Distribution Agreement

In presenting this dissertation as a partial fulfillment of the requirements for an advanced degree from Emory University, I hereby grant to Emory University and its agents the non-exclusive license to archive, make accessible, and display my dissertation in whole or in part in all forms of media, now or hereafter known, including display on the world wide web. I understand that I may select some access restrictions as part of the online submission of this dissertation. I retain all ownership rights to the copyright of the dissertation. I also retain the right to use in future works (such as articles or books) all or part of this dissertation.

_____ _____

Lakshmi Pullasseri Madom Narayana Iyer Date

Exploring Novel Quantum Phases in both Periodic and Fractal Topological Systems

By

Lakshmi Pullasseri Madom Narayana Iyer
PhD

Department of Physics

Prof. Luiz H Santos
Advisor

Prof. Wladimir Benalcazar
Committee Member

Prof. Stefan Boettcher
Committee Member

Prof. Raphael Ribeiro
Committee Member

Prof. Ajit Srivastava
Committee Member

Accepted:

Kimberly Jacob Arriola
Dean of the James T. Laney School of Graduate Studies

February 27, 2025

Date

Exploring Novel Quantum Phases in both Periodic and Fractal Topological Systems

By

Lakshmi Pullasseri Madom Narayana Iyer

Advisor: Prof. Luiz H Santos

An abstract of
A dissertation submitted to the Faculty of the
Emory College of Arts and Sciences of Emory University
in partial fulfillment of the requirements for the degree of
PhD
in Department of Physics
2024

Abstract

Exploring Novel Quantum Phases in both Periodic and Fractal Topological Systems
By Lakshmi Pullasseri Madom Narayana Iyer

The collective electronic behavior in materials, fundamental to condensed matter physics, often arises from the periodic potential landscape created by an ordered atomic lattice, which allows the application of Bloch's theorem and traditional band theory. These frameworks reveal characteristic energy bands and gaps in periodic systems, with features such as Van Hove singularities (VHS) enhancing interaction-driven quantum phases like superconductivity, magnetism, and charge density waves. Interestingly, higher-order VHS (HOVHS), arising from higher-order saddle points in band dispersion, exhibit an even stronger density of states divergence, amplifying correlation effects and providing fertile ground for novel electronic phases. In this thesis, we focus on the interplay of HOVHS and broken time-reversal symmetry (TRS) in topological systems.

We investigate this phenomenon in the context of two distinct systems. First, we examine the interplay between HOVHS and broken TRS on the surface of 3D topological insulators (TIs). Specifically, we explore the emergence of topological Chern bands on the surface of TIs, which host higher-order Van Hove singularities characterized by a power-law divergence in the density of states. These singularities arise from the interaction between a time-reversal symmetry-breaking Zeeman field, induced by proximity to a ferromagnetic insulator, and a time-reversal invariant moiré potential influencing the surface electrons. The singularities are modulated by the relative energy scales of the Zeeman field and moiré potential, providing a novel platform for realizing exotic Lifshitz transitions in topological bands.

We next turn our attention to the kagome lattice, a geometrically frustrated system with the potential for hosting exotic quantum phases. By introducing time-reversal-breaking next-nearest-neighbor (NNN) hopping, we induce non-trivial topological band structures characterized by higher Chern numbers. This intricate interplay between geometry and topology gives rise to a rich landscape of HOVHS in the electronic band structure, controlled by the phase and magnitude of the NNN hopping. This classification of HOVHS in kagome systems provides a platform to explore unconventional electronic orders induced by electronic correlations. Furthermore, the NNN hopping induces topological bands with higher Chern numbers obeying a sublattice interference, where electronic states in specific bands became maximally localized on particular sublattices at high-symmetry points in the Brillouin zone.

The second focus of this thesis extends beyond conventional band theory by exploring electronic systems with fractal symmetry, thereby challenging traditional frameworks that rely on translational invariance. By employing fractal geometries, we construct potential landscapes that lack periodicity, aiming to understand how self-similarity influences the behavior of Dirac fermions on the surfaces of 3D topological insulators (TIs). We investigate a novel class of states that arise from the

coupling of surface Dirac fermions to a time-reversal symmetric fractal potential, which breaks translational symmetry while preserving self-similarity. Using large-scale exact diagonalization, scaling analysis of the inverse participation ratio, and the box-counting method, we identify the emergence of self-similar Dirac fermions with fractal dimension for a surface potential modeled after the Sierpinski carpet fractal. These states, characterized by their fractal dimension, open promising avenues for exploring exotic transport phenomena and the potential for quantum information storage in topological systems with fractal dimensionality.

In summary, this thesis systematically studies novel quantum phases in both periodic and non-periodic topological systems. By investigating systems both within and beyond the constraints of translational invariance, this research highlights how unique electronic behaviors can emerge when established paradigms of band theory are pushed into new regimes.

Exploring Novel Quantum Phases in both Periodic and Fractal Topological Systems

By

Lakshmi Pullasseri Madom Narayana Iyer

Advisor: Prof. Luiz H Santos

A dissertation submitted to the Faculty of the
Emory College of Arts and Sciences of Emory University
in partial fulfillment of the requirements for the degree of
PhD
in Department of Physics
2024

Acknowledgments

First and foremost, my deepest gratitude to my advisor Prof. Luiz H Santos for providing a direction to my research, for being available almost anytime to have a discussion whenever I reach a dead-end, for providing me with much-needed encouragement and support, especially before my talks, for his patience with me through my PhD journey and also for his wonderful movie and restaurant suggestions. His expertise and encouragement were instrumental in shaping this research. It has been indeed a great privilege to be a student of such an exceptional teacher and researcher.

I would also like to thank my thesis committee, Luiz H Santos, Wladimir Benalcazar, Stefan Boettcher, Raphael Ribeiro, and Ajit Srivastava, for their invaluable guidance, support, and encouragement throughout my research journey. I am particularly grateful to Wladimir and Stefan for their support and understanding during challenging times, and to Ajit and Rafael for their insightful feedback and constructive criticism, which significantly contributed to the quality of this work. My sincere thanks go to all my committee members for their dedication and commitment to my academic and professional development.

I would like to thank my fellow physicists, Dr. Jian Wang, Dr. Daniel Shaffer, Tianhong Lu, and Edrick Wang, for the many wonderful discussions I shared with them. They have taught me, challenged me, and inspired me to become a better physicist.

I owe my thanks to the people at Emory for providing me with a warm welcome to this country and for making this journey a memorable experience for me. I would especially like to thank Barbara Conner for her assistance with paperwork, scheduling, and all PhD-related matters beyond research. I also express my heartfelt gratitude to Prof. Justin Burton and Prof. Hayk Harutyunyan for their invaluable support in helping me navigate both personal and professional challenges.

This acknowledgment would be incomplete without mentioning the friends I have accumulated throughout my life, without whose unwavering support and encouragement, my research journey might have stopped years ago. I extend my heartfelt gratitude to my chosen family, especially, Gokul Premraj, Katie Whitcomb, Mahajabin Rahman, Tomilola Obadiya, and Robins Kurian, for nudging me in the right direction whenever I needed it the most.

Last but not least, I owe my thanks to my family to whom I dedicate this thesis. Their unconditional support and faith in me have helped me beyond words. I wholeheartedly thank them for inspiring me with their words and life, to strive to be my best self in my professional and personal life.

Contents

List of Figures

List of Tables

Chapter 1

Introduction

The fundamental basis of condensed matter physics lies in understanding how the collective behavior of a vast number of atoms and electrons in a material gives rise to its macroscopic properties, such as electrical conductivity, magnetism, and superconductivity. To understand these emergent properties, it is essential to study how the electrons move through and interact with the potential energy landscape created by the host material's atomic structure, which significantly influences these properties.

When the atoms of the host material are arranged in a periodic lattice, the potential energy landscape experienced by the electrons as they traverse the crystal mirrors the periodicity of the lattice. This periodicity implies that the system possesses translational invariance, meaning that the lattice remains invariant under translations by lattice vectors. Such a translational invariant potential allows for the application of Bloch's theorem [3, 4], which posits that the wave function of an electron in a periodic potential can be expressed as a plane wave modulated by a periodic function that reflects the periodicity of the lattice. Consequently, the electron's wave function can be expressed in terms of wave vectors that are intrinsically linked to the periodicity of the crystal lattice, enabling the electron's

behavior to be effectively described in momentum space.

The translational invariance of the crystal imposes specific limits on the energies that electrons can have, leading to the creation of distinct energy bands in momentum space. As electrons move through the crystal, the periodic potential they encounter causes constructive and destructive interference at certain wave vectors. This interference creates regions where electrons are allowed to exist and regions where they are not, known as permitted and forbidden energies, respectively. As a result, energy bands are formed, separated by gaps where no electrons can reside (band gaps) [3, 4].

These energy bands can be visualized as compact manifolds in momentum space, with electron energy varying continuously with respect to the wave vector. While energy bands are bounded in all dimensions, something particularly intriguing occurs in two-dimensional (2D) systems. In 2D, the momentum space manifold takes the form of a torus and the Poincaré-Hopf theorem [5] implies that the presence of both maxima and minima within an energy band necessitates the existence of saddle points. At these saddle points, the gradient of the energy dispersion vanishes, as shown in Fig. 1.1(a), causing the energy surface to locally flatten. In the 1950s, physicist Léon Van Hove showed that around these points—now known as Van Hove singularities (VHS)—the density of states diverges logarithmically [6], as shown in Fig. 1.1(b). This sharp increase in the density of states near the VHS signifies a critical point in the band structure, with profound implications for the material's electronic properties.

The large accumulation of electronic states near these VHS creates an ideal environment for studying interaction-driven effects. With so many states available at similar energy levels, electrons near a Van Hove singularity experience amplified interactions, often giving rise to novel quantum phases, such as unconventional superconductivity, magnetism, or charge density waves [7–27]. These dense regions

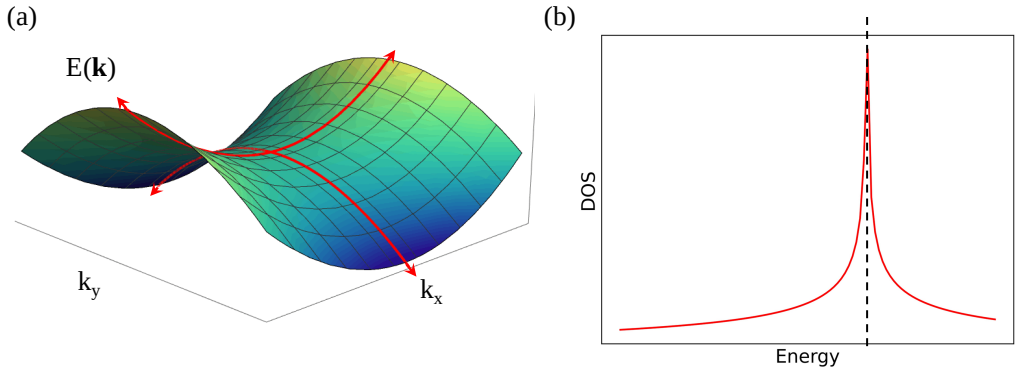

Figure 1.1: (a) Energy dispersion of the form $E(\mathbf{k}) = k_x^2 - k_y^2$, depicting a saddle point at $E = 0$ where the red lines cross. The red lines denote the gradient at the saddle point along the k_x and k_y directions. (b) The corresponding density of states exhibiting logarithmic divergence as $E \to E_{vhs} = 0$ (denoted by the dashed black line).

of states provide a fertile ground for exploring exotic phenomena in 2D systems, making them especially valuable in the quest to discover new material properties and potential applications in quantum technologies.

An intriguing scenario arises when the energy dispersion of electronic bands supports higher-order saddles, giving rise to higher-order Van Hove singularities (HOVHS), which are characterized by a stronger power-law divergence in the density of states [28, 29]. Unlike conventional VHS [6], which exhibits a logarithmic divergence, HOVHS enhances this effect further, resulting in an even denser concentration of electronic states at specific energy levels. This extreme accumulation of states near HOVHS creates an amplified setting for interaction effects, making them highly promising for exploring unconventional electronic phases [28–40].

Although HOVHS have been studied in time-reversal symmetric systems, their behavior in time-reversal broken systems remains largely unexplored. The breaking

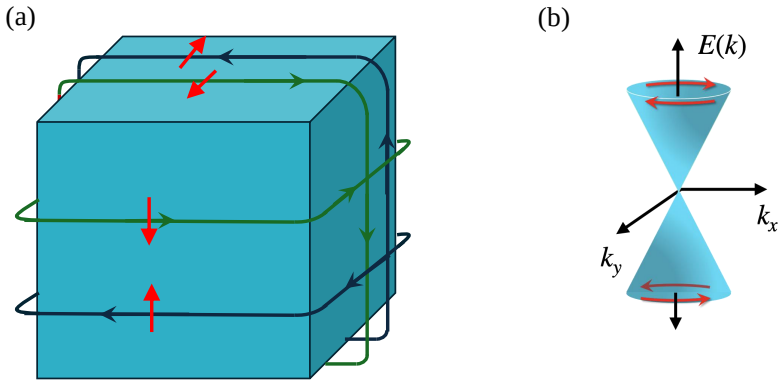

Figure 1.2: (a) Schematic representation of the 3D TI in real space. Electrons with spins up and down (denoted by the red arrows) move in opposite directions. (b) The corresponding energy dispersion plot, showing Dirac cones at the surface states.

of time-reversal symmetry (TRS) in topological systems can give rise to phenomena such as topological superconductivity [41–45] and fractional quantum Hall effects [46, 47], which are often driven by strong correlations that are naturally intensified near HOVHS. Moreover, the interplay between HOVHS and broken TRS could lead to the emergence of novel quantum states, such as superconducting pair-density waves and Chern supermetals [48] in the time-reversal broken Haldane model that supports HOVHS. Breaking TRS also provides a unique opportunity to explore the interaction between HOVHS and band topology, an area that remains relatively underexplored. This combination of factors makes time-reversal symmetry-broken systems particularly exciting for the discovery of new quantum phases.

Driven by the potential to uncover novel quantum states that may emerge from this unique combination, we focus on the interplay between HOVHS and broken TRS in two distinct systems: the surface of a 3D topological insulator (TI) and a kagome lattice system.

3D TIs [49–51] (Fig. 1.2(a)) are characterized by insulating bulk behavior and conducting surface states that arise due to the strong spin-orbit coupling intrinsic to these materials. These surface states are protected by the bulk-boundary correspondence, a hallmark of topological states, and exhibit a Dirac-like dispersion, as shown in Fig. 1.2(b). A crucial feature of these surface states is their spin-momentum locking, where the spin of an electron is orthogonal to its momentum, which gives rise to robust transport properties and suppresses backscattering in the presence of non-magnetic impurities.

The exposed boundary of a 3D TI provides a unique platform for manipulating these topologically protected surface states and engineering exotic quantum phenomena. External perturbations such as magnetic fields, magnetic doping, or proximity-induced effects can break time-reversal symmetry (TRS), opening a gap at the Dirac point and altering the electronic dispersion. This broken symmetry enables phenomena like the quantum anomalous Hall effect [52, 53], where dissipationless edge currents arise even in the absence of an external magnetic field. Furthermore, coupling the surface states to a superconducting substrate can induce topological superconductivity [54, 55] and pave the way for realizing exotic quasiparticles like Majorana fermions [56–58], which hold promise for fault-tolerant quantum computing.

The manipulability of these surface states is complemented by the accessibility provided by techniques such as angle-resolved photoemission spectroscopy (ARPES) and scanning tunneling microscopy (STM), which allow precise mapping and control of their electronic structure. This makes the surface of a 3D TI an ideal platform to explore how HOVHS interacts with broken TRS to generate unique quantum states.

Similarly, the kagome lattice [59, 60] shown in Fig. 1.3(a), known for its geometric frustration and the potential to host flat bands [61–65], Dirac fermions [66, 67] as

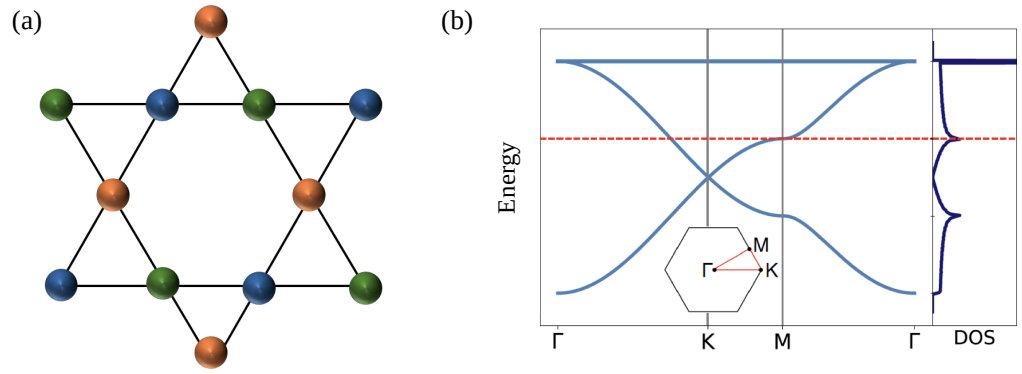

Figure 1.3: (a) Schematic representation of the kagome lattice. (b) Band structure of the nearest-neighbor kagome model demonstrating the flat band (the highest band) and Dirac cone at the ***K*** point. The corresponding DOS is displayed on the right. The red dashed lines denote the energy at which the ***M*** points of the second band support a conventional VHS.

well as VHSs [39, 67], as shown in Fig. 1.3(b), provides a natural setting for the emergence of HOVHS. When coupled with time-reversal symmetry breaking—such as through magnetic ordering or applied magnetic fields—the kagome lattice system offers a rich ground for studying the enhanced effects of HOVHS in the presence of nontrivial band topology. This interplay opens up a wealth of possibilities for novel quantum phases, as seen in kagome metals [59, 68] where the potential for exotic states, such as quantum spin liquids or chiral superconductivity [68–77], grows as HOVHS come into play. Both systems— the surface of a 3D TI and the kagome lattice—offer distinct but complementary environments for studying the interplay between HOVHS and broken TRS, each providing unique opportunities to uncover new quantum states and phenomena.

While Bloch's theorem provides a robust framework for understanding the electronic properties of crystalline solids with perfect periodicity, real-world materials

often exhibit deviations from this ideal. Disordered crystals, for instance, can introduce subtle imperfections that, while not completely disrupting long-range order, can give rise to quantum interference effects such as weak localization. Amorphous materials, lacking any long-range order, pose even greater challenges to traditional band theory. To fully comprehend the behavior of these complex systems, a systematic approach to studying materials with a complete absence of translational symmetry is essential. Exploring such systems not only addresses the practical need to understand the behavior of real-world materials and devices but also fuels intellectual curiosity to uncover novel quantum phenomena beyond the confines of periodic lattices.

To systematically study these translation symmetry-broken systems, we employ fractal geometry as a framework to construct and analyze potential energy landscapes with complex spatial structures. Fractals [78, 79] provide a unique setting where self-similarity replaces periodicity, enabling us to explore electronic behaviors in a fundamentally non-periodic, yet highly ordered setting. A recent study demonstrated that the assembly of Sierpiński gasket fractal networks on copper surfaces—achieved through the deposition of CO molecules—results in surface states with fractal dimensions [80]. Motivated by this, this thesis focuses on investigating the effects of fractal geometry on the surface of 3D TIs, aiming to understand how potential landscapes with fractal symmetries influence electronic states.

Unlike the surface of copper, 3D TIs possess a unique electronic structure characterized by topologically protected Dirac fermions. These massless fermions exhibit remarkable properties such as Klein tunneling, allowing them to traverse potential barriers regardless of their height, and a quantized Berry curvature of π, leading to anomalous Hall effects and other exotic transport phenomena. The interplay between the unique electronic properties of 3D TIs and the intriguing nature of

fractal geometry makes this a particularly exciting avenue for exploration.

In a nutshell, this thesis explores two distinct avenues of research. The first focuses on the behavior of electrons within a translational invariant potential energy landscape, specifically investigating the interplay between HOVHS and broken TRS. This investigation is conducted in the context of two specific systems: the surface of a 3D topological insulator (TI) and a kagome lattice system. The second avenue delves into the realm of non-periodic systems, examining the electronic properties of potential energy landscapes that exhibit fractal geometry. This exploration involves coupling the surface Dirac fermions of 3D TIs with fractal geometries.

Structure of the Thesis

In Chapter 2, we investigate the interplay of HOVHS and broken TRS on the surface of 3D TIs. We examine how the interplay of a time-reversal breaking Zeeman field and a time-reversal invariant moiré potential leads to the formation of topologically non-trivial bands on the surface, which host HOVHS. Our analysis further identifies a characteristic signature in the low-temperature intrinsic anomalous Hall conductivity near the VHS, providing a potential pathway to probe Van Hove singularities in Chern bands through anomalous transport measurements.

In Chapter 3, we turn our attention to a spinless fermion kagome system with both nearest-neighbor (NN) and next-nearest-neighbor (NNN) hopping. The introduction of the complex NNN hopping that breaks TRS yields topological bands with non-zero Chern number. We explore the resulting electronic structure, with a particular focus on how HOVHS emerges in this system, and we uncover a rich and complex landscape of HOVHS, controlled by the magnitude and phase of the NNN hopping. Additionally, the NNN hopping induces the formation of higher Chern number bands in the middle of the spectrum obeying a sublattice interference.

Chapter 4 introduces a novel system in which surface Dirac fermions on 3D TIs are coupled to a fractal potential. This potential breaks translation symmetry while

maintaining self-similarity, and the study focuses on understanding the influence of fractal geometries on the electronic properties of the surface states. The work aims to uncover how fractal geometries can lead to unique transport phenomena and quantum states on the surface of 3D TIs.

Finally, in Chapter 5, we present a summary of the key findings of this dissertation. We emphasize the intricate relationship between HOVHS and band topology in 3D TIs as well as kagome systems. Additionally, we explore the coupling of surface Dirac fermions in 3D TIs with fractal geometry, where we have systematically investigated a non-periodic system that extends beyond the scope of Bloch's theorem. This chapter also outlines potential future directions for research.

Chapter 2

Chern Bands with Higher-Order Van Hove Singularities on Topological Moiré Surface States

Note: The material presented in this chapter has been published in *Physical Review B*, 110(11):115125, 2024. DOI: 10.1103/PhysRevB.110.115125

In this chapter, we investigate the emergence of topological Chern bands on the surface of three-dimensional topological insulators, which host higher-order Van Hove singularities that are characterized by the power-law diverging density of states. Such singularities emerge from the interaction between a time-reversal symmetry-breaking Zeeman field, induced by proximity to a ferromagnetic insulator, and a time-reversal invariant moiré potential affecting the surface electrons. These singularities are modulated by the Zeeman and moiré potential energy scales, presenting a novel platform for realizing exotic Lifshitz transitions in topological bands.

In two-dimensional systems, topological changes of the Fermi surface, known as Lifshitz transitions [81], are marked by saddle points in the energy dispersion,

which give rise to Van Hove singularities (VHS) where the density of states has a logarithmic divergence. [6] Van Hove has demonstrated that these singularities are generic features of two-dimensional periodic systems, and the existence of saddle points in the periodic energy dispersion $\varepsilon(\boldsymbol{k})$ is of topological origin and can be understood within the framework of Morse theory. Recent progress in the synthesis of new classes of two-dimensional materials along with the possibility of engineering electronic band structures have renewed interest in characterizing electronic states near VHS. In particular, the enhancement of interaction effects due to the large accumulation of electronic states in the vicinity of VHSs has been studied as a fruitful setting to characterize Fermi liquid instabilities in cuprates [19, 82, 83], doped graphene [20, 84–86], Hofstadter systems [21, 22] and moiré graphene superlattices [10–18, 87].

A physically rich scenario occurs when the energy dispersion of electronic bands supports higher-order saddles, giving rise to higher-order Van Hove singularities (HOVHS) characterized by stronger power-law divergence of the density of states.[28, 29] While previous studies of HOVHS have mainly focused on the properties of time-reversal invariant bands, the interplay between HOVHS and time-reversal broken Chern bands has been recently highlighted as a path towards new electronic phases. [48, 88] In particular, Ref. [48] has mapped the landscape of VHS of Haldane Chern bands on the honeycomb lattice [89] and demonstrated that, under inversion symmetry, the system supports a pair of HOVHS at the two valleys of the Brillouin zone which, under repulsive interactions, give rise to a rich phase diagram containing pair density wave superconductivity and a Chern super metal state. These developments highlight the importance of identifying new electronic platforms supporting Chern bands with HOVHS.

In this work, we present an approach to design Chern bands that support HOVHS. Our mechanism combines the breaking of time-reversal symmetry and the

presence of a moiré pattern in a system that hosts a single Dirac cone. Specifically, we provide a route to realize Chern bands supporting HOVHS on the surface of three-dimensional topological insulators (TI). [49–51]

Recent experiments have revealed that a moré pattern can emerge on the surface of topological insulators that host a single Dirac fermion when the crystals are grown using the technique of molecular beam epitaxy (MBE). In the case of Bi_2Te_3[2] a small in-plane rotation of the top layer (facilitated by Cu dopants that reduce the interlayer coupling) results in the emergence of a triangular moiré superlattice of constant $\approx 13nm$. [1] Moreover, on Bi_2Se_3 [90] grown using MBE on a substrate, superstructures with lattice constants $\approx 10nm$ can be constructed from the direct lattice mismatch of the crystal with substrates like graphene, [91] FeSe,[92] $\mathrm{Au}(111)$,[93] hBN[94] and In_2Se_3. [95] The interplay of Dirac surface states with a time reversal invariant moiré surface potential reorganizes the surface states into a sequence of moiré bands hosting satellite Dirac fermions.[30, 96]. Furthermore, near charge neutrality, one of these time-reversal invariant bands can support a pair of HOVHS with cubic dispersion on each of the valley points $\pm\boldsymbol{K}$ of the moiré Brillouin zone.[30].

We explore the effects of a Zeeman field on these HOVHS states near charge neutrality. The addition of a Zeeman field significantly modifies the characters of the HOVHS band near charge neutrality. First, the Zeeman field gaps out this band resulting in a pair of topological bands with Chern numbers ± 1 near charge neutrality. Second, the Zeeman field behaves as a control knob for the character of the Lifshtz transition. Specifically, while the time-reversal symmetric pair of HOVHS occurs for a fine-tuned value of the moiré potential V,[30] the Zeeman field gives rise to a line HOVHS in the (V, h) plane. Remarkably, we uncover simple expressions for these lines of HOVHS in a Chern band for moiré potentials with C_3 and C_6 rotation symmetries, and we estimate that this HOVHS manifold could be within experimental reach for certain TI systems. These results establish a

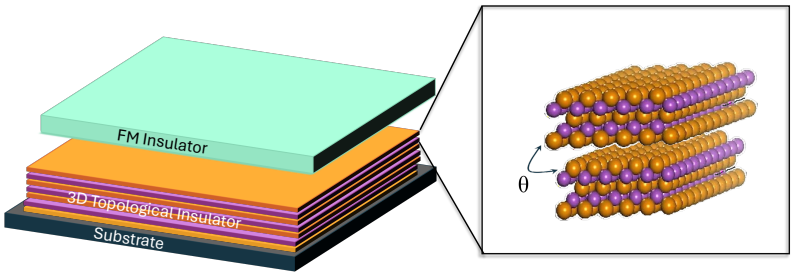

Figure 2.1: Schematic illustration of the experimental realization of 3D TI surface with a relative twist between the top quintuple layers, as shown in the inset, in proximity with a ferromagnetic insulator that breaks TRS.

promising route to achieve higher-order Lifshitz transitions in time-reversal broken TI surface states.

The existence of exotic Lifshtz transitions in topological Chern bands raises the prospect of exploring new interplays between Van Hove singularities and band topology. Along these lines, we establish a connection between Lifshitz transitions and the quantum geometry of Chern bands through the intrinsic part of the anomalous Hall conductivity σ_{xy}^{int}. [97–99] The intrinsic Hall anomalous Hall contribution arises from non-zero Berry curvature of the Bloch states, which leads to an anomalous Hall velocity[100–102] when charges are coupled to an electric field. In the low-temperature limit, we show that $d\sigma_{xy}^{\text{int}}/d\mu$ is proportional to the average Berry curvature on the Fermi surface and the density of states at the Fermi energy. In particular, this relationship implies a diverging behavior in $d\sigma_{xy}^{\text{int}}/d\mu$ as the chemical potential μ is tuned across the Lifshitz transition, a salient feature that could be observed in low-temperature transport experiments when the anomalous Hall response is dominated by Berry phase effects.

2.1 Higher Order Van Hove Singularities

In this section, we describe a mechanism to obtain Chern bands supporting HOVHS, which relies on a system described by a single Dirac fermion coupled to a periodic potential and a time-reversal breaking uniform Zeeman field. Notably, these three ingredients can be realized on the surface of 3D TI such as Bi_2Se_3 or Bi_2Te_3, subject to a moiré pattern in proximity to a ferromagnetic insulator. As such, we henceforth focus on this system described by the Hamiltonian

$$\hat{H} = \int d^2\boldsymbol{r}\, \hat{\psi}^\dagger(\boldsymbol{r}) H\, \hat{\psi}(\boldsymbol{r}) \tag{2.1a}$$

where $\hat{\psi}^T(\boldsymbol{r}) = (\psi_\uparrow(\boldsymbol{r}), \psi_\downarrow(\boldsymbol{r}))$ is the two-component spinor with $\psi_{\sigma=\uparrow,\downarrow}(\boldsymbol{r})$ the electron annihilation operator, and

$$H = v_F\, \hat{z} \cdot (-i\, \boldsymbol{\nabla} \times \boldsymbol{\sigma}) + V(\boldsymbol{r})\sigma_0 + h_z\sigma_z\,, \tag{2.1b}$$

where v_F is the Fermi velocity, $\boldsymbol{\sigma} = (\sigma_x, \sigma_y, \sigma_z)$ are the Pauli matrices, σ_0 is the identity matrix, and $\hbar = 1$. $V(\boldsymbol{r}) = V(\boldsymbol{r} + \boldsymbol{R})$ (where $\boldsymbol{R}$ is a translation vector) is a time-reversal invariant periodic superlattice potential, and h_z is a time-reversal breaking uniform Zeeman field. The low energy theory depends upon three energy scales: the effective bandwidth v_F/a where a is the superlattice constant, the strength of the moiré potential V, and the Zeeman energy scale h_z. Henceforth, we work in rescaled units where the low-energy physics is determined by the dimensionless parameters $V\,a/v_F$ and $h_z\,a/v_F$.

In TIs such as Bi_2Te_3 and Bi_2Se_3, the moiré pattern can emerge when the crystals are grown using MBE. For Bi_2Te_3 with a Fermi velocity of approximately 0.3 eV nm, [2] a small in-plane rotation of the top layer, which is facilitated by Cu dopants that reduce the interlayer coupling, results in the emergence of moiré triangular

superlattice with lattice constant $a \approx 13$ nm. [1] In Bi_2Se_3 with a Fermi velocity of 0.4 eV nm [90] grown using MBE on a substrate, superlattices with periodicity a ranging from 2 to 7 nm can be constructed from the direct lattice mismatch of the crystal with the substrates like graphene, [91] FeSe,[92] Au(111),[93] hBN[94] and In_2Se_3. [95]

Since the single particle Hamiltonian Eq. (2.1b) is invariant under translations by a lattice vector $\boldsymbol{R}$ of the moiré superlattice, the eigenvalue equation for the Bloch states reads

$$H\Psi_{n,\boldsymbol{k}} = E_{n,\boldsymbol{k}}\Psi_{n,\boldsymbol{k}}\,, \tag{2.2}$$

where the two-component spinor $\Psi_{n,\boldsymbol{k}}(\boldsymbol{r}) = e^{i\boldsymbol{k}\cdot\boldsymbol{r}}U_{n,\boldsymbol{k}}(\boldsymbol{r})$ with $U_{n,\boldsymbol{k}}(\boldsymbol{r}+\boldsymbol{R}) = U_{n,\boldsymbol{k}}(\boldsymbol{r})$. From Eq.(2.2) it follows that

$$H_{\boldsymbol{k}}U_{n,\boldsymbol{k}}(\boldsymbol{r}) = E_{n,\boldsymbol{k}}U_{n,\boldsymbol{k}}(\boldsymbol{r})\,, \tag{2.3a}$$

where

$$H_{\boldsymbol{k}} = v_F\left[\hat{z}\cdot(-i\boldsymbol{\nabla}+\boldsymbol{k})\times\boldsymbol{\sigma}\right] + V(\boldsymbol{r})\sigma_0 + h_z\sigma_z\,. \tag{2.3b}$$

We numerically diagonalize Eq.(2.3) for a total number of 242 bands. One of our main findings is that the reconstructed Dirac spectrum obtained from Eq.(2.3) contains a Chern band near charge neutrality supporting cubic HOVHS with power law diverging density of states $\rho(\varepsilon) \sim |\varepsilon|^{-1/3}$, where the energy scale of the HOVHS is set to zero.

The appearance of HOVHS in this topological band is controlled by h_z and V. The energy scale h_z corresponds to the Zeeman gap opened in the Dirac spectrum, which can be experimentally realized in heterostructures where the 3D TI surface is coupled by the proximity effect to a ferromagnetic insulator (FMI). Experimental realizations of the TI-FMI heterostructure of the quintuple layered 3D TIs such as Bi_2Se_3 and Bi_2Te_3, and FMIs with comparable lattice constants, such as EuS,[103,

104] MnSe,[105, 106] MnTe,[107] and $Y_3Fe_5O_{12}$[108] present evidence for broken TRS on the TI surface. Leveraging on these experimental conditions, we propose a path to realizing moiré Chern bands on the TI surface by coupling 3D TIs where there is an in-plane rotation of the top quintuple layers, with an FMI of comparable lattice constant, as shown in Fig. 2.1.

The point group symmetries of the moiré potential play an important role in the structure of the higher-order Lifshitz transitions. To address the role of point group symmetries, we consider two classes of superlattice potentials with C_6 and C_3 symmetry. In the C_6 symmetric case, the HOVHS appears as a pair at the valley $\pm\boldsymbol{K}$, as shown in Section 2.1.1. Breaking the C_6 symmetry down to C_3 results in a single HOVHS located either at $\boldsymbol{K}$ or at $-\boldsymbol{K}$ valley, as discussed in Section 2.1.2. In what follows, we study each of these cases separately.

2.1.1 C_6 symmetric moiré potential

We consider Dirac electrons under the effect of the C_6 periodic moiré potential as shown in Fig. 2.2a

$$V_6(\boldsymbol{r}) = 2V \sum_{j=1}^{3} \cos\left(\boldsymbol{G}_j \cdot \boldsymbol{r}\right), \tag{2.4}$$

where $\boldsymbol{G}_j = \frac{4\pi}{\sqrt{3}a}\left[-\sin\left(\frac{2\pi j}{3}\right), \cos\left(\frac{2\pi j}{3}\right)\right]$ are the reciprocal lattice vectors, and V is the strength of the lattice potential. This potential has invariance under three-fold rotations and inversion symmetry since $V(\boldsymbol{r}) = V(-\boldsymbol{r})$. Without a Zeeman field, the potential given in Eq.(2.4) yields a gapless spectrum that supports a band with a pair of HOVHS at the valleys $\pm\boldsymbol{K}$ of the moiré Brillouin zone when the strength of the potential $V_0 = 1.36 v_F/a$ [30]. Despite this higher-order Lifshtiz transition, these bands remain topologically trivial due to time-reversal symmetry. At $V = V_0$, the higher-order saddle point at each valley carries a topological index of -2 corresponding to the winding of the vector field $\boldsymbol{\nabla}_{\boldsymbol{k}}\varepsilon(\boldsymbol{k})$ around the higher-order

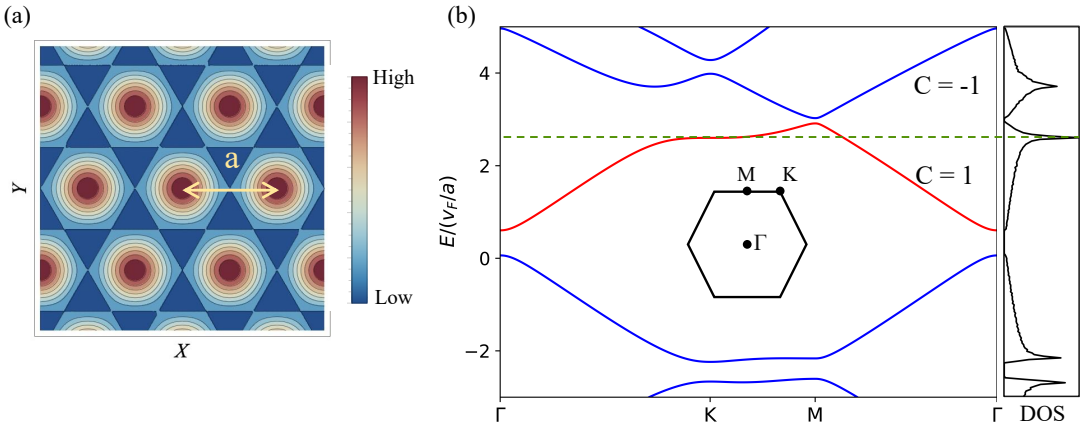

Figure 2.2: (a) Contour plot of the C_6 symmetric potential $V_6(\boldsymbol{r})$, given in Eq. (2.4), with superlattice constant a. (b) Band structure of the model given in Eq. (2.1b) with the C_6 periodic potential for $(h_z, V) = (0.5, 1.38)$ in units of (v_F/a) to the left. The mini Brillouin zone is shown in the center. The isolated band shown in red carries the Chern number $C = 1$, and it supports HOVHS at the $\pm\boldsymbol{K}$ points, as indicated by the peak in the DOS shown on the right. The green dashed line denotes the energy at the $\pm\boldsymbol{K}$ points, where the DOS diverges.

saddle point.[109, 110]

To achieve a topological band supporting HOVHS, time-reversal symmetry is broken with the Zeeman field induced by the proximity effect. On turning the Zeeman field on for $V = V_0$, the higher-order saddle point splits into 4 critical points, of which 3 are ordinary saddle points with a topological index of -1 each and the remaining one is a local extremum with a topological index of 1, such that the sum of the topological indices $3 \times (-1) + 1 = -2$ remains conserved. At the same time, the lowest pair of conduction bands acquire an energy gap and Chern numbers of ± 1 [111], as shown in Fig.2.2(b).

Remarkably, we notice that these split critical points (i.e., three conventional VHS and one extremum) can be merged together again at $\pm\boldsymbol{K}$ to generate a HOVHS in the Chern band marked in red in Fig.2.2(b) by adjusting either V or h_z. We uncover a line in (h_z, V) parameter space, shown in Fig. 2.3(a), where the $C = 1$

band supports pairs of HOVHS. This line in (h_z, V) parameter space obeys the relation

$$V_6(h_z) = V_6^{(0)} + \Gamma\, h_z^2\,, \tag{2.5}$$

where, $V_6^{(0)} = V_6(h_z = 0) = 1.36 v_F/a$, and $\Gamma \approx 0.05$ is a fitting parameter. The quadratic scaling between h_z and V is observed for h_z values ranging from 0 to $\approx 2v_F/a$. As a result, for moiré surface states with lattice constant $a \approx 10$ nm and Fermi velocity $v_F \approx 300$ meV. nm, the parameters h_z and V that can be employed to tune the HOVHS follow the scaling relation given in Eq. (2.5) for h_z as large as 60 meV

To understand the relation given by Eq. (2.5), we study the energy dispersion around the valley $\boldsymbol{K}$,

$$\varepsilon(\boldsymbol{p}) \equiv E(\boldsymbol{p} + \boldsymbol{K}) - E(\boldsymbol{K}) = \alpha p^2 + \beta(p_x^3 - 3p_x p_y^2)\,, \tag{2.6}$$

where $\boldsymbol{p} = (p_x, p_y)$ is the momentum in the vicinity of the valley. The momentum dependence of the dispersion Eq. (2.6), expanded up to the third order, is dictated by the point group symmetries of the hexagonal lattice. From this, we obtain the critical points $\boldsymbol{\nabla}_{\boldsymbol{p}}\varepsilon(\boldsymbol{p}) = 0$ and characterize their behavior by computing the Hessian $\mathcal{H} = \det\Big(\partial_{p_i}\partial_{p_j}\varepsilon(\boldsymbol{p})\Big)$.

While the gradient of the dispersion vanishes for $\boldsymbol{p} \in \Big\{(0,0), \big(\frac{-2\alpha}{3\beta}, 0\big), \big(\frac{\alpha}{3\beta}, \pm\frac{\alpha}{\sqrt{3}\beta}\big)\Big\}$, the corresponding Hessian $\mathcal{H} = 4(\alpha^2 - 9\beta^2 p^2)$ evaluated at each of the four aforementioned critical points vanishes only when the coefficient $\alpha = 0$, which implies the vanishing of the term quadratic in momentum. Thus, the scaling relation Eq. (2.5) characterizes the points in the (h_z, V) parameter space for which the quadratic in momentum coefficient $\alpha(h_z, V) = 0$, so that the energy dispersion around $\boldsymbol{K}$ can be described by a third-order polynomial $\varepsilon(\boldsymbol{p}) \approx \beta(p_x^3 - 3p_x p_y^2)$, corresponding to a HOVHS with diverging density of states $\rho(\varepsilon) \sim \frac{1}{|\varepsilon|^{1/3}}$. [28]

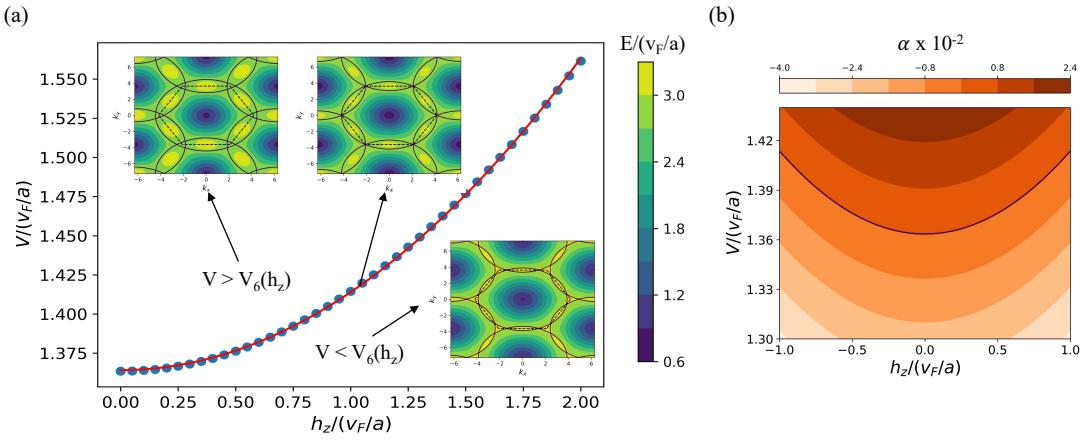

Figure 2.3: (a) Parameter space plot showing the values of the Zeeman mass (h_z) and the lattice potential strength (V) that corresponds to HOVHS located at the $\pm\boldsymbol{K}$ points of the BZ. The (h_z, V) pairs follow a scaling relation given by Eq.(2.5). The contour plots of the Fermi surfaces corresponding to the regions- $V > V_6(h_z)$, $V = V_6(h_z)$, and $V < V_6(h_z)$ are shown in the inset, where the dotted black lines indicate the boundaries of the FBZ and the black lines show the Fermi surfaces passing through VHS. (b) $\alpha(h_z, V)$ obtained using Eq. (2.7) plotted in the $h_z - V_6$ parameter space. The thick black curve indicates the $\alpha(h_z, V) = 0$ line which, as expected, coincides with the $h_z - V$ curve shown in (a) that corresponds to the emergence of HOVHS at $\pm\boldsymbol{K}$ points.

Furthermore, in the range of (h_z, V) values where we observe the quadratic scaling given in Eq. (2.5), the parameter $\alpha(h_z, V)$ can be well approximated by the empirical form,

$$\alpha(h_z, V) = \alpha_0 \ln\left[\frac{V}{V_6(h_z)}\right], \tag{2.7}$$

where $\alpha_0 \approx 0.4$, and $V_6(h_z)$ is given by Eq. (2.5). The manifold of (h_z, V) values for which $\alpha(h_z, V)$ vanishes is denoted by the black curve in Fig. 2.3(b). When the strengths of the potential and the Zeeman energy deviate from condition (2.5), the HOVHS splits into three ordinary saddle point VHS for $\boldsymbol{p} \in \left\{\left(\frac{-2\alpha}{3\beta}, 0\right), \left(\frac{\alpha}{3\beta}, \pm\frac{\alpha}{\sqrt{3}\beta}\right)\right\}$ and a local extremum at $\boldsymbol{p} = (0, 0)$. Under small deviations δV of the moiré potential and the Zeeman energy from $(h_z = 0, V = V_6)$, a perturbative expansion of the coefficient $\alpha(h_z, \delta V)$ to lowest order yields $\alpha(h_z, V) \approx c_1\, \delta V + c_2\, h_z^2$, where a linear term in h_z vanishes due to inversion symmetry. Then the condition $\alpha(h_z, \delta V) = 0$ yields Eq. (2.5).

Apart from the high concentration of density of states, the bands supporting HOVHS display another interesting feature. As shown in Fig. 2.4, the real space wave functions for the energy states at the HOVHS and projected on the valleys $\pm\boldsymbol{K}$ are particularly polarized on two sublattices that form a honeycomb lattice localized between the maxima of the moiré potential. This sublattice polarization behavior is observed along the HOVHS line given by Eq. (2.5), and highlighted in Fig. 2.4 for $(h_z, V) = (0.5, 1.38)$. We note that this sublattice polarization in the vicinity of HOVHS on the TI surface states is a feature observed in other two-dimensional systems tight-binding systems such as in Haldane Chern insulators tuned to higher-order Lifshitz transitions [48] and kagomé bands. [69, 112]

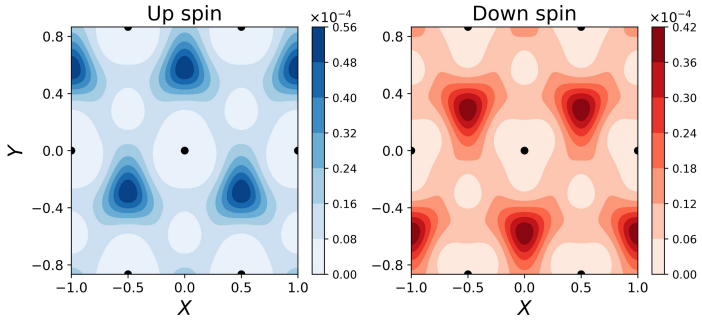

Figure 2.4: Real space wavefunction of the up (left) and down (right) spin electrons with momentum $\boldsymbol{K}$ on the HOVHS band of the C_6 symmetric model with $(h_z, V) = (0.5, 1.38)$ in units of (v_F/a). The difference in the maximum amplitude of the up and down spins can be attributed to the broken TRS. The maxima of the lattice potential are denoted with black dots.

2.1.2 C_3 symmetric moiré potential

We investigate the effects of breaking inversion symmetry such that $V(\boldsymbol{r}) \neq V(-\boldsymbol{r})$ by adding a contribution to the C_6 symmetric lattice potential given in Eq. (2.4) that yields a potential with C_3 symmetry

$$V_3(\boldsymbol{r}) = 2V \sum_{j=1}^{3} \Big[\cos\big(\boldsymbol{G}_j \cdot \boldsymbol{r}\big) - \cos\big(\boldsymbol{G}_j \cdot \boldsymbol{r} + \phi\big) \Big], \tag{2.8}$$

for any $\phi \neq 0, \pi$. Subsequently, we narrow our focus to the specific case where $\phi = \frac{2\pi}{3}$, as depicted in Fig. 2.5a.

In the absence of the Zeeman field, the C_3 symmetric model supports a gapless spectrum of moiré bands, wherein we uncover one band supporting a pair of HOVHS in the moiré Brillouin zone valleys when the strength of the moiré potential $V_3^{(0)} = V_3(h_z = 0) = 0.802(v_F/a)$. The existence of a pair of valley HOVHS follows from TRS degenerate states at $\pm\boldsymbol{K}$ despite breaking of inversion symmetry by the potential Eq. (2.8).

On turning the Zeeman field on with $V = V_3^{(0)}$, the HOVHS splits into 3

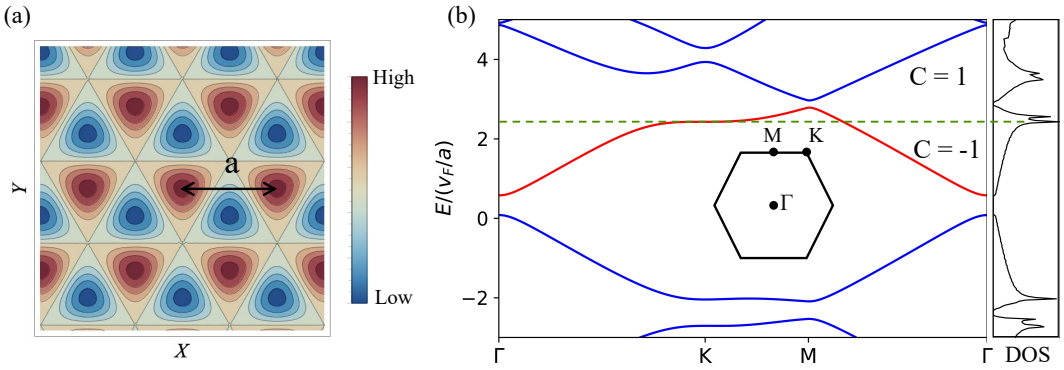

Figure 2.5: (a) Contour plot of the C_3 symmetric potential $V_3(\boldsymbol{r})$, given in Eq. (2.8), with superlattice constant a. (b) Band structure of the model given in Eq. (2.1b) with the C_3 periodic potential with $(h_z, V) = (0.5, 0.83)$ in units of (v_F/a), to the left and the corresponding DOS to the right. The sharp peak in the DOS at the $\boldsymbol{K}$ point indicates the presence of HOVHS while the shorter peak right above it in energy points towards the conventional VHS around the $\boldsymbol{K}'$ point. Here, the lowest conduction band (shown in red) that carries a Chern number of -1, hosts HOVHS located at the $\boldsymbol{K}$ points.

conventional VHS located around each of the $\boldsymbol{K}$ and $-\boldsymbol{K}$ points of the lowest conduction band which carries a Chern number of -1, as shown in Fig. 2.5b. By adjusting the lattice potential strength or the Zeeman field, the conventional VHS can merge back into a HOVHS. However, due to the breaking of inversion symmetry, this HOVHS is located in either one of the valleys. This situation is analogous to the effect of an inversion-breaking sublattice potential on the Haldane Chern insulator model that can lead to a single HOVHS on one of the valleys. [88]

Similarly to the approach of Sec. 2.1.1, we characterize the (h_z, V) parameter space for which the $C = -1$ band supports HOVHS in one of the valleys. For the $\boldsymbol{K}$ valley HOVHS, we uncover the relation between moiré potential and Zeeman field,

$$V_3(h_z) = V_3^{(0)} + \Gamma_1 h_z + \Gamma_2 h_z^2 + \Gamma_3 h_z^3 \,, \tag{2.9}$$

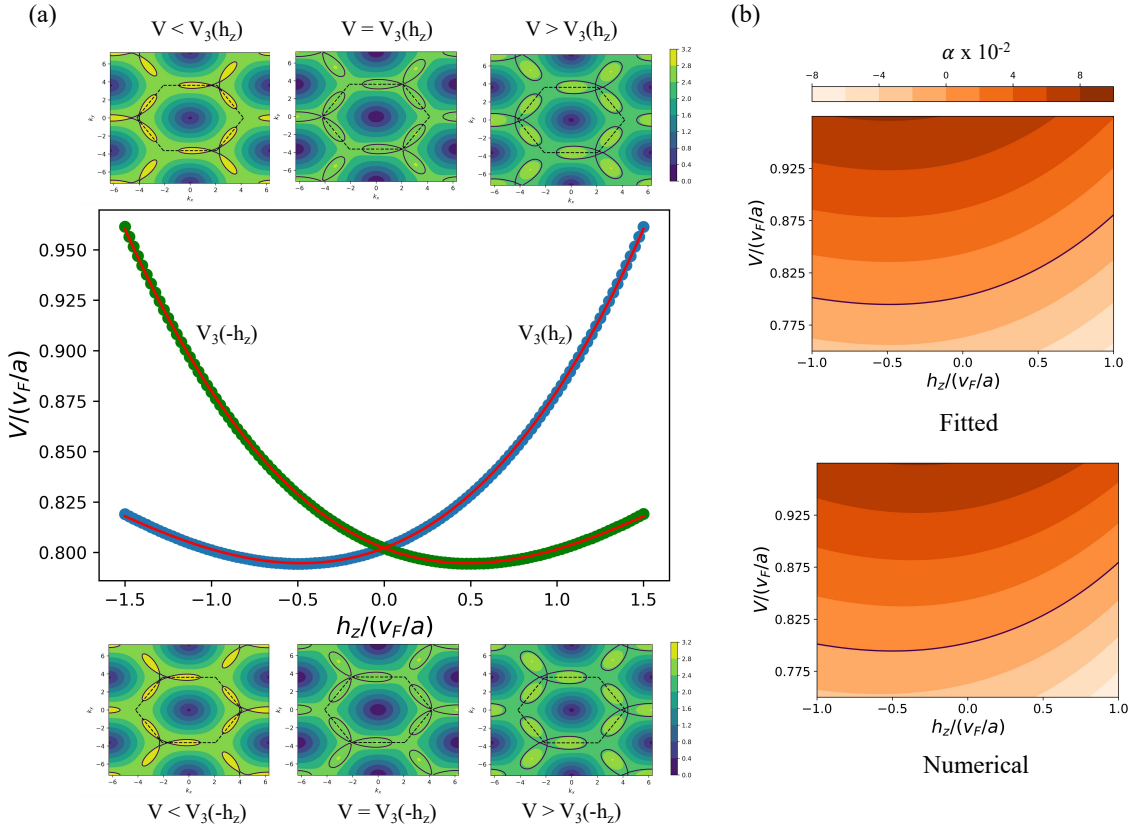

Figure 2.6: (a)Parameter space plot showing the values of the Zeeman mass (h_z) and the lattice potential strength (V) that corresponds to HOVHS located at the $\boldsymbol{K}$ (blue) and the $\boldsymbol{K'}$ (green) points of the BZ. The (h_z, V) pairs that support HOVHS located at K (K') follow a scaling relation $V_3(h_z)$ ($V_3(-h_z)$) given by Eq. (2.9). The contour plots of the Fermi surfaces corresponding to the regions- $V < V_3(h_z)$, $V = V_3(h_z \neq 0)$, and $V > V_3(h_z)$ are shown above, and those corresponding to the regions- $V < V_3(-h_z)$, $V = V_3(-h_z \neq 0)$, and $V > V_3(-h_z)$ are shown below. When $h_z = 0$ and $V = V_3^{(0)}$, we find HOVHS located at both $\boldsymbol{K}$ and $\boldsymbol{K'}$ points, as in the case of the C_6 symmetric lattice potential. Here, the dotted black lines indicate the boundaries of the first moiré Brillouin zone and the black lines show the Fermi surfaces passing through VHS. (b)$\alpha(h_z, V)$ obtained numerically from the expression given in Eq. (2.10) (top) and from the Taylor expansion of the energy dispersion around the $\boldsymbol{K}$ points (bottom). The thick black curve indicates the $\alpha(h_z, V) = 0$ line which, as expected, coincides with the $h_z - V$ curve corresponding to the emergence of HOVHS at the $\boldsymbol{K}$ point shown in (a).

in terms of numerically fitted coefficients $(\Gamma_1, \Gamma_2, \Gamma_3) \approx (0.033, 0.039, 0.007)$, and h_z and $V$are measured in units of (v_F/a). We note that unlike in the case discussed in Sec. 2.1.1, the breaking of inversion symmetry allows for terms with odd powers in h_z. Furthermore, while $(h_z, V_3(h_z))$ corresponds to a higher-order saddle point at the $\boldsymbol{K}$ point, $(h_z, V_3(-h_z))$ corresponds to the one at the $-\boldsymbol{K}$ point. In Fig. 2.6(a), we plot these curves and the character of the Fermi surface contours at and in the vicinity of the higher-order Lifshitz transitions.

Eq. (2.9), which describes the condition for the coefficient $\alpha(h_z, V)$ in Eq. (2.6) to vanish, can be well approximated by

$$\alpha(h_z, V) = \alpha_0 \ln\left[\frac{V}{V_3(h_z)}\right], \tag{2.10}$$

where $\alpha_0 \approx 0.4$ for $h_z a/v_F < 2$. Similarly, the Hessian vanishes at the $-\boldsymbol{K}$ points when $\alpha(h_z, V) = \alpha_0 \ln(V/V_3(-h_z))$ with $\alpha_0 \approx 0.4$. Thus, we have established a mechanism to create and access a larger landscape of HOVHS topological bands with Chern number $C = \pm 1$, which occur through the interplay of a moiré potential and a uniform Zeeman field coupled to the surface states a 3D topological insulator. In the next section, we discuss an important feature in anomalous Hall response implied by the existence of Van Hove singularities in Chern bands and apply it to the case of conventional and higher-order VHS.

2.2 Intrinsic Anomalous Hall Conductivity near Lifshitz Transitions

In this section, we discuss the manifestation of Lifshitz transitions in the context of anomalous transport in a Chern band. We establish a general result that relates the divergence in the density of states associated with Van Hove singularities to the

low-temperature differential anomalous Hall response, as expressed in Eqs.(2.17). While the discussion in this section applies generally to Chern bands, we specifically explore this connection for the HOVHS characterized in Sec. 2.1.

In Chern bands, the presence of non-zero Berry curvature of the Bloch states leads to an anomalous Hall velocity[100–102] when charges couples to an electric field, giving rise to the intrinsic anomalous Hall effect.[97–99] While for a filled Chern band insulator, this leads to a quantized Hall conductivity in units of e^2/h, in a partially filled Chern band, the intrinsic anomalous Hall conductivity σ_{xy}^{int} can be continuously tuned by the electronic filling of the Chern band, and it probes the Berry phase contribution of the occupied electronic states. In particular, when the Fermi energy crosses a Lifshitz transition in a Chern band, the large peak in the density of states entailed by the change in the topology of the Fermi surface suggests that the anomalous Hall response may correspondingly manifest some distinct property. Furthermore, this distinct behavior should be a generic feature of Chern bands, provided the sharp features in the density of states are not significantly rounded by disorder and thermal broadening. Thus, we hereafter discuss the character of the intrinsic anomalous Hall response of Chern bands at low temperatures and in cases where the anomalous Hall effect is dominated by the intrinsic contribution[99], where we uncover a characteristic feature relating the anomalous Hall conductivity and the density of states. Specifically, in the $T \to 0$ limit, we show that $d\,\sigma_{xy}^{\text{int}}/d\,\mu$ diverges when the Fermi energy μ crosses the scale of logarithmic and power-law Van Hove singularities. Also, in what follows, we assume that the system remains a Fermi liquid as the Fermi energy crosses a Van Hove singularity.

To establish these connections, we consider an isolated Chern band described by Bloch states $|u_{\boldsymbol{k}}\rangle$ with energy dispersion $\varepsilon(\boldsymbol{k})$ and non-vanishing Berry curvature $\Omega(\boldsymbol{k}) = \nabla_{\boldsymbol{k}} \times \boldsymbol{A}_{\boldsymbol{k}}$, where the Berry connection $\boldsymbol{A}_{\boldsymbol{k}} = i\,\langle u_{\boldsymbol{k}}|\,\nabla_{\boldsymbol{k}}\,|u_{\boldsymbol{k}}\rangle$. This system is

characterized by the intrinsic anomalous Hall conductivity [97]

$$\sigma_{xy}^{\text{int}}(\mu;T) = \frac{e^2}{h}\frac{1}{2\pi}\int d^2\boldsymbol{k}\,\Omega(\boldsymbol{k}) f_{\mu;T}(\varepsilon(\boldsymbol{k}))\,, \tag{2.11}$$

where the integral extends over the first Brillouin zone, e is the charge of the electron, h is Planck's constant and $f_{\mu;T}(\varepsilon(\boldsymbol{k})) = \left(e^{\frac{\varepsilon(\boldsymbol{k})-\mu}{k_B T}}+1\right)^{-1}$ is the Fermi distribution at temperature T and chemical potential μ.

In the $T \to 0$ limit, Eq. (2.11) becomes

$$\sigma_{xy}^{\text{int}}(\mu;0) = \frac{e^2}{h}\frac{1}{2\pi}\int d^2\boldsymbol{k}\,\Omega(\boldsymbol{k})\Theta(\mu-\varepsilon(\boldsymbol{k}))\,, \tag{2.12}$$

where $\Theta(x)$ is the Heaviside step function signaling a sharp separation between occupied and empty electronic states. This contribution varies continually with the Fermi energy μ when the Fermi energy lies between the minimum and maximum of the Chern band.

An insight can be obtained by considering differential anomalous Hall conductivity, which measures the slope of σ_{xy}^{int} as a function of Fermi energy,

$$\frac{d\sigma_{xy}^{\text{int}}(\mu;0)}{d\mu} = \frac{e^2}{h}\frac{1}{2\pi}\int d^2\boldsymbol{k}\,\Omega(\boldsymbol{k})\delta(\mu-\varepsilon(\boldsymbol{k}))\,. \tag{2.13}$$

Eq. (2.13) shows that at $T = 0$, the differential anomalous Hall conductivity gets its contribution from states at the one-dimensional Fermi surface manifold $\varepsilon(\boldsymbol{k}) = \mu$.

Upon normalizing by the density of states at the Fermi energy,

$$\rho(\mu) = \int d^2\boldsymbol{k}\,\delta(\mu-\varepsilon(\boldsymbol{k}))\,, \tag{2.14}$$

Eq. (2.13) reads

$$\frac{d\sigma_{xy}^{\text{int}}(\mu;0)}{d\mu} = \frac{e^2}{2\pi h}\langle\Omega\rangle_{FS}\,\rho(\mu)\,, \tag{2.15}$$

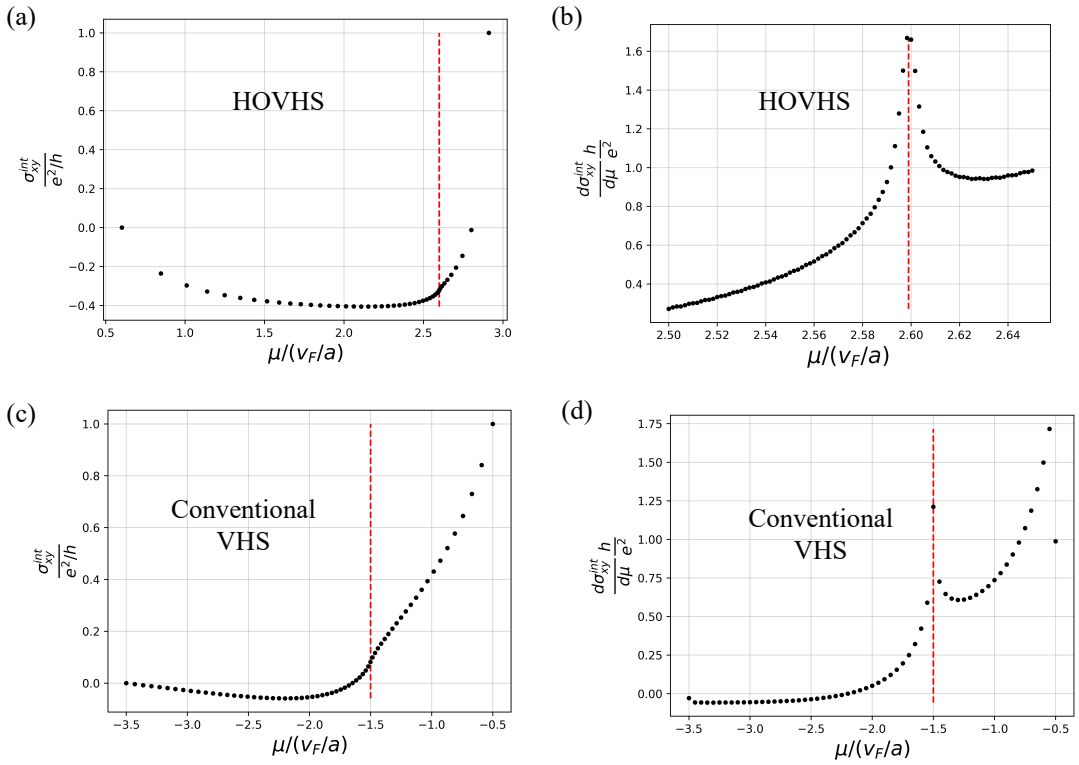

Figure 2.7: (a) Intrinsic anomalous Hall conductivity (σ_{xy}^{int}) and (b) differential anomalous Hall response ($\frac{d\sigma_{xy}^{\text{int}}}{d\mu}$), at zero temperature plotted as a function of the Fermi energy μ for the Chern band supporting HOVHS at $(h_z, V) = (0.5, 1.38)$ in units of (v_F/a). The dashed red line denotes the energy at which HOVHS occurs, μ_*. The differential anomalous Hall response exhibits a power law divergence around μ_*, as given in Eq. (2.17) (b), with $\nu = 0.39 \approx 1/3$, and $\kappa_+ = \kappa_- = 0.43$. (c) Intrinsic anomalous Hall conductivity (σ_{xy}^{int}) and (d) differential anomalous Hall response ($\frac{d\sigma_{xy}^{\text{int}}}{d\mu}$), at zero temperature plotted as a function of the Fermi energy μ for the lower energy band of the Chern insulator model defined on a square lattice of lattice constant a, $H = (v_F/a)[\sin k_x \sigma_x + \sin k_y \sigma_y + (m - \cos k_x - \cos k_y)\sigma_z]$ at $m = 1.5$ where it supports VHS at $\mu_* = -1.5(v_F/a)$ (denoted by the red dashed line) and carries a Chern number of 1. The differential anomalous Hall response exhibits a log divergence around μ_*, as given in Eq. (2.17) (a), with $\Lambda = 1.35(v_F/a) = 0.45\times$ bandwidth and $\rho_0 = \frac{0.58}{v_F/a}$. Note that in (a) and (c), as the Fermi reaches the top of the band, the total Hall conductivity approaches 1, the Chern number of the corresponding band.

where

$$\langle\Omega\rangle(\mu) \equiv \frac{\int d^2\boldsymbol{k}\,\Omega(\boldsymbol{k})\delta(\mu-\varepsilon(\boldsymbol{k}))}{\int d^2\boldsymbol{k}\,\delta(\mu-\varepsilon(\boldsymbol{k}))} \tag{2.16}$$

defines the average of the Berry curvature on the Fermi surface.

Eq. (2.15) provides an insightful connection between the average Berry curvature (which is the imaginary part of the quantum metric tensor), the density of states, and the anomalous Hall transport, which can be in principle explored to read out the Berry curvature by scanning the Fermi energy of the band. Moreover, let us consider the behavior of Eq. (2.15) in the vicinity of a Lifshitz transition occurring at energy μ^*. In this case, if $\langle\Omega\rangle(\mu^*) \neq 0$ (which we expect to occur typically in a Chern band), the differential anomalous Hall conductivity is dominated by the Van Hove singularities in the density of states, resulting in the following asymptotic forms for the conventional and higher-order Lifshitz transitions

$$\frac{d\sigma_{xy}(\mu;0)}{d\mu} \approx \frac{e^2}{2\pi h} \times \langle\Omega\rangle(\mu) \times \underbrace{\rho_0 \log(\Lambda/|\mu-\mu_*|)}_{\text{Conventional Lifshitz transition}}, \tag{2.17a}$$

$$\frac{d\sigma_{xy}(\mu;0)}{d\mu} \approx \frac{e^2}{2\pi h} \times \langle\Omega\rangle(\mu) \times \underbrace{\frac{\Theta(\mu-\mu_*)\kappa_+ + \Theta(\mu_*-\mu)\kappa_-}{|\mu-\mu_*|^\nu}}_{\text{Higher-order Lifshitz transition}}, \tag{2.17b}$$

where ν is a positive exponent and $\kappa_\pm$ coefficients for $\mu \geq \mu_*$ ($\mu \leq \mu_*$). Eq. (2.17) establishes a general connection between differential anomalous Hall response and Lifshitz transitions in Chern bands.

In Figure 2.7, we plot $d\sigma_{xy}^{\text{int}}/d\mu$ and $\sigma^{\text{int}}(\mu)$ as a function of the Fermi energy μ for two representative cases, namely, the Chern bands holding HOVHS discussed in Sec.2.1 and a two-band model Chern insulator model supporting logarithmic VHS [113, 114]. In the top panels of Figure 2.7, we observe that the cubic power-law divergence in the DOS for the topological insulator moiré surface Chern bands

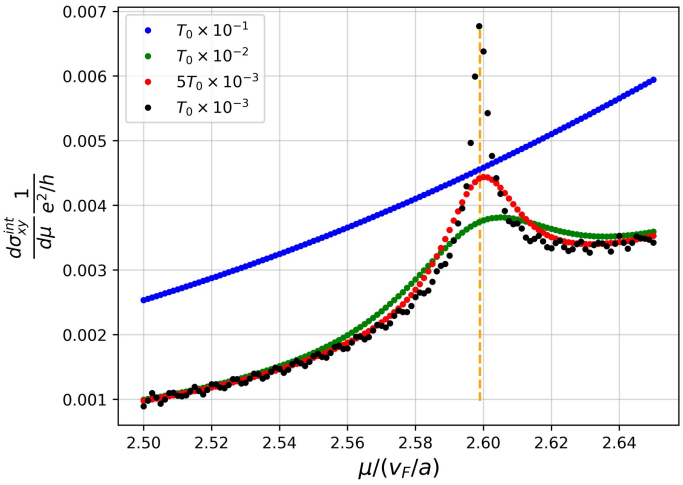

Figure 2.8: Differential anomalous Hall conductivity $\frac{d\sigma_{xy}^{\text{int}}}{d\mu}$ plotted against the Fermi energy μ for the HOVHS band with $(h_z, V) = (0.5, 1.38)$ in units of (v_F/a), for different values of temperature (T) that are labelled on the plot. The temperature T is scaled with $T_0 = (v_f/a)/k_B$ where k_B is the Boltzmann constant and $v_F/a \approx 30$ meV. [1, 2] The yellow dashed line denotes the energy at which the HOVHS occurs, μ_*. The peak in $\frac{d\sigma_{xy}^{\text{int}}}{d\mu}$ associated with the HOVHS gets progressively stronger as the temperature decreases.

gives rise to a pronounced peak in $d\sigma_{xy}^{\text{int}}/d\mu$ (Figure 2.7b), which then reflects a characteristic slope in σ_{xy}^{int} (Figure 2.7a) as the system undergoes a Lifshitz transition at $\mu = \mu^*$, which is indicated by the red dotted lines. In the bottom panels of Fig. 2.7, we perform a similar analysis for a Chern band with conventional logarithmic VHS. In both cases, the characteristic behavior by Eq. (2.17) is confirmed despite some numerical rounding introduced by the finite-size grid.

To account for the effects of thermal broadening, we obtain from Eq. (2.11) the temperature dependence of the differential anomalous Hall conductivity

$$\frac{d\,\sigma_{xy}^{\text{int}}}{d\,\mu}(\mu; T) = \frac{e^2}{2\pi\,h} \int d^2\,\boldsymbol{k}\,\Omega(\boldsymbol{k})\,\frac{1}{k_B\,T}\Big[2\,\cosh\frac{(\varepsilon(\boldsymbol{k}) - \mu)}{2\,k_B\,T}\Big]^{-2}, \tag{2.18}$$

where the last term in the integral accounts for the temperature dependence of the Fermi distribution.

In Figure 2.8 we plot the temperature dependence of the differential anomalous Hall conductivity Eq. (2.18) for the TI surface state discussed in Sec. 2.1.1 for the Chern band supporting a pair of HOVHS. As expected, for temperatures compared with or greater than the bandwidth $T \gtrsim T_0 \sim \Lambda/k_B$, where Λ is the bandwidth, thermal effects strongly destroy the effect of the VHS. However, with decreasing of temperature substantially below the bandwidth scale, the peak in $\frac{d\,\sigma_{xy}^{\text{int}}}{d\,\mu}$ becomes progressively more pronounced, allowing for the identification of a VHS, and asymptotically tending to a sharp peak as in $T \to 0$ limit described by Eq. (2.17).

2.3 Discussion and Outlook

In this work, we have identified a mechanism to create time-reversal broken topological Chern bands that host higher-order Van Hove singularities on the surface of a 3D topological insulator. We have shown that these HOVHS in topologically nontrivial bands can emerge from the interplay of a time-reversal breaking Zeeman field induced by the proximity to a ferromagnetic insulator and a time-reversal invariant moiré potential induced on the surface electrons of a three-dimensional topological insulator. The latter can naturally occur through the misalignment of the quintuple layers in Bi_2Se_3 and Bi_2Te_3, responsible for the onset of a nanometer scale moiré potential. Employing exact diagonalization and symmetry analysis, we have demonstrated that tuning of the Zeeman and moiré potential energy scales gives rise to a manifold of higher order Lifshitz transitions on the moiré Brillouin zone valleys. This setting opens a direction for future exploration of correlation effects associated with the presence of strong density of state singularities in moiré Chern bands on the surface of topological insulators.

Moreover, our analysis of HOVHS, which focuses on the surface of 3D TIs characterized by a single Dirac cone, offers a compelling opportunity for extension to 2D materials that exhibit multiple Dirac fermion flavors, such as twisted bilayer graphene [7, 115, 116] and transition metal dichalcogenides. [117, 118] Extending our mechanism to such 2D materials, where each Dirac cone can be treated as an independent or isolated one, would be particularly interesting. Additionally, our mechanism lays the groundwork for future research into designing Chern bands with HOVHS, beyond the constraint of a single Dirac cone.

Furthermore, we have identified a characteristic signature in the intrinsic anomalous Hall response as the Fermi surface crosses a Lifshitz transition. Specifically, the rate of change of the anomalous Hall conductivity as a function of the Fermi energy, $d\sigma_{xy}^{\text{int}}/d\mu$, displays a pronounced peak at low temperatures due to the large accumulation of states near the VHS, which tracks the logarithmic or power-law divergences in conventional and higher-order Lifshitz transitions, respectively. In the moiré surface Chern bands studied in this work, this entails a power-law divergence in $d\sigma_{xy}^{\text{int}}/d\mu$ as the temperature tends to zero. This relationship opens a route to experimentally probe VHS and Chern bands through transport measurements, and it would be not only applicable in the HOVHS on the surface of a topological insulator but also to a wider class of Hofstadter-Chern bands, [87, 119–132] and zero-field Chern bands in moiré heterostructures.[133–137]

Chapter 3

Classification of Higher-Order Van Hove Singularities in Kagome Topological Bands

Note: The material in this chapter is available on arXiv: arXiv:2410.07000.

Motivated by the growing interest in band structures featuring higher-order Van Hove singularities (HOVHS), we investigate a spinless fermion kagome system characterized by nearest-neighbor (NN) and next-nearest-neighbor (NNN) hopping amplitudes. While NN hopping preserves time-reversal symmetry, NNN hopping, akin to chiral hopping on the Haldane lattice, breaks time-reversal symmetry and leads to the formation of topological bands with higher Chern numbers. We perform analytical and numerical analysis of the energy bands near the high-symmetry points, which uncover a rich and complex landscape of HOVHS, controlled by the magnitude and phase of the NNN hopping. Furthermore, the NNN hopping induces the formation of higher Chern number bands in the middle of the spectrum obeying a sublattice interference.

The interplay between topological electronic bands and correlation effects pro-

vides a fruitful avenue to realizing unconventional phases driven by competing electronic states. The presence of a large density of states (DOS) provides an effective mechanism to enhance electronic correlations. In 2D lattices, Van Hove has shown that saddle points in the band dispersion lead to Van Hove singularities (VHS) characterized by logarithmic divergent DOS [6]. The possibility of higher-order VHS (HOVHS) displaying even stronger power-law divergent DOS, considered in the context of cuprate band structures [138, 139], has recently garnered significant interest as a pathway to explore unconventional electronic orders [28–40]. In particular, when HOVHS emerge in Chern bands [48, 88, 140], the interplay between band topology and high DOS can promote novel electronic orders, such as superconducting pair-density waves and Chern supermetals [48], which underscores the importance of higher-order singularities in topological bands for discovering new quantum phases. However, beyond initial studies on the Haldane lattice [48, 88] and topological insulator moiré surface states [140], the structure of HOVHS in Chern bands remains largely unexplored.

In this work, we extend this knowledge by investigating a rich scenario where band topology and HOVHS are intertwined in a 2D kagome system. Kagome lattices [59, 60], characterized by their geometrically frustrated network of corner-sharing triangles in two dimensions, support VHSs [39, 67], along with flat bands [61–65] and Dirac fermions [66, 67], which provide an ideal platform for studying complex electronic phenomena. The substantial enhancement of interaction effects due to the large accumulation of electronic states around the VHS plays a crucial role in the emergence of various electronic phenomena including charge density waves, pair density waves, and unconventional superconductivity [141–144].

We investigate the effects of a complex next-nearest-neighbor (NNN) hopping amplitude, $t_2\, e^{i\phi}$, on the electronic bands of a kagome lattice. This hopping term, analogous to the Haldane model on the honeycomb lattice [89], breaks time-reversal

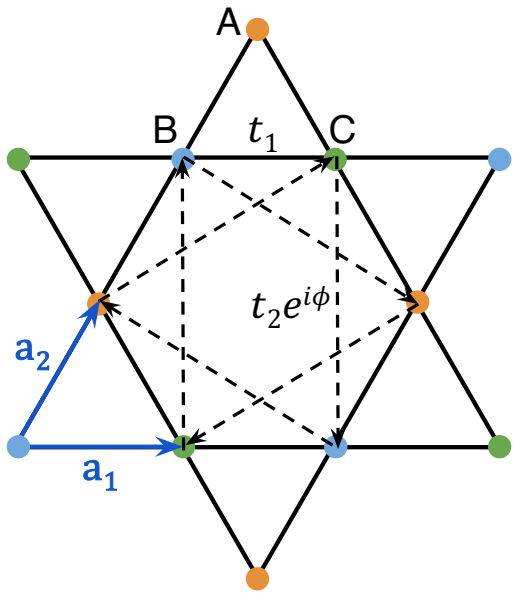

Figure 3.1: Kagome lattice with the sites A, B, and C marked in orange, blue, and green respectively. The vectors connecting site B with its nearest neighbors A and C are denoted as $\mathbf{a_2}$ and $\mathbf{a_1}$ respectively. The real NN hopping amplitude, t_1, is represented by solid black lines. The black dashed arrows show the orientation of the NNN hoppings with strength $t_2e^{i\phi}$. This NNN hopping breaks time-reversal symmetry while preserving $\mathcal{C}_3$ rotation and inversion symmetry about the center of the hexagon.

symmetry (TRS) and induces the formation of bands with non-zero Chern numbers. Employing a systematic analytical and numerical classification of critical points at high-symmetry points $\mathbf{\Gamma}$, $\pm\boldsymbol{K}$, and $\boldsymbol{M_i}$ ($i = 1, 2, 3$) of the Brillouin zone as a function of (t_2, ϕ), we reveal a rich landscape of HOVHS in this time-reversal broken kagome system. Notably, we identify conditions under which bands with Chern numbers as large as $C = \pm 4$, emerge. Owing to the presence of HOVHSs, these bands support power-law divergences in the DOS, $\rho(\epsilon) \sim |\epsilon|^{-\nu}$, with exponents $\nu = \frac{1}{2}$, $\frac{1}{3}$, and $\frac{1}{4}$. The classification of HOVHS reveals new features of the kagome band structure:

(1) In the lowest band, our classification of HOVHS not only identifies the loci of high DOS but also pinpoints the location of a nearly flat Chern band with $C = \pm 1$ in the (t_2, ϕ) parameter space. This provides an ideal scenario for exploring competing electronic orders and emergent fractional Chern insulators [145–149] in a partially filled band.

(2) The NNN chiral hopping, while breaking TRS, preserves the sublattice interference (SI) [69, 112, 150] of the second band for the entire parameter space (t_2, ϕ). SI implies that electronic states associated with $\boldsymbol{M_i}$ points at the Brillouin zone boundary are maximally localized on the sublattices A, B, and C, which has a non-trivial effect on interactions when the Fermi energy crosses a HOVHS at the $\boldsymbol{M_i}$ points at the zone boundary. Our work thus extends the mechanism of SI in time-reversal broken Chern bands from the Chern number $C = \pm 1$ band on the honeycomb lattice [48] into the realm of topological kagome bands supporting higher Chern numbers, $C = \pm 2$ and $C = \pm 4$.

(3) While the NNN hopping destroys the exact flatness condition of the third band in the nearest-neighbor (NN) kagome lattice [63–65] (a special case where all points in the Brillouin zone become critical at $t_2 = 0$), our phase diagram uncovers HOVHS lines at the high symmetry points $\boldsymbol{K}$ and $\boldsymbol{M_i}$ in the (t_2, ϕ) parameter space, which converge to a flat band at $(t_2 \to 0, \phi = \pm\pi/2)$. Thus the kagome lattice provides a

relevant setting to study the emergence of HOVHS near stronger DOS singularities due to flatbands.

This work opens a direction to explore exotic kagome bands in synthetic materials such as optical lattices [151]. In particular, an implementation of the complex NNN hopping akin to a Haldane optical lattices [152] could be achieved via periodic modulation using piezoelectric actuators. Moreover, the recent discovery of a new family of kagome metals, AV_3Sb_5 (A = K, Rb, Cs) displaying a variety of exotic correlated electronic phenomena [69–75] and exhibiting both conventional and higher-order Van Hove singularities [68, 76, 77], as evidenced by angle-resolved photoemission spectroscopy (ARPES) [38, 39], further motivates a deeper exploration of the HOVHS landscape in kagome lattices. While kagome systems have been actively studied in connection with Van Hove singularities, the relationship between VHS and non-trivial band topology in these materials remains largely unexplored.

Model – We study a tight-binding model of the kagome lattice with lattice constant a, consisting of NN hopping as well as complex NNN hopping,

$$H = -t_1 \sum_{\langle i,j \rangle} c_i^\dagger c_j - t_2 \sum_{\langle\langle i,j \rangle\rangle} e^{i\phi_{ij}} c_i^\dagger c_j + h.c., \tag{3.1}$$

where t_1 (t_2) is the NN (NNN) hopping strength, ϕ_{ij} is the phase factor associated with the NNN hopping between sites i and j, $\langle i,j \rangle$ and $\langle\langle i,j \rangle\rangle$ indicates the NN and NNN hopping respectively, and $c_j^\dagger$ is the fermionic creation operator at site j. The vectors connecting the NN atomic sites are defined as $\mathbf{a_1} = \frac{a}{2}(1,0)$, $\mathbf{a_2} = \frac{a}{4}(1,\sqrt{3})$ and $\mathbf{a_3} = \mathbf{a_1} - \mathbf{a_2}$, and the NNN hopping vectors are defined as $\mathbf{b_1} = \frac{a}{2}(0,\sqrt{3})$, $\mathbf{b_2} = \frac{a}{4}(3,-\sqrt{3})$, and $\mathbf{b_3} = -(\mathbf{b_1} + \mathbf{b_2})$, as shown in Fig. 3.1. Notice that the black dashed arrows shown in Fig. 3.1 denote the direction of the complex NNN hopping. Furthermore, we assume the system is spin-polarized, thereby omitting the spin

degree of freedom.

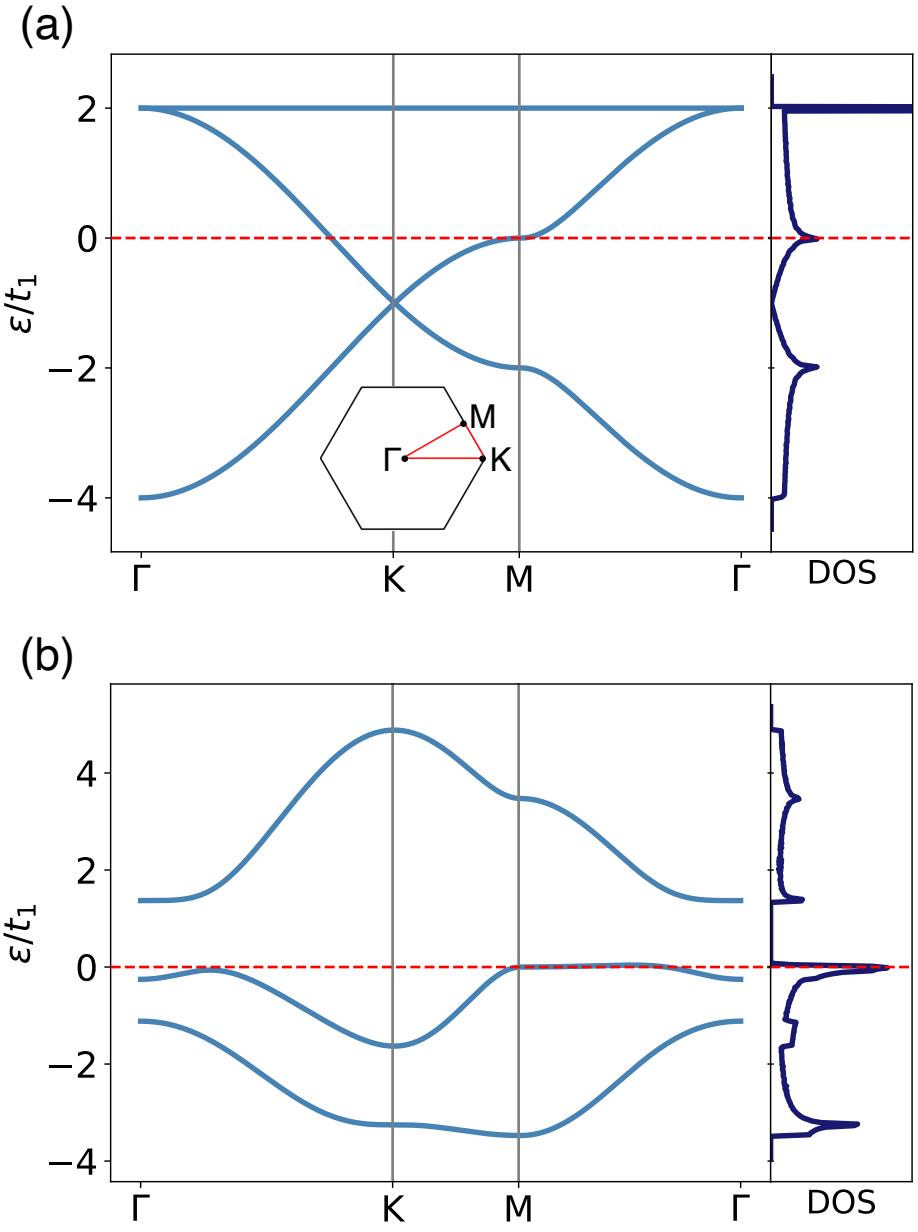

Figure 3.2: Band structure at (a) $(t_2, \phi) = (0, 0)$ and (b) $(t_2, \phi) = (0.76, 0.9\pi)$, with the first BZ shown in (a). The corresponding DOS is displayed on the right. The red dashed lines in (a) and (b) denote the energy at which the $\boldsymbol{M}$ points of the second band support a conventional VHS and a HOVHS respectively, as indicated by the divergences in the corresponding DOS. Notice that the energy corresponding to the $\boldsymbol{M}$ points on band 2 is always zero.

In the momentum space, the Hamiltonian reads $H = \sum_{\boldsymbol{k}} c^{\dagger}_{\mathbf{k}} \hat{\mathcal{H}}(\boldsymbol{k}) c_{\mathbf{k}}$, where

$\hat{\mathcal{H}}(\boldsymbol{k}) = \hat{\mathcal{H}}_{NN}(\boldsymbol{k}) + \hat{\mathcal{H}}_{NNN}(\boldsymbol{k})$, and $c_{\mathbf{k}} = (c_{\mathbf{k},\mathrm{A}} \;\; c_{\mathbf{k},\mathrm{B}} \;\; c_{\mathbf{k},\mathrm{C}})^T$, with A, B, C being the three sites of the kagome unit cell displayed in Fig. 3.1. The momentum $\boldsymbol{k}$ is defined in the first Brillouin zone (BZ) spanned by the two reciprocal lattice vectors, $\mathbf{G_1} = \frac{2\pi}{a}(1, -\frac{1}{\sqrt{3}})$ and $\mathbf{G_2} = \frac{2\pi}{a}(0, \frac{2}{\sqrt{3}})$. The lattice constant a will henceforth be set to 1. The single particle Hamiltonian $\hat{\mathcal{H}}(\boldsymbol{k})$ can be expressed as

$$\hat{\mathcal{H}}(\boldsymbol{k}) = \begin{pmatrix} 0 & h_{12}(\boldsymbol{k}) & h_{13}(\boldsymbol{k}) \\ h_{12}^*(\boldsymbol{k}) & 0 & h_{23}(\boldsymbol{k}) \\ h_{13}^*(\boldsymbol{k}) & h_{23}^*(\boldsymbol{k}) & 0 \end{pmatrix}, \tag{3.2}$$

where $h_{12}(\boldsymbol{k}) = -2\,t_1\,\cos(\boldsymbol{k}\cdot\boldsymbol{a}_2) - 2\,t_2\,e^{i\phi}\,\cos(\boldsymbol{k}\cdot\boldsymbol{b}_2)$, $h_{13}(\boldsymbol{k}) = -2\,t_1\,\cos(\boldsymbol{k}\cdot\boldsymbol{a}_3) - 2\,t_2\,e^{-i\phi}\,\cos(\boldsymbol{k}\cdot\boldsymbol{b}_3)$, and $h_{23}(\boldsymbol{k}) = -2\,t_1\,\cos(\boldsymbol{k}\cdot\boldsymbol{a}_1) - 2\,t_2\,e^{i\phi}\,\cos(\boldsymbol{k}\cdot\boldsymbol{b}_1)$.

Diagonalization of the Hamiltonian given in Eq. (3.2), $H = \sum_{\boldsymbol{k}}\sum_{n=1,2,3}\Psi^\dagger_{n,\mathbf{k}}\epsilon_{n,\mathbf{k}}\Psi_{n,\mathbf{k}}$, yields the dispersion of each band, $\epsilon_{n,\mathbf{k}}$, where $n = 1, 2, 3$ denotes the index of the first, second and third energy bands, respectively, in ascending order. Henceforth, energy is expressed in units of t_1. Owing to $\mathcal{C}_3$ rotation and inversion symmetries, the spectrum satisfies $\epsilon_{n,\mathcal{C}_3\mathbf{k}} = \epsilon_{n,\mathbf{k}}$ and $\epsilon_{n,-\mathbf{k}} = \epsilon_{n,\mathbf{k}}$.

3.1 Classification of Higher Order Van Hove Singularities

In 2D Bloch bands, an ordinary VHS exhibits logarithmic divergence in the DOS ($\rho \propto \log|\epsilon|$) [6], which occurs at a saddle point (i.e., where the dispersion is locally $\epsilon_{n,\boldsymbol{k}} \sim k_x^2 - k_y^2$), with the following conditions satisfied: $\nabla_{\mathbf{k}}\epsilon_{n,\mathbf{k}} = 0$ and $\mathbb{H}_{n,\mathbf{k}} < 0$, where $\mathbb{H}_{n,\mathbf{k}} = \det(\frac{\partial^2\epsilon_{n,\mathbf{k}}}{\partial k_i \partial k_j})$ is the Hessian of the dispersion $\epsilon_{n,\mathbf{k}}$. The vanishing of the Hessian at the critical point signals the degeneracy of the quadratic form and the formation of a HOVHS with power-law divergence in DOS [28–30, 110] due to a

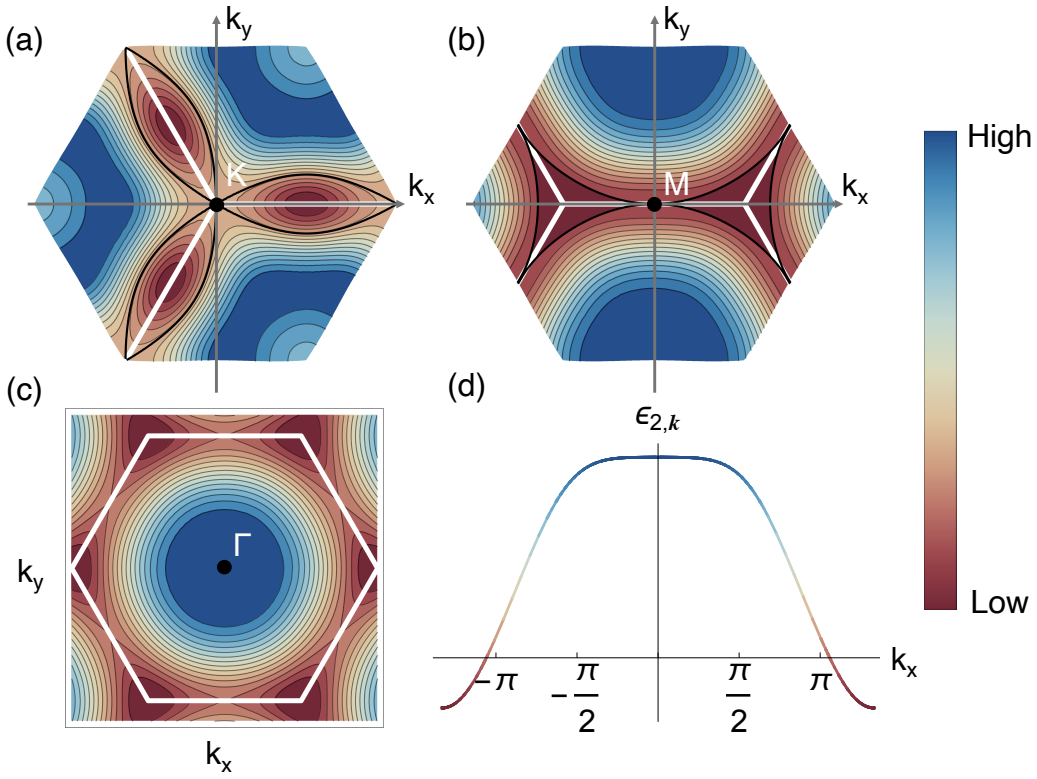

Figure 3.3: Contour plots of the energy dispersion corresponding to band 2, near the high-symmetry points (a) $\pm\boldsymbol{K}$, (b) $\boldsymbol{M_i}$, and (c) $\boldsymbol{\Gamma}$ points, where the Hessian vanishes, thereby supporting HOVHS. The white lines denote the boundaries of the first BZ and the black lines correspond to the Fermi surface contour at the corresponding energy of the HOVHS. At the $\boldsymbol{K}$ point (a), the dispersion exhibits a monkey-saddle dispersion. In contrast, around the $\boldsymbol{M_3}$ point (b), the dispersion becomes locally flat only along the k_x direction. At the $\boldsymbol{\Gamma}$ point (c), which is an extremum, the second-order curvature of the dispersion vanishes along both k_x and k_y directions. (d) The energy dispersion considered in (c), around the $\boldsymbol{\Gamma}$ point, plotted along k_x with k_y held constant at zero, in order to highlight the flatness of the band around the $\boldsymbol{\Gamma}$ point.

higher-order critical point.

In the absence of NNN hopping, as shown in Fig. 3.2 (a), band 3 is flat and bands 1 and 2 support critical points on the high-symmetry points of the first BZ $\mathbf{\Gamma} = (0,0)$, $\pm\mathbf{K} = (\pm\frac{4\pi}{3}, 0)$, $\mathbf{M_1} = (\pi, \frac{\pi}{\sqrt{3}})$, $\mathbf{M_2} = (-\pi, \frac{\pi}{\sqrt{3}})$, and $\mathbf{M_3} = (0, -\frac{2\pi}{\sqrt{3}})$, with conventional saddle points located on $\boldsymbol{M_i}$. Fig. 3.2 (b) illustrates the effect of the NNN hopping on the band structure, where we observe the onset of bands with significantly higher DOS divergence than ordinary VHS. Henceforth we focus on addressing how these critical points emerge as a function of the parameters (t_2, ϕ). As shown below, all high-symmetry points on the three bands can support HOVHS in this parameter space. In particular, we analyze high-symmetry points separately and classify their HOVHS as shown in Fig. 3.3. $\mathcal{C}_3$ rotation and inversion symmetries, reduce the analysis to three of the six high-symmetry points.

3.1.1 Critical points at $\pm\mathbf{K}$

Higher-order singularities emerge at $\boldsymbol{K}$ in the form of monkey saddles, as shown in Fig. 3.3 (a). The corresponding low-energy dispersion, which reflects the $\mathcal{C}_3$ rotation symmetry around the $\boldsymbol{K}$ points, takes the form

$$\epsilon_{\mathbf{K}+\mathbf{p}} - \epsilon_{\mathbf{K}} = \alpha(p_x^3 - 3p_x p_y^2) + \cdots, \tag{3.3}$$

where p_x and p_y are defined parallel and perpendicular to the $\mathbf{\Gamma}\boldsymbol{K}$ line in the first Brillouin zone, respectively, and the coefficient α is real. This monkey saddle dispersion indicates that the corresponding DOS exhibits a power-law divergence with exponent $\nu = 1/3$ [28, 110, 153, 154], which we confirm numerically. Furthermore, these observations apply to the $-\boldsymbol{K}$ points as well, since the model is symmetric under inversion.

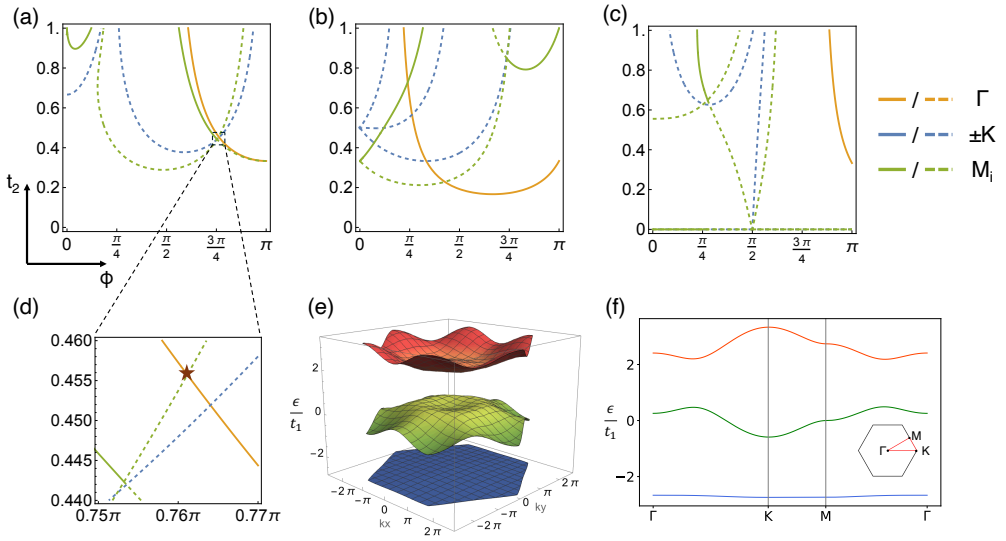

Figure 3.4: (a)-(c) Parameter space plots showing the set of (t_2, ϕ) values for which the the high-symmetry points $\mathbf{\Gamma}$(orange), $\pm\boldsymbol{K}$ (blue) and $\boldsymbol{M}$(green) corresponding to the bands 1-3 (from left to right) support HOVHSs. The dashed lines correspond to the high-symmetry points which can be classified as higher-order saddles whereas the solid lines correspond to extrema with vanishing Hessian. (d) Parameter space plot zoomed in around the intersections of the lines highlighted with the black dashed lines in (a), clarifying the different intersections of boundary lines. The parameter pair of interest is labeled with $\star$, with values $(t_2 = 0.45, \phi = 0.76\pi)$. (e) The 3D plot of the band structure at parameters labeled with $\star$ in (d), supporting HOVHSs at both $\boldsymbol{M}$ and $\mathbf{\Gamma}$ points. (f) Band diagram of the same bands to showcase the exceptional flatness of band 1, with an approximate bandwidth of $0.08\, t_1$. The first BZ is shown in the diagram as well.

3.1.2 Critical points at Γ

In contrast to the $\pm\boldsymbol{K}$ points, the $\mathbf{\Gamma}$ point does not support a high-order saddle even though the Hessian $\mathbb{H}_{n,\mathbf{\Gamma}}$ vanishes. Instead, as the second-order curvature of the dispersion vanishes along both the k_x and k_y directions, $\mathbf{\Gamma}$ becomes an extremum with vanishing Hessian, thereby resulting in a locally flat band around the $\mathbf{\Gamma}$ point, as shown in Fig. 3.3 (c). The corresponding low-energy dispersion takes the form,

$$\epsilon_{\mathbf{\Gamma}+\mathbf{p}} - \epsilon_{\mathbf{\Gamma}} = \alpha(p_x^2 + p_y^2)^2 = \alpha\, p^4 \tag{3.4}$$

where α is a real parameter and $(p_x, p_y) = p\,(\cos\theta, \sin\theta)$. Furthermore, the dispersion exhibits a stronger power-law divergence with exponent $\nu = 1/2$, i.e, $\rho(\epsilon) \propto |\epsilon - \epsilon_{\mathbf{\Gamma}}|^{-\frac{1}{2}}$. Additionally, we notice one particular instance at $(t_2\,, \phi) = (1/3\,, \pi)$ for the first band where the coefficient α vanishes resulting in a low-energy dispersion of the form (up to $\mathcal{O}(p^6)$)

$$\epsilon_{\mathbf{\Gamma}+\mathbf{p}} - \epsilon_{\mathbf{\Gamma}} \approx \frac{p_x^6}{1152} - \frac{p_x^4 p_y^2}{192} + \frac{p_x^2 p_y^4}{128} = \frac{p^6}{1152}\cos^2(3\,\theta)\,, \tag{3.5}$$

where $\epsilon_{\mathbf{\Gamma}} = -\frac{8}{3}$, and the corresponding DOS diverges around $\mathbf{\Gamma}$ as $\rho(\epsilon) \sim |\epsilon - \epsilon_{\mathbf{\Gamma}}|^{-2/3}$. We note that both expressions Eqs. (3.4) and (3.5) obey inversion and $\mathcal{C}_3$ rotation symmetries.

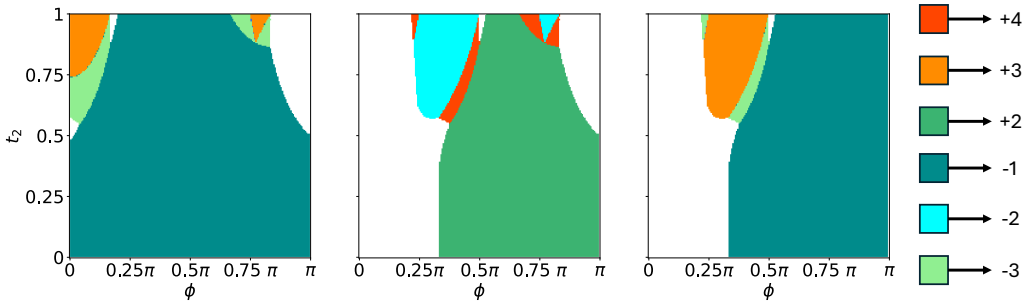

Figure 3.5: Phase diagrams for band 1 (left), band 2 (middle), and band 3 (right), showing the Chern numbers in the t_2-ϕ parameter space. White regions indicate non-positive indirect energy gaps where the Chern number is not well-defined. Only $[0, \pi]$ is shown on the ϕ axis, since for any Chern number C at (t_2, ϕ), as ϕ goes to $-\phi$, the Chern number flips sign. As seen in certain regions of the parameter space, band 2 can support Chern number as high as ± 4.

3.1.3 Critical points at $\mathbf{M_i}$

The emergence of HOVHS at $\boldsymbol{M_i}$ points occurs under two conditions: when either one or both of the eigenvalues of the Hessian $\mathbb{H}_{n,\boldsymbol{M_i}}$ vanish. Given the model has $\mathcal{C}_3$ symmetry, the following discussion applies to all the $\boldsymbol{M_i}$ points, and hence we drop the subscript i for the $\boldsymbol{M_i}$ points. When one eigenvalue vanishes, the second-order

curvature of the dispersion vanishes along either the k_x or k_y direction, resulting in a locally flat band structure in that direction, as shown in Fig. 3.3 (b). The corresponding low-energy dispersion takes the form,

$$\epsilon_{\mathbf{M}+\mathbf{p}} - \epsilon_{\mathbf{M}} = \begin{cases} \alpha p_x^2 + \beta p_x^4 + \gamma p_x^2 p_y^2 + \delta p_y^4 + \cdots, & \partial_{ky}^2 \epsilon_{n,\mathbf{M}} = 0 \\ \alpha p_y^2 + \beta p_x^4 + \gamma p_x^2 p_y^2 + \delta p_x^4 + \cdots, & \partial_{kx}^2 \epsilon_{n,\mathbf{M}} = 0 \end{cases}, \tag{3.6}$$

with all coefficients being real, where the DOS diverges around $\boldsymbol{M}$ as $\rho(\epsilon) \sim |\epsilon - \epsilon_{\boldsymbol{M}}|^{-1/4}$. On the other hand, when both eigenvalues vanish, the α coefficient vanishes, leading to a fourth-order dispersion in momentum, where the DOS obeys a power-law divergence with exponent $\nu = 1/2$, similar to the case of the $\mathbf{\Gamma}$ point.

3.1.4 HOVHS Phase Diagrams

We numerically calculate the Hessian for the band dispersions corresponding to the Hamiltonian in Eq. (3.2) around the high-symmetry points $\pm\boldsymbol{K}$, $\mathbf{\Gamma}$, and $\boldsymbol{M}$. Our analysis reveals a range of (t_2, ϕ) values, shown in Fig. 3.4 (a)-(c), for which all three bands support HOVHS at one or more of these high-symmetry points. The critical points marked by the HOVHS lines in Fig. 3.4 (a)-(c) all correspond to a vanishing Hessian. Dashed lines indicate higher-order saddle points, while solid lines denote higher-order extrema. Notice that the higher-order critical point at $\mathbf{\Gamma}$ is invariably an extremum, whereas those at $\pm\boldsymbol{K}$ are consistently higher-order saddles. Additionally, we find that the Hessian is invariant under the transformation $\phi \to -\phi$. As a result, we display the HOVHS lines for only $0 \leq \phi \leq \pi$.

In particular, we notice a region in Fig. 3.4 (a) where numerous line intersections occur, for the first band. That region is zoomed in and shown in Fig. 3.4 (d). Coincidentally, the band width in that region also achieves a minimum as low as

$\approx 0.08\, t_1$. Selecting a parameter pair of $(t_2 = 0.45, \phi = 0.76\pi)$, which is marked with $\star$ in Fig. 3.4 (d), we obtain a band 1 giving rise to HOVHSs both at $\mathbf{\Gamma}$ and $\boldsymbol{M}$ points. The 3D plot of the band structure is showcased in Fig. 3.4 (e), and the 1D band structure of the system is demonstrated in Fig. 3.4 (f), exhibiting the extreme flatness of the lowest band. The particular region shown in Fig. 3.4 (d) can be a promising territory to observe strongly correlated phenomena in the system.

We now discuss an analytic approach underlying the phase diagrams shown in Fig. 3.4 (a)-(c). In particular, we perturbatively determine the quadratic form near each high-symmetry point. For concreteness, we focus on the $\mathbf{\Gamma}$ point, where non-degenerate perturbation theory holds, except when degeneracies occur between bands 2 and 3 at $\phi = 0, \pi$. Expanding the Hamiltonian about $\mathbf{\Gamma}$, we get

$$\hat{\mathcal{H}}(\mathbf{\Gamma} + \boldsymbol{p}) = \hat{\mathcal{H}}(\mathbf{\Gamma}) + \hat{\mathcal{H}}(\boldsymbol{p})\,, \tag{3.7}$$

$$\hat{\mathcal{H}}(\boldsymbol{p}) = \begin{pmatrix} 0 & \zeta_{12}(\boldsymbol{p}) & \zeta_{13}(\boldsymbol{p}) \\ \zeta_{12}^*(\boldsymbol{p}) & 0 & \zeta_{23}(\boldsymbol{p}) \\ \zeta_{13}^*(\boldsymbol{p}) & \zeta_{23}^*(\boldsymbol{p}) & 0 \end{pmatrix}, \tag{3.8}$$

where, up to second order in momentum, $\zeta_{12} = t_1(\boldsymbol{p}\cdot\boldsymbol{a_2})^2 + t_2 e^{i\phi}(\boldsymbol{p}\cdot\boldsymbol{b_2})^2$, $\zeta_{13} = t_1(\boldsymbol{p}\cdot\boldsymbol{a_3})^2 + t_2 e^{-i\phi}(\boldsymbol{p}\cdot\boldsymbol{b_3})^2$, $\zeta_{23} = t_1(\boldsymbol{p}\cdot\boldsymbol{a_1})^2 + t_2 e^{i\phi}(\boldsymbol{p}\cdot\boldsymbol{b_1})^2$. The eigenstates of $\hat{\mathcal{H}}(\mathbf{\Gamma})$ can be expressed as, $\Psi^{(0)}_{1,\mathbf{\Gamma}} = \frac{1}{\sqrt{3}}(1,1,1)$, $\Psi^{(0)}_{2,\mathbf{\Gamma}} = \left(\frac{1}{6}\left(-\sqrt{3}-3i\right), \frac{1}{6}\left(-\sqrt{3}+3i\right), \frac{1}{\sqrt{3}}\right)$, and $\Psi^{(0)}_{3,\mathbf{\Gamma}} = \left(\frac{1}{6}\left(-\sqrt{3}+3i\right), \frac{1}{6}\left(-\sqrt{3}-3i\right), \frac{1}{\sqrt{3}}\right)$. The dispersion, to leading quadratic order, follows from

$$\epsilon_{n,\mathbf{\Gamma}+\boldsymbol{p}} = \epsilon^{(0)}_{n,\mathbf{\Gamma}} + \Psi^{(0)*}_{n,\mathbf{\Gamma}}\hat{\mathcal{H}}(\boldsymbol{p})\Psi^{(0)}_{n,\mathbf{\Gamma}}. \tag{3.9}$$

and, hence, the Hessian $\mathbb{H}_{n,\mathbf{\Gamma}}(t_2,\phi)$ of each band:

$$\begin{aligned}
\mathbb{H}_{1,\mathbf{\Gamma}} &= \left[\frac{3}{4}\left(t_1 + 3t_2\cos(\phi)\right)\right]^2, \\
\mathbb{H}_{2,\mathbf{\Gamma}} &= \left[-\frac{1}{8}t_1\left(1 + 3t_2\cos(\phi) - 3\sqrt{3}t_2\sin(\phi)\right)\right]^2, \\
\mathbb{H}_{3,\mathbf{\Gamma}} &= \left[-\frac{1}{8}t_1\left(1 + 3t_2\cos(\phi) + 3\sqrt{3}t_2\sin(\phi)\right)\right]^2.
\end{aligned} \tag{3.10}$$

Setting $\mathbb{H}_{n,\mathbf{\Gamma}} = 0$, results in the HOVHS contours at $\mathbf{\Gamma}$ shown in Fig. 3.4 (orange lines),

$$\begin{aligned}
\tau_{1,\mathbf{\Gamma}}(\phi) &= -\frac{\sec(\phi)}{3}, \\
\tau_{2,\mathbf{\Gamma}}(\phi) &= -\frac{1}{3(\cos(\phi) - \sqrt{3}\sin(\phi))}, \\
\tau_{3,\mathbf{\Gamma}}(\phi) &= -\frac{1}{3(\cos(\phi) + \sqrt{3}\sin(\phi))}.
\end{aligned} \tag{3.11}$$

The other high-symmetry points can be dealt with similarly. In particular, the analysis of degenerate perturbation theory for $\mathbf{\Gamma}$ at $\phi = \pi$, as well as the Hessian expressions for $\boldsymbol{M}$ and $\boldsymbol{K}$ points are provided in Appendix. A.

3.2 Band Topology

The NNN hopping breaks time-reversal symmetry and leads to the possibility of energy-isolated topological bands characterized by a non-zero Chern number. To investigate that, we numerically compute [155] the Chern number of the three bands in the $t_2 - \phi$ parameter space.

The Chern number diagrams are presented in Fig. 3.5. We restrict our analysis to $0 \leq t_2 \leq 1$ where the magnitude of the second neighbor hopping is less than the NN hopping t_1. Furthermore, the parameter ϕ is restricted from $[0, \pi]$, since for any Chern number C at (t_2, ϕ), as ϕ goes to $-\phi$, the Chern number flips sign. The white

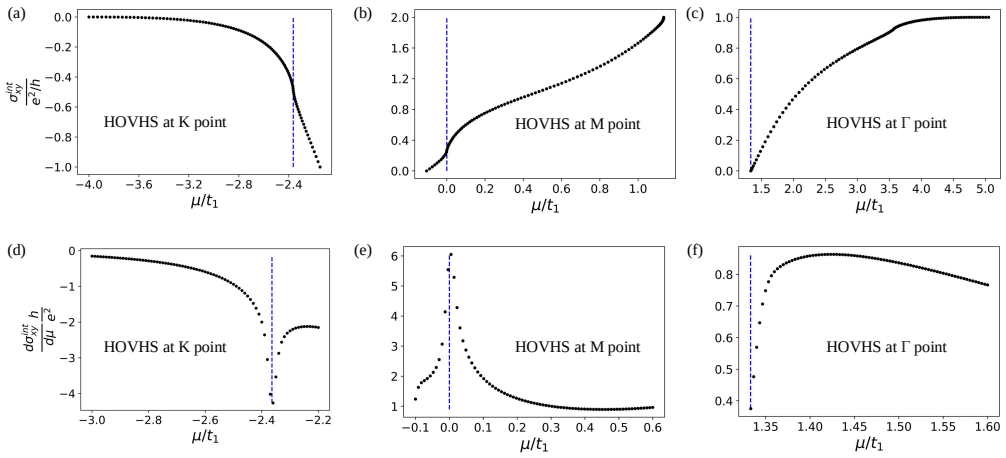

Figure 3.6: (a-c) Intrinsic anomalous Hall conductivity $\sigma_{xy}^{\text{int}}(\mu;0)$ and (d-f) the corresponding differential anomalous Hall conductivity $\frac{d\sigma_{xy}^{\text{int}}(\mu;0)}{d\mu}$ at zero temperature, plotted as a function of the Fermi energy μ in units of t_1 for the Chern bands supporting HOVHS at $(t_2, \phi) = (0.39, \pi/2)$ for band 1 (left), $(t_2, \phi) = (0.26, \pi/2)$ for band 2 (middle) and $(t_2, \phi) = (0.80, -0.9\pi)$ for band 3 (right). The high-symmetry point where the HOVHS is located is mentioned in each plot. The differential anomalous Hall response, like the corresponding DOS, exhibits a power-law divergence around μ^* (marked by the blue dashed line) with exponents $1/3$, $1/4$ and $1/2$ for $\boldsymbol{K}$, $\boldsymbol{M}$ and $\boldsymbol{\Gamma}$ point respectively.

regions describe bands that are not separated by a direct gap. The colored regions represent isolated bands with non-zero Chern numbers. In this parameter regime, we observe a rich landscape of gapped topological bands, some of which support relatively large Chern numbers.

By combining the phase diagrams shown in Fig. 3.4 and Fig. 3.5, we uncover a comprehensive understanding of how the NNN hopping leads to the onset of topological bands supporting HOVHS at the high-symmetry points, characterized by power-law diverging DOS $\rho(\epsilon) \sim |\epsilon - \epsilon_0|^{-\nu}$, with exponents $\nu = 1/2, 1/4, 1/3$, which is one of the main results of our analysis.

This structure of HOVHS can be accessed upon changing the Fermi energy in each of the bands, which also changes the anomalous Hall response owing to the

presence of a finite Berry curvature in the bands. Importantly, the zero temperature differential anomalous Hall response displays a strong divergence whenever the Fermi level crosses a Van Hove singularity, due to the large change in the number of electronic states in a small energy window. At zero-temperature, this response, $\frac{d\sigma_{xy}^{\text{int}}(\mu;T=0)}{d\mu}$, near VHSs can be expressed in terms of the density of states $\rho(\mu)$ as [140]

$$\frac{d\sigma_{xy}^{\text{int}}(\mu;T=0)}{d\mu} = \frac{e^2}{2\pi h}\,\langle\Omega\rangle_{FS}\,\rho(\mu)\,, \tag{3.12}$$

where $\sigma_{xy}^{\text{int}}(\mu;T=0) = \frac{e^2}{h}\frac{1}{2\pi}\int d^2\boldsymbol{k}\,\Omega(\boldsymbol{k})\Theta(\mu-\epsilon(\boldsymbol{k}))$ is the anomalous Hall conductivity at zero-temperature, defined in terms of the Berry curvature $\Omega(\boldsymbol{k})$, and $\langle\Omega\rangle_{FS}$ defines the average of the Berry curvature on the Fermi surface.

In Fig. 3.6, we plot $\sigma_{xy}^{\text{int}}(\mu;0)$ as well as $\frac{d\sigma_{xy}^{\text{int}}(\mu;0)}{d\mu}$ as a function of the Fermi energy μ for three different cases where a Chern band supports HOVHS at either of the three high-symmetry points. Notice that in all the three cases, the inverse of the slope of the anomalous Hall response $\sigma_{xy}^{\text{int}}(\mu;0)$ vanishes as $\mu \to \mu^*$ where μ^* is the energy corresponding to the HOVHS, shown in Figs. 3.6 (a)-(c). As a result, the $\frac{d\sigma_{xy}^{\text{int}}(\mu;0)}{d\mu}$ plots show a divergence as $\mu \to \mu^*$, displayed in Figs. 3.6 (d)-(f).

We numerically confirm that the differential anomalous Hall responses exhibit power-law divergences with the same exponent as the corresponding DOS, and note that the distinctly sharp peaks become progressively broadened as temperature increases.

3.3 Sublattice Interference

A remarkable feature of Kagome systems is that Bloch states of the second band corresponding to each $\boldsymbol{M_i}$ point in the Brillouin zone are maximally localized on one of the three sublattices A, B and C. Notably, this form of sublattice interference

(SI) [69, 112, 143] is persistent even with long-range real hopping terms extending up to the third nearest neighbor [112]. However, SI in kagome systems supporting topological bands is yet to be explored. In this section, we investigate the rich interplay between SI and HOVHS promoted by the complex hopping.

First, we establish that the SI *persists on band 2 throughout the t_2-ϕ parameter space*. For instance, consider the high-symmetry point $\boldsymbol{M_1} = (\pi, \frac{\pi}{\sqrt{3}})$. Working out the dot product of $\boldsymbol{M_1}$ with the lattice vectors $\boldsymbol{a_i}$ and $\boldsymbol{b_i}$, $\boldsymbol{M_1} \cdot \boldsymbol{a_1} = \pi/2$, $\boldsymbol{M_1} \cdot \boldsymbol{a_2} = \pi/2$, $\boldsymbol{M_1} \cdot \boldsymbol{a_3} = 0$, $\boldsymbol{M_1} \cdot \boldsymbol{b_1} = \pi/2$, $\boldsymbol{M_1} \cdot \boldsymbol{b_2} = \pi/2$ and $\boldsymbol{M_1} \cdot \boldsymbol{b_3} = -\pi$, yields the Hamiltonian $\hat{\mathcal{H}}(\boldsymbol{M_1})$

$$\hat{\mathcal{H}}(\boldsymbol{M_1}) = -2\,t_1 \begin{pmatrix} 0 & 0 & 1 \\ 0 & 0 & 0 \\ 1 & 0 & 0 \end{pmatrix} - 2\,t_2 \begin{pmatrix} 0 & 0 & -e^{i\phi} \\ 0 & 0 & 0 \\ -e^{-i\phi} & 0 & 0 \end{pmatrix}, \tag{3.13}$$

supporting the energy values, $\epsilon_{1,3} = \pm 2\sqrt{(t_1 - t_2 e^{-i\phi})(t_1 - t_2 e^{i\phi})}$ and $\epsilon_2 = 0$, where $\epsilon_1 \leq \epsilon_2 \leq \epsilon_3$. The corresponding eigenstates are denoted as $\Psi_{n,\mathbf{k}} = u_{\lambda,\mathbf{k}} c_{\mathbf{k}}$, where $u_{\lambda,\mathbf{k}}$ is a unitary transformation with $\lambda =$ A, B, C. Notably, the $\epsilon = 0$ case corresponds to the second band with eigenvector $\Psi_{2,\boldsymbol{M_1}} = (0\,1\,0)^T$, localized on the B sublattice.

Similarly, for the other two high-symmetry points $\boldsymbol{M_2}$ and $\boldsymbol{M_3}$, the eigenvalues of the corresponding Hamiltonian yield the eigenvalues $\epsilon_1 \leq \epsilon_2 = 0 \leq \epsilon_3$, where the $\epsilon = 0$ case again corresponds to the second band. Additionally, the eigenvectors corresponding to $\boldsymbol{M_2}$ and $\boldsymbol{M_3}$ can be obtained as $\Psi_{2,\boldsymbol{M_2}} = (0\,0\,1)^T$ and $\Psi_{2,\boldsymbol{M_3}} = (1\,0\,0)^T$, respectively. Owing to $\mathcal{C}_3$ rotation symmetry, the eigenvectors of the second band at $\boldsymbol{M_2}$ and $\boldsymbol{M_3}$, $\Psi_{2,\boldsymbol{M_2}} = (0\,0\,1)^T$ and $\Psi_{2,\boldsymbol{M_3}} = (1\,0\,0)^T$, are maximally localized on the C and A sublattices, respectively. Fig. 3.7 shows the strong sublattice localization at each of $\boldsymbol{M_i}$ on the second band.

SI plays an important role in constraining the interactions between electronic

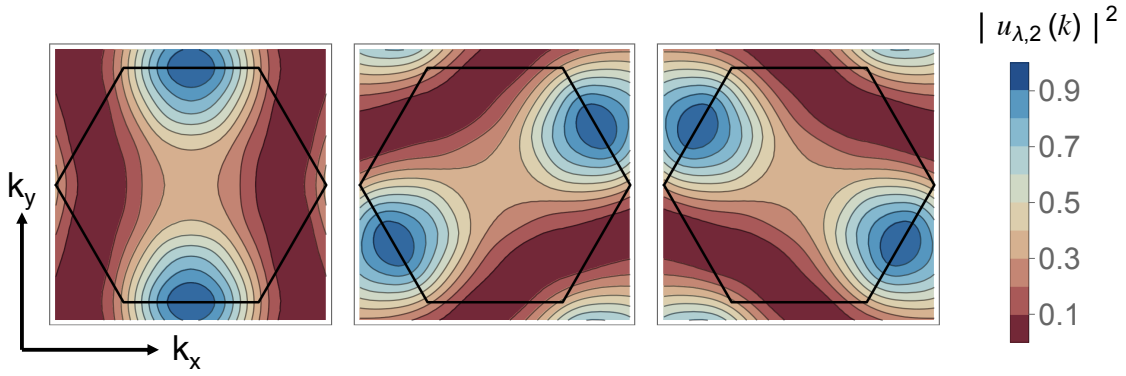

Figure 3.7: Contour plot of the sublattice weights for the second band corresponding to the sites A (left), B (middle), and C (right) of the kagome lattice at $(t_2\,\phi) = (0.258,\ \pi/2)$, demonstrating that each $\boldsymbol{M_i}$ point on band 2 corresponds to one of the three sites of the kagome lattice. In this example, the band carries a Chern number of $+2$ while supporting HOVHS at the $\boldsymbol{M}$ points. Here, the black lines denote the first Brillouin zone boundaries.

states located near $\boldsymbol{M_i}$ when the Fermi level crosses a Van Hove singularity. Earlier works have explored this regime for logarithmic VHS in kagome lattice [69, 112, 143]. The presence of the complex hopping on this kagome lattice, remarkably, uncovers a new regime where the second band supports HOVHS on the $\boldsymbol{M_i}$, displayed in the green contours of Fig. 3.4. Furthermore, these band support higher Chern numbers, $C = \pm 2, \pm 4$ (middle panel of Fig. 3.5), generalizing the SI in time-reversal broken Chern bands beyond the Chern number $C = \pm 1$ band on the honeycomb lattice [48]. The identification of topological bands showing SI and HOVHS is a promising platform to explore electronic correlations.

3.4 Discussion

Motivated by recent interest in band structures supporting higher-order Van Hove singularities, we have investigated a kagome system characterized by NN and NNN hopping, which, respectively, preserve and break time-reversal symmetry (Fig. 3.1). The latter, similarly, to a chiral hopping on the Haldane lattice, leads to

the formation of topological bands supporting Chern numbers $C = \pm 1, \pm 2, \pm 3, \pm 4$, as depicted in Fig. 3.5.

More notably, we have performed a comprehensive analytical and numerical analysis of the band dispersions near the six high-symmetry points $\boldsymbol{\Gamma}$, $\pm\boldsymbol{K}$ and $\boldsymbol{M_i}$ ($i = 1, 2, 3$), which uncovered a complex and diverse domain of HOVHS controlled by the magnitude and phase of the NNN hopping (Figs. 3.2, 3.3, and 3.4). As such, our analysis unveils Chern bands with strong power law divergence in the DOS, $\rho(\epsilon) \sim |\epsilon|^{-\nu}$ characterized by the exponents $\nu = 1/2, 1/3, 1/4$. Such strong singularities in the density of states can imprint characteristic features in the low-temperature intrinsic anomalous Hall response when the Fermi level crosses the HOVHS (Fig. 3.6).

We have explored distinct features of the kagome system worth mentioning. First, while it takes a critical value of the NNN hopping strength for HOVHS to emerge in bands 1 and 2, HOVHS can emerge at the $\pm\boldsymbol{K}$ and $\boldsymbol{M_i}$ out of the third (flat) band for infinitesimal strength of the NNN, as shown in Fig. 3.4. Furthermore, the NNN hopping provides a mechanism for the realization of high Chern number bands manifesting a sublattice interference whereupon electronic states of the second band are maximally localized on the A, B, and C sublattices as the momentum approaches $\boldsymbol{M_3}$, $\boldsymbol{M_1}$ and $\boldsymbol{M_2}$, respectively (Fig. 3.7).

The classification of HOVHS in kagome systems opens promising directions for future investigation. In particular, the interplay between band topology and large density of states provides a guiding principle to exploring correlation effects in kagome lattices, which could serve as a mechanism to realize unconventional electronic orders such as chiral topological superconductivity and fractional topological states.

Chapter 4

Quantum Fractality on the Surface of 3D Topological Insulators

Note: The material presented in this chapter has been published in *Physical Review B*, 108(15):155430, 2023. DOI: 10.1103/PhysRevB.108.155430

In this chapter, we explore the electronic states on the surface of 3D topological insulators outside the regime of Bloch theorem which is a key ingredient of our understanding of solid-state behavior. We investigate a new class of states arising from the coupling of surface Dirac fermions to a time-reversal symmetric fractal potential, which breaks translation symmetry while retaining self-similarity. This novel set of states, characterized by a fractal dimension, opens promising avenues for exploring exotic regimes of transport and quantum information storage in topological systems with fractal dimensionality.

Bloch's theorem dictates that single-particle electronic states in regular crystals are organized into electronic bands. Bloch states also encode invaluable topological information that underlies the classification of free fermion symmetry-protected topological states [156–158]. Deviations from perfect crystalline order are naturally present in any material, such as those produced by disorder and lattice defects.

However, Bloch electrons remain a useful framework to characterize the low energy properties of weakly correlated materials when these effects are small [159]. On the other hand, it is fundamental to inquire what types of novel electronic states could arise when regular crystalline order is strongly violated, breaking away from the traditional paradigm of Bloch states. Are there systematic ways to investigate electronic systems that lack translation invariance, but still retain some degree of structure beyond amorphous materials?

Fractals [78, 79] provide a rich arena to explore this front. They are geometric structures with intricate details at arbitrary scales that exhibit self-similarity across various scales while lacking translational invariance. Interestingly, even in the absence of translational symmetry, fractals can display self-similarity and point group symmetries. This makes them an excellent choice for investigating emerging self-similar quantum states that deviate from the well-established regime of Bloch states.

Fractality, which is prevalent across a wide range of complex natural phenomena and spans seemingly disparate domains, has also been studied in quantum systems. There is a long history of theoretical investigation of transport in fractal geometries, relating anomalous regimes of classical diffusion to the properties of the fractal [160–163], such as its fractal dimension. Furthermore, experimental developments in recent years have brought renewed interest in the phenomenon of quantum fractality in electronic systems. For instance, the assembly of Sierpiński gasket fractal networks on copper surfaces via deposition of CO molecules produces surface states with fractal dimension [80]. Quantum states with fractal dimensionality open a venue to explore phenomena outside the realm of integer dimensions, allowing for novel regimes of transport and correlations [164–176]. Moreover, they provide a rich setting to pursue new topological phenomena beyond topological Bloch states.

Motivated by these developments, we introduce and analyze a new fractal

system formed on the surface of 3D time-reversal invariant topological insulators (TIs) [49–51], in order to probe the response of surface Dirac fermions to a scalar potential with fractal geometry, which respects the two key symmetries of 3D TIs, namely time-reversal and charge conservation symmetries. Unlike Schrödinger electrons, Dirac fermions on the surface of topological insulators are characterized by anomalous properties such as spin-momentum locking and nontrivial Berry phase. In this work, we analyze the electrons on the TI surface subject to a time-reversal invariant scalar potential $V(\mathbf{r})$ that couples to electron density according to the $H_V = \sum_{\sigma=\uparrow,\downarrow} \int d\mathbf{r} V(\mathbf{r})\, \psi^\dagger_\sigma(\mathbf{r})\psi_\sigma(\mathbf{r})$, and which has a self-similar fractal structure, as depicted in Fig.4.1 for a Sierpiński carpet.

The fractal geometry could be imposed on the surface of $3D$ TI by atomic/molecular deposition techniques which have already been achieved on copper surfaces creating unconventional states such as molecular graphene [177] and electrons in a fractal Sierpiński geometry [80]. Nanopatterning [178–180] techniques that induce surface potential with fractal geometry could also open new pathways to design quantum states that combine topological and fractal properties. Another method to imprint fractal geometry on the surface of TI such as Bi_2Se_3 and Bi_2Te_3 involves surface etching techniques, where Se or Te atoms can be selectively removed in a controlled manner [181]. As we show in this work, emergent quantum fractality can be probed via scanning tunneling microscopy (STM) through distinct features in the LDOS.

The lack of translation invariance combined with the presence of anomalous Dirac fermions on the TI surface makes their theoretical study nontrivial even at the non-interacting regime, which is the focus of this work. To address this new regime, we perform large-scale exact diagonalization (ED) using finite element discretization. While lattice discretization leads to fermion doubling [182], we show in Sec.4.1 that the mixing between the extra copies of Dirac fermions is negligible

provided the fractal potential is smooth on the scale of the underlying lattice. This then provides a route to effectively model the response of a single Dirac cone on the TI surface to a fractal symmetry-preserving potential. Remarkably, our analysis uncovers Dirac quantum states that inherit the fractal dimension of the geometrical fractal deposited on the TI surface.

The focus of the present analysis of Dirac electrons in fractal potentials without translation invariance goes beyond the recent works exploring the interplay of the Dirac fermions on the surface of $3D$ TI with a periodic lattice potential. [30, 96] We also stress that this new regime is distinct from the well-explored multifractality studied in the context of localization transition in disordered electronic systems [183–194] where the disorder induces multifractal scaling in the surface state wavefunctions at the localization threshold. Although disordered systems can support multifractal states with a set of fractal dimensions, the possibility of Dirac surface states exhibiting fractal scaling behavior with a single scaling exponent corresponding to a fractal geometry of choice has not been previously discussed, to the best of our knowledge. This work's main result is establishing the existence of this new class of *Dirac Fractals* on TI surfaces. Additionally, our approach can be extended to 2D Dirac materials such as monolayer graphene and graphene-based heterostructures.

4.1 Sierpiński Carpet Geometry on 3D TI Surface

In this section, we introduce a model of the 3D TI surface imprinted with a Sierpiński carpet fractal geometry, as shown in Fig 4.1. The model consists of the surface Dirac cone of the 3D TI, described by a continuum Dirac Hamiltonian, coupled with a time-reversal symmetric scalar potential $V(\mathbf{r})$. The resulting Hamiltonian takes the

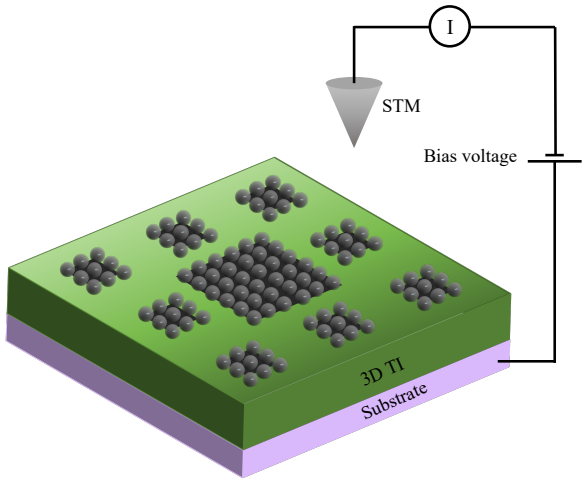

Figure 4.1: Schematic illustration of the experimental realization of the surface of a 3D TI coupled with a Sierpiński carpet fractal. The experimental setup consists (from top to bottom) of a thin film of $3D$ TI grown on a substrate, scattering centers deposited on the $3D$ TI surface that lead to surface electronic states with Sierpiński carpet fractal geometry, and STM apparatus to measure the LDOS of the surface states.

form

$$H = \hbar v_F \left(\boldsymbol{\sigma} \times \mathbf{p}\right) + V(\mathbf{r})\sigma_0 \,, \tag{4.1}$$

where v_F is the Fermi velocity, $\mathbf{p} = \left(p_x, p_y\right)$ is the 2D momentum, $\boldsymbol{\sigma} = \left(\sigma_x, \sigma_y\right)$ are the Pauli matrices, and σ_0 is the identity matrix. Here, the scalar potential $V(\mathbf{r})$, also called the fractal potential, consists of a network of potential wells of strength V arranged in a Sierpiński carpet fractal geometry, as depicted in Fig.4.2.

The construction of the Sierpiński carpet fractal starts with an $L_f \times L_f$ square region that can be considered at the zeroth generation Sierpiński carpet, denoted $G(0)$. The first generation carpet $G(1)$ is obtained by dividing $G(0)$ into nine square sub-regions of size $l_1 = L_f/3$, and removing the central square, as shown in Fig.4.2 (a). The second generation carpet $G(2)$ is then obtained by repeating the procedure on each of the remaining eight squares: each square is divided into nine squares of size $l_2 = L_f/3^2$, and the central square is removed. In general, the $G(n)$ generation

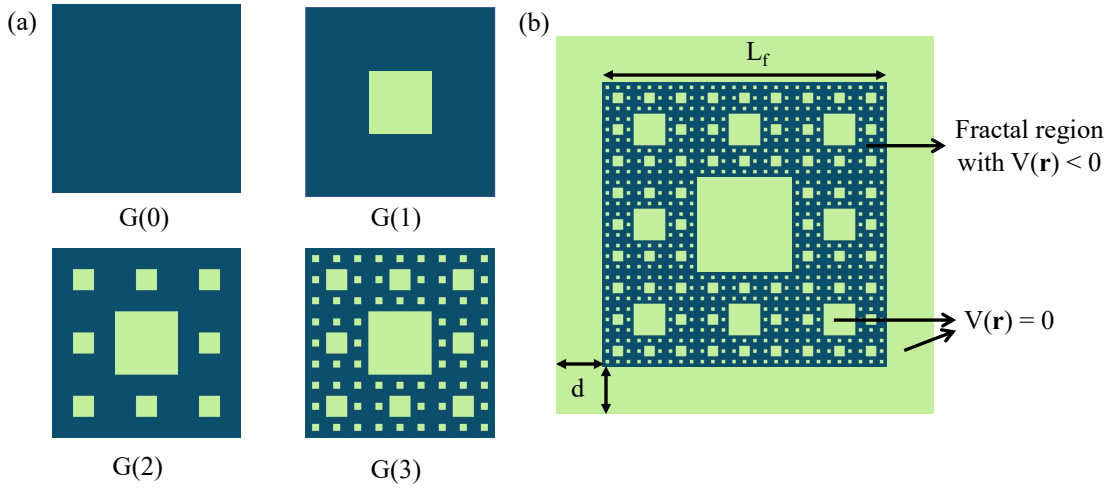

Figure 4.2: (a) Representation of the construction of the Sierpiński carpet fractal. $G(0)$ is a $2D$ square that can be subdivided into 9 square units of the same size, from which the central unit is removed to obtain the $G(1)$ unit of the Sierpiński carpet. The same procedure is then applied to the remaining 8 square units of $G(1)$ to generate $G(2)$. Similarly, $G(n)$ can be constructed from $G(0)$ by recursive application of this procedure. (b) Schematic of the model given in Eq. 4.1 that couples the surface Dirac cone of 3D TI with Sierpiński carpet fractal of fourth generation. Here, the region on the 3D TI surface, shown in a darker color, which is the intersection of all the fractal units of generations ranging from generations 1 to 4 is defined as the fractal region. It has a linear dimension L_f but has a Hausdorff dimension of 1.893. The fractal potential $V(\mathbf{r})$ takes a non-zero value V in the fractal region while zero otherwise. In this model, the fractal region is positioned away from the boundary of the 3D TI surface by a finite distance, $\frac{d}{a} = 3$

.

carpet is obtained from the $G(n-1)$ generation carpet by subdividing the l_{n-1}-sized squares from the previous step into nine squares of size $l_n = L_f/3^n$, and removing all the central squares. The Sierpiński carpet fractal is obtained recursively as the limit of the sequence of $G(n)$ as n tends to infinity. In practice we can only consider finite generation carpets as an approximation of the true fractal (up to $n = 4$ in our analysis), and take the potential $V(\mathbf{r})$ to have non-zero strength $V < 0$ only within the region $G(n)$, as shown in Fig 4.2 (b):

$$V(\mathbf{r}) = \begin{cases} V < 0 & \mathbf{r} \in G(n) \\ 0 & \text{otherwise} \end{cases} \tag{4.2}$$

and study the scaling properties of the system as n increases.

A defining characteristic of fractals is that they obey a scaling law characterized by a non-integer fractal dimension that remains constant over a range of length scales.[78] In the simplest cases, the fractal dimension can be found using a box-counting argument by considering the number N_n of boxes of linear size l_n needed to cover a region of total linear size L_f. A two-dimensional $L_f \times L_f$ square, for example, can be covered with $N_n = (L_f/l_n)^2$ such boxes, while a three-dimensional cube can be covered with $(L_f/l_n)^3$ boxes. In general, $N_n = (L_f/l_n)^D$ defines the Hausdorff dimension D of the set. Applying the box-counting method to the generation n Sierpiński carpet $G(n)$, since by construction $G(n)$ consists of $N_n = 8^n$ squares of width

$$l_n = \frac{L_f}{3^n}\,, \tag{4.3}$$

taking $N_n = \left(L_f/l_n\right)^D$ gives the Hausdorff dimension of the Sierpiński carpet fractal as $D = \ln 8/\ln 3 \approx 1.893$. We observe that for $G(n)$ with fixed finite n, the fractal scaling behavior will be seen for boxes of size $l_n < l < l_1$, and no scaling behavior will be seen below the length scale l_n.

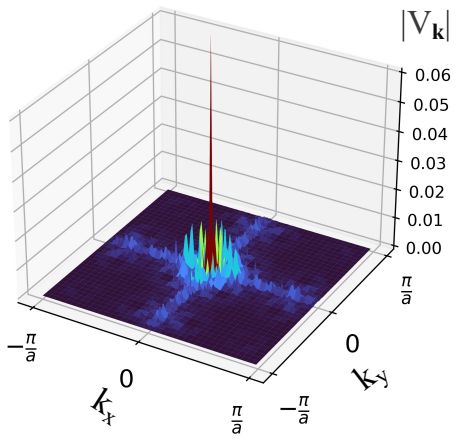

Figure 4.3: Fourier components ($V_{\mathbf{k}}$), in units of t, of the $G(4)$ fractal potential given in Eq. 4.2 with $V = -0.25\,t$, plotted in the first Brillouin zone of a $2D$ square lattice with lattice constant a. The dominating contribution comes from modes near zero momentum, with the largest red peak of height $V_{\mathbf{k}=0} = 0.14\,t$, shown in red. Note that the z-axis of the plot is cut off at $|V_{\mathbf{k}}| = 0.06\,t$ in order to display the details of the smaller peaks. The smallest length scale of $G(4)$ considered in this case is $l_4 = 3a$.

Since the fractal potential lacks translational invariance, a representation in terms of Bloch states is impossible. We, therefore, resort to an ED analysis of the single particle spectrum of the Hamiltonian Eq. (4.1), discretizing the Dirac model on a finite lattice that covers the fractal region. We chose a 249×249 square lattice with lattice constant $a = 1$, on which it is simpler to define the Sierpiński carpet fractal. The Dirac operator is discretized on this lattice using the finite difference method. With this choice we are constrained to look only at the first four generations of the Sierpiński carpet, lying within a square region of linear dimension $\frac{L_f}{a} = 243$ that we refer to as the fractal region below. Obtaining the full eigenspectrum of this model requires performing ED on an $N \times N$ lattice Hamiltonian matrix where $N = 2 \times 249^2 = 124002$ (the factor of 2 accounting for spin), the details of which are given in Appendix B. Furthermore, we work with boundary conditions that terminate the wavefunction at a distance $d \ll L_f$ away from the fractal region, as shown in Fig. 4.2.

In the absence of the fractal potential and with periodic boundary conditions, our choice of lattice regularization for the Dirac fermions leads to the periodic Bloch Hamiltonian

$$H_0 = t\left[\sin\left(k_y a\right)\sigma_x - \sin(k_x a)\sigma_y\right], \tag{4.4}$$

where $t = \frac{\hbar v_F}{a}$. This Hamiltonian supports four Dirac cones at momenta $\{(0,0),(0,\pi/a),(\pi/a,0),(\pi/a,\pi/a)\}$ in the Brillouin zone, each of which is described by Eq. (4.1) with $V = 0$. Since the regime of linearly dispersing Dirac fermions occurs in the energy domain $|E| \lesssim t$, we restrict the analysis of the effect of the fractal potential onto states within an effective bandwidth $W \sim 2t$. Furthermore, we require that $W/V \lesssim 1$, so that the fractal potential does not exceed the energy scale of the 3D TI bulk energy gap.

The appearance of an even number of Dirac cones in the lattice Hamiltonian H_0 is a familiar manifestation of fermion doubling.[182] In order to capture the

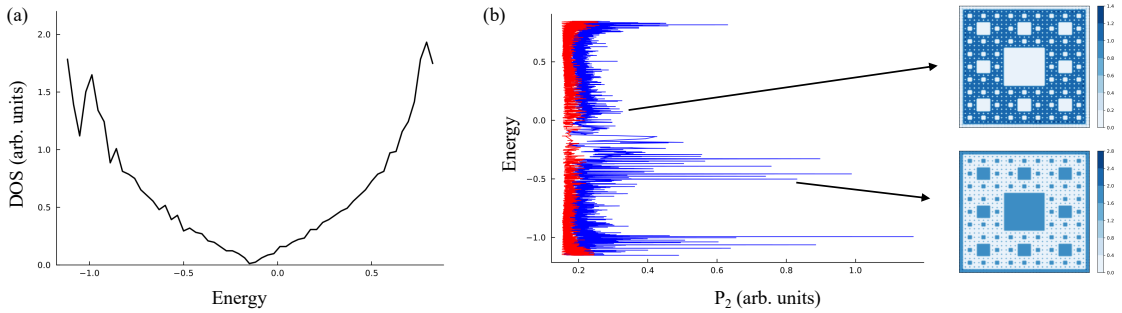

Figure 4.4: (a) DOS plotted vs energy, measured in units of $t = \frac{\hbar v_f}{a}$, for a $G(4)$ fractal potential of strength $V = -0.25\,t$. The DOS vanishes at $E_D = -0.14\,t$, and the considered energy window is centered around $E = E_D$ with a width of $W = 2t$. (b) The $q = 2$ moment of IPR (P_2) of each individual state, as given by Eq. (4.5), plotted against energy, measured in units of $t = \frac{\hbar v_f}{a}$, for $G(4)$ fractal potential of strengths $V = -0.25\,t$ (blue) and $V = 0$ (red). The LDOS maps of the states corresponding to $V = -0.25\,t$, that lie within an energy window of width $\Delta E = 0.01\,t$, around $E = 0.1\,t > E_D$ and $E = -0.53\,t < E_D$, as indicated by the arrows, are shown on the right.

properties of the TI surface described by a single component Dirac fermion, we restrict the fractal potential to have negligible Fourier components with $|\mathbf{k}| \gg \frac{1}{a}$, which ensures that the coupling between different Dirac cones is negligible.

We verified this condition for fractal potentials smooth on the scale of the discrete lattice i.e, $l_n \gg a$, as depicted in Fig. 4.3 that shows that the dominant Fourier components of the fractal potential are peaked at small momenta $|\mathbf{k}| \ll \frac{1}{a}$. In addition, the inversion symmetry of the Sierpiński carpet forces the Fourier components with momenta $\mathbf{k} \in \{(0, \pi/a), (\pi/a, 0), (\pi/a, \pi/a)\}$ to vanish, thus further suppressing the coupling between different Dirac cones.

4.2 Numerical Analysis of the Model

In this section, we discuss the results of the ED analysis of the model given in Eq. (4.1) and investigate the emergence of the Dirac surface states with fractal dimensionality in the presence of the potential $V(\mathbf{r})$. We identify the dimensions of the

states using two complementary approaches. In Sec. 4.2.1 the fractal scaling behavior of the surface states is numerically established by analyzing the distribution of the IPR of the single-particle states, and in Sec. 4.2.2 we confirm these results using the standard box-counting applied to the local density of states. In both approaches, we numerically observe the occurrence of states with fractal dimension ≈ 1.89.

As we are regularizing the single Dirac cone using a square lattice with lattice constant a and hopping parameter t, the interplay between the fractal potential and kinetic effects is captured by the dimensionless parameter V/t. The ED analysis [195] of the model is performed with a fractal potential of strength $V/t = -0.25$, which corresponds to 12.5% of the effective bandwidth W, for each of the first four generations of the Sierpiński carpet, and the obtained eigenspectra are studied to seek out the onset of fractality in the Dirac surface states.

The large-scale diagonalization yields information about the single-particle eigenstates formed in the fractal region over a wide range of energies. With this dense data, we perform several lines of inquiry, starting with the analysis of the density of states (DOS). We observe that the DOS corresponding to a $G(4)$ fractal potential shown in Fig 4.4 (a), vanishes at non-zero energy $E_D \approx -0.14t$. This implies that the fractal potential shifts the massless Dirac cone in energy to $E_D = V_{\mathbf{k}=0}$ while leaving the time-reversal symmetry (TRS) intact, so that the spectrum is formed by degenerate Kramers pairs. We numerically confirm that the shift in energy E_D is directly proportional to V such that the Dirac point moves down (up) in energy as V grows more negative (positive). Additionally, we note that the particle-hole symmetry of the DOS about E_D is broken when the potential is introduced.

To probe the localization properties of eigenstates $\psi(\mathbf{r})$, we employ the inverse participation ratio, [196] $IPR_q = \sum_i |\psi(\mathbf{r}_i)|^{2q}$ where i is summed over all the lattice points of the system and $q \in \mathbb{R}$. A uniform state has an $IPR_2 = 1/N$ where N is

the total number of sites, and in general $1/IPR_2$ can be considered as an effective number of sites N_f to which the wave function is localized. For a state with an effective fractal dimension, we expect the same scaling for N_f as for the number of boxes needed to cover the fractal, i.e. $N_f \sim (L_f/l)^D$ where l is the lattice constant. However, as discussed in Sec. 4.1, for a finite generation approximation of the fractal $G(n)$ the fractal scaling persists only for boxes of size l_n and above. To take this into account, we consider a coarse-grained IPR obtained by averaging the wave function over the length scale l_n, dividing the L_f sized square region shown in Fig. 4.2(a) into l_n-sized regions $\mathcal{A}_i$, each of which is treated as a coarse-grained lattice site. The coarse-grained probability distribution is then defined as $|\bar{\psi}_i|^2 = \sum_{j\in\mathcal{A}_i} |\psi(\mathbf{r}_j)|^2$ and the corresponding coarse-grained IPR is given by

$$P_q = \sum_i |\bar{\psi}_i|^{2q} \tag{4.5}$$

where the index i runs over all the the l_n-sized regions denoted by $\mathcal{A}_i$. Wave function normalization ensures $P_{q=1} = 1$, and henceforth we focus on $q > 1$ modes.

In Fig. 4.4(b), we display the second moment of the IPR (P_2) numerically calculated for each of the eigenstates corresponding to the $G(4)$ fractal potential. The spectrum consists of Kramers pairs of localized states characterized by high IPR peaks in an energy window of width $W = 2t$ around E_D. A striking feature is the appearance of two classes of states separated by the scale E_D. The manifold of states with $E > E_D$ exhibits a characteristic LDOS distribution consistent with the fractal, as shown in the top right LDOS map of Fig. 4.4 (b), where the probability of finding electrons outside the fractal region, though non-zero, is very small. Importantly, not all the individual eigenstates belonging to this class of states above E_D exhibit this characteristic LDOS distribution with very small support from outside the fractal region. As the wide range of heights shown by their corresponding IPR peaks in

Fig. 4.4 (b) indicates, the individual eigenstates have different IPR values, thereby different spatial distributions of the LDOS. But interestingly, when we consider the LDOS map averaged over in energy that corresponds to the states in an energy window of width $\Delta E \sim 10^{-2}\, t$, we find the emergence of the characteristic LDOS profile shown in the top right LDOS map of Fig. 4.4 (b), that mirrors features of the Sierpiński carpet fractal. This suggests that most of the individual eigenstates above E_D, in an energy window of width ΔE feature the geometry of the Sierpiński carpet, as we confirm below.

The states with $E < E_D$, on the other hand, show more pronounced IPR peaks, with spatial profile shown by the bottom right LDOS map of Fig. 4.4 (b). These correspond to electronic configurations with probability dominated by contributions outside the fractal region. Such high IPR peaks can be attributed to the fact that the area outside the fractal region is smaller than the area of the fractal region when approximated by finite generation sets $G(n)$ for $n \leq 4$; for sufficiently large n we, therefore, expect the IPR of states with $E > E_D$ to eventually exceed that of states with $E < E_D$. Already at $n \leq 4$, we observe additional lower IPR peaks for $E < E_D$, that correspond to more delocalized states that have a substantial weight in the fractal region in comparison to the states with higher IPR peaks. In all cases, the states with $E < E_D$ lack self-similarity, indicating the absence of fractal scaling behavior. Importantly, we have observed the same pattern described above for all four fractal generations of the Sierpiński carpet fractal potential that we studied.

While the LDOS maps provide important visual guidance of the onset of Dirac states with fractal dimension, we confirm that the states with energy $E > E_D$ indeed inherit the scaling properties of the Sierpiński carpet fractal by calculating their fractal dimensions through IPR scaling in Sec.4.2.1, and box-counting methods in Sec.4.2.2.

4.2.1 Scaling of the IPR logarithm

In this section, we provide numerical evidence that states with energy $E > E_D$ have a fractal dimension, using the scaling of the coarse-grained IPR distribution. As alluded to above, the inverse of the second moment IPR $P_2 \sim 1/N_f$ can be considered as the effective number of coarse-grained sites occupied by the eigenstate. If the eigenstate is completely uniform within the fractal region and vanishes outside of it, the IPR coarse-grained over boxes of size l_n would then be given by precisely $1/N_n$ with N_n being equal to the number of boxes of size l_n needed to cover the fractal region. In that case, we, therefore, conclude that $P_2 = (L_f/l_n)^{-D}$ where D is the fractal dimension of the Sierpiński carpet obtained using the box-counting method, and which can therefore alternatively be obtained by scaling P_2 with the generation n.

In general, the wave functions are non-uniform and non-vanishing, but since P_q remains well-defined we can obtain an effective dimension of the wave functions by considering how P_q scales with the generation of the fractal. If the wave functions in a given energy window are scale-invariant on a range of length scales l with $a \ll l \ll L_f$, the IPR *distribution* $\mathcal{P}$ over a set of states has a universal form independent of system size and box size l_n.[196–198] More precisely, the distribution $\mathcal{P}\left[\ln\left(P_q/P_q^{typ}\right)\right]$ of the IPR logarithms scaled by a typical IPR P_q^{typ} (which can be taken to be the mean of the IPR distribution) is independent of L_f and l_n. The scaling properties of the IPR are contained in P_q^{typ}, which in this case satisfies

$$P_q^{typ} \propto \left(\frac{L_f}{l_n}\right)^{-D_q(q-1)}, \tag{4.6}$$

where D_q is the fractal dimension that can be different for different q, which signals multifractality.[199, 200] If $D_q = D$ for all q, the system is fractal and there is no multifractality.

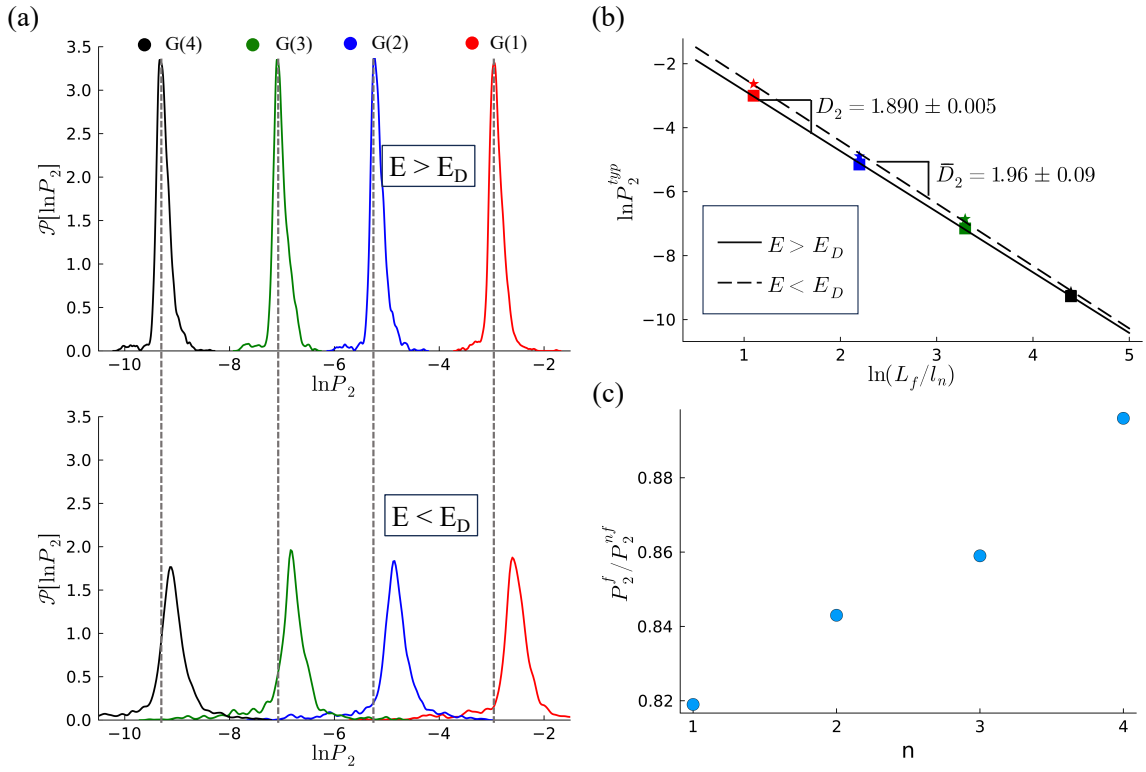

Figure 4.5: (a) Distribution of the IPR logarithm, $\mathcal{P}[\ln P_2]$ of the two classes of states separated by E_D, for each of the first four generations of the Sierpiński carpet fractal potential of strength $V = -0.25\,t$. The dashed line indicates the mean $\ln P_2^{typ}$ of $\mathcal{P}[\ln P_2]$ corresponding to $E > E_D$ for each of the first four fractal generations. (b) The log-log scaling of the typical values $\ln P_2^{typ}$ shown in (a), with linear dimension $L_f/l_n = 3^n$. The fractal dimensions, D_2 and $\bar{D}_2$ of the set of states with $E > E_D$ and $E < E_D$ respectively, are given by the corresponding regression slopes. (c) Ratio of the typical IPR values (P^{typ}) corresponding to $E > E_D$ and $E < E_D$, denoted as P_2^f and P_2^{nf} respectively, plotted as a function of the fractal generation n.

To test if this scaling scenario holds for states with $E > E_D$, as suggested by the characteristic LDOS maps shown in Fig. 4.4(b), we plot the $\ln P_2$ distribution for the states with $E > E_D$ for the first four generations of the fractal potential, as displayed at the top of Fig. 4.5(a). We note that each of the distributions displays a sharp peak and narrow width, indicating that most of the states above E_D have similar spatial support. Moreover, the distributions appear similar for all the fractal generations, and we confirm that they largely coincide upon shifting along the horizontal axis. The same behavior is also exhibited by $\mathcal{P}[\ln P_3]$.

In Fig. 4.5(b) we show the scaling of the corresponding typical values $P_2^{typ}(n)$ (given by the mean value of the distribution) with the linear dimension L_f/l_n, and extract the fractal dimension D_q from the scaling exponent according to Eq.(4.6). [198, 201–203] From the regression slopes, we determine that the states with $E > E_D$ have fractal dimension $D_2 = 1.890 \pm 0.005$, which is very close to the dimension of the Sierpiński carpet. We also check for possible multifractal behavior[199] by calculating the $q = 3$ as well as $q = 1.5$ scaling exponents, which gives the corresponding fractal dimensions, $D_3 = 1.86 \pm 0.04$ and $D_{1.5} = 1.895 \pm 0.008$, as shown in Appendix C. We are unable to check the scaling behavior for $q > 3$ due to system size limitations. However, since the fractal dimension of the Sierpiński carpet falls within the confidence interval of the estimated value of D_2, $D_{1.5}$ and D_3, our findings strongly suggest that for $E > E_D$, the states on the surface of the 3D time-reversal invariant topological insulator are well localized in the fractal, thus inheriting the fractal dimension of the Sierpiński carpet.

We similarly carry out the same IPR scaling analysis for states with $E < E_D$. The corresponding $\ln P_2$ distributions for the first four generations of the fractal potential are plotted in Fig. 4.5(a). In this case, we do not expect a scaling behavior for low generations if the wave functions are localized to the non-fractal region, because the box-counting dimension of the non-fractal region converges to two only

for sufficiently large generations $n \gg 4$, as can be verified by direct computation. Surprisingly, we nevertheless find that the scaling of the typical IPR values, again given by the mean of the distribution, with L_f/l_n results in a scaling dimension $\bar{D}_2 = 1.96 \pm 0.09$, as shown in Fig. 4.5(b). This suggests that the typical wave functions for states with $E < E_D$ are close to two dimensional already for small generations, despite the presence of states with high IPR peaks located on the tails of the distributions shown at the bottom of Fig. 4.5 (a) which appear to be localized to the non-fractal region. This suggests that these typical states have wave functions that leak considerably into the fractal region. This additionally implies that although the IPR of the fractal states with $E > E_D$ is on average lower than that of the non-fractal states with $E < E_D$, as the generation increases the IPR of the fractal states will eventually exceed that of the non-fractal states. This trend can be seen by comparing peaks of the IPR distribution for fractal and non-fractal states, as shown by vertical dashed lines in Fig. 4.5(a): the non-fractal distribution can be seen to shift to the left (towards lower IPR) faster than the fractal distributions as the generation increases. This trend is explicitly verified in Fig. 4.5(c).

We also observe that the IPR distributions for states with $E < E_D$ are broader than for states with $E > E_D$, which reflects the wider range of IPR peaks for $E < E_D$ shown in Fig. 4.4(b). The states localized to the non-fractal region corresponding to the highest IPR peaks, which we do not expect to exhibit two-dimensional scaling at low generations, lie in the higher tail ends of the IPR distributions, so these are not typical states. For high generations $n \gg 4$, we expect the dimension of these atypical states to tend to two and their IPR to decrease as the ratio of the area outside to the area inside the fractal grows with n.

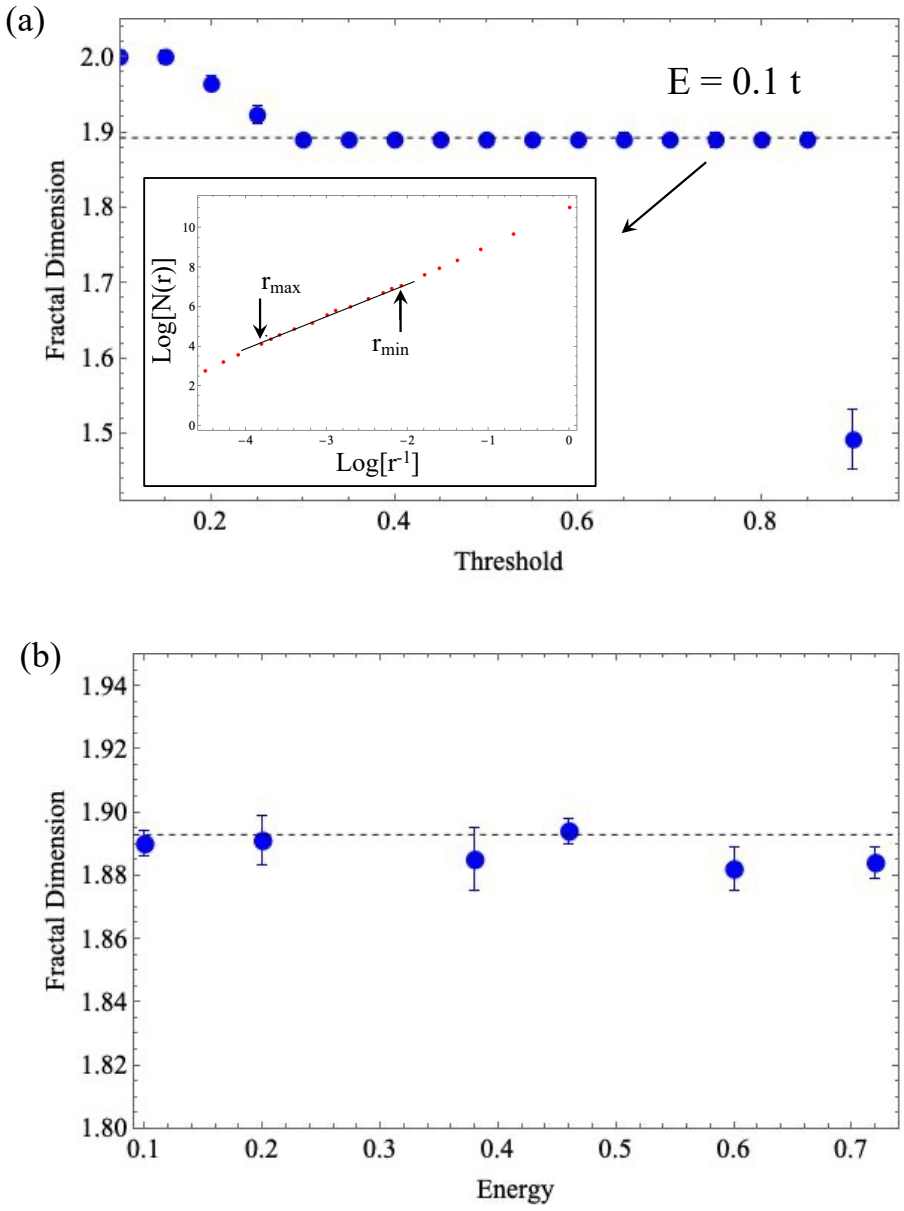

Figure 4.6: (a) Fractal dimension D of the states within an energy window of width $\Delta E = 0.01t$ around $E = 0.1\,t$, for a $G(4)$ fractal potential of strength $V = -0.25\,t$, calculated using the box-counting method, plotted against the binarization threshold, α. The plateau at $D = 1.890 \pm 0.004$ indicates the fractal dimension for threshold values ranging from 0.3 to 0.85. Note that the error bars of the plot are smaller in size compared to the scale of the y-axis. Inset shows the log-log plot of $N(r)$ vs $1/r$ corresponding to the threshold $\alpha = 0.75$. Here, r_{min} and r_{max}, respectively, denote the minimum and maximum box sizes chosen to estimate the box-counting dimension of the states. (b) Fractal dimensions of the states as a function of the corresponding energy values for a $G(4)$ Sierpiński carpet fractal potential of strength $V = -0.25\,t$, calculated using the box-counting method, as shown in (a). The black dashed line in (a) and (b) marks the fractal dimension of the Sierpiński carpet at $D = 1.893$.

4.2.2 Box-counting method

In this section, we provide an alternative confirmation of the fractal dimension of states with energy $E > E_D$ using the box-counting method applied to the LDOS. The method is based on counting the number $N(r)$ of boxes of size r that cover the LDOS profile of the wavefunction, leading to the Minkowski-Bouligand (or the box-counting) dimension[204]

$$D = \lim_{r \to 0} \frac{\ln(N(r))}{\ln(1/r)} \,. \tag{4.7}$$

To binarize the LDOS map we introduce a threshold $\alpha > 0$, such that values of LDOS below (above) α are set to zero (one) in the binarized map. Varying α allows us to probe whether the fractal dimension obtained via Eq. (4.7) is stable over a range of threshold values. A threshold that is too low or too high makes the binarized map sensitive to very short distance features of the LDOS, for instance, due to the lattice discretization. Additionally, the scaling given by Eq. (4.7) holds[205, 206] only in a finite range of box sizes $r \in [r_{min}, r_{max}]$, as it breaks down when box sizes are either too close to the linear dimension of the system (this tends to overestimate the dimension), or too small and pick up spurious short distance behavior due to noise. Following Ref. [206], we determine this finite range as follows. We start with all the possible box sizes r. As we reduce r from the maximum possible box size, we obtain a regression slope of two until r reaches r_{max}. Then r_{min} is determined as the smallest box size that gives a linear regression (with a maximum standard deviation of 10^{-3}) in the range $r \in [r_{min}, r_{max}]$.

In Fig. 4.6(a), we show the Minkowski-Bouligand dimension for an energy window of width $\Delta E = 0.01\,t$ around $E = 0.1\,t > E_D$ for a $G(4)$ fractal potential $V = -0.25\,t$, and for different values of the binarization threshold ranging from 0 to 1, where the LDOS values are rescaled such that their minimum and maximum

values are 0 and 1 respectively. When the threshold α is set close to zero such that we pick up contributions from even the shorter LDOS peaks, the LDOS landscape appears homogeneous, thereby resulting in a box-counting dimension of *two*. On increasing α further, interestingly, we find a range of threshold $\alpha \in [0.3, 0.85]$ that shows the emergence of a set of dominant LDOS peaks spread across the fractal region, as indicated by the plateau at $D = 1.890 \pm 0.004$, which characterizes the onset of fractal dimensionality in good approximation with that of the Sierpiński carpet fractal. Importantly, our approach reveals the stability of the fractal scaling behavior over a considerable range of threshold values.

Moreover, the box-counting method applied to a larger set of states with $E > E_D$ reveals, as shown in Fig. 4.6(b), reveals that their fractal dimension is in good agreement with the fractal dimension of the Sierpiński carpet. Therefore, combined with the analysis of the IPR scaling discussed in Sec. 4.2.1, the fractal dimension of the TI surface state obtained for the Minkowski-Bouligand dimension provide strong evidence that the Dirac surface states can inherit the scaling properties of the Sierpiński carpet fractal. Furthermore, we have observed similar fractal dimensions for another value of the fractal potential with $V = -0.5t$, suggesting that the observed fractal character of the states is robust against varying the strength of the fractal potential.

4.3 Beyond the Sierpiński Carpet Geometry

We numerically establish that coupling a single Dirac fermion on the surface of a 3D TI with fractal geometry allows the Dirac surface states to inherit the scaling properties of the corresponding fractal geometry, using the example of fractal potential carrying the geometry of the Sierpiński carpet fractal. Furthermore, we confirm these results by coupling the 3D TI surface with a different fractal geometry,

the Sierpiński gasket. Sierpiński gasket is a fractal with the overall shape of an equilateral triangle, recursively subdivided into smaller equilateral triangles, with its scaling behavior defined by a single scaling exponent, $\log 3/\log 2 \approx 1.585$. Our analysis, as detailed in Appendix D, confirms that the Dirac surface states can indeed inherit the scaling properties of the Sierpiński gasket when the 3D TI surface is coupled with this fractal geometry.

4.4 Discussion and Outlook

Time reversal invariant 3D topological insulators are a large class of symmetry-protected topological states with surface Dirac fermions protected by time-reversal and charge conservation symmetries, which provide a rich arena to explore exotic regimes of quantum matter. In this work, we used large-scale exact diagonalization to study a new class of Dirac surface states formed when a symmetry preserving one-body potential with the geometry of a fractal is superimposed on the surface of this topological material, opening a new direction to interrogate and explore topological fermionic states with fractal properties.

The main finding of this study is the onset of Dirac fractals, gapless Dirac states whose wave function acquires the fractal dimension of the applied potential over a wide range of energies. These results were obtained for a symmetry-preserving one-body fractal potential having the geometry of a Sierpiński carpet fractal. We have employed two methods based on inverse participation ratio as well as box counting, which show within numerical accuracy that Dirac fermions on the TI surface acquire the fractal dimension of Sierpiński carpet fractal $D \approx 1.89$. Additionally, we confirmed these results for another example where the Dirac surface states, coupled with the Sierpiński gasket geometry acquire the fractal dimension of the Sierpiński gasket fractal $D \approx 1.58$. Furthermore, our analysis does not support the scenario of

multifractality. Therefore, to our knowledge, this work presents the first numerical evidence of time-reversal invariant Dirac surface states of fractal character, which expands the realm of fractal quantum states beyond time-reversal broken fractal Hofstadter states. [21, 119, 207]

This research opens an interesting avenue to search for exotic fractal quantum orders on the surface of topological insulators. A fruitful direction would be to characterize new regimes of charge and energy transport in such fractal networks for the Sierpiński carpet and beyond. Moreover, probing the response of such states perturbations that break time-reversal and/or charge conservation symmetry symmetries could offer new ways to understand fractionalization phenomena in the fractal setting. Another direction would be to understand the formation of fractal states in Weyl semimetals and, in this context, to understand the role of weak disorder on surface states. [208, 209] The advent of new experimental platforms that could induce a surface potential with fractal geometry using techniques such as nanopatterning [178–180], and molecular deposition [80, 177], combined with probe techniques such as scanning tunneling microscopy, offer promising experimental landscapes to realize and probe Dirac fractals.

Chapter 5

Conclusion and Outlook

The fundamental properties of condensed matter systems are intimately tied to the intricate interplay between electrons and the underlying atomic structure. The potential energy landscape created by this atomic arrangement significantly influences the electronic behavior, giving rise to a diverse range of quantum phenomena. Building on this foundation, this thesis has pursued two distinct research pathways aimed at exploring unconventional quantum states within these complex electronic landscapes.

The first avenue investigates electron behavior within a translational invariant potential energy landscape, specifically examining the combined effects of higher-order Van Hove singularities (HOVHS) and broken time-reversal symmetry (TRS). This study is applied to two notable systems: the surface of a 3D topological insulator (TI) and a kagome lattice, each providing a rich platform for exploring the role of HOVHS in topologically nontrivial phases.

On the surface of a 3D topological insulator (TI), we have identified a mechanism to create time-reversal-breaking Chern bands that host higher-order Van Hove singularities (HOVHS). Specifically, we demonstrate that these HOVHS in topologically nontrivial bands emerge from the combined effects of a time-reversal-

breaking Zeeman field—induced by proximity to a ferromagnetic insulator—and a time-reversal-invariant moiré potential applied to the surface electrons of a 3D TI. Through exact diagonalization and symmetry analysis, we show that tuning the relative strengths of the Zeeman field and moiré potential energy scales leads to a range of higher-order Lifshitz transitions at the moiré Brillouin zone valleys.

The classification of HOVHS in moiré Chern bands on the surface of 3D TIs provides a rich avenue for investigating correlation effects linked to strong density of state singularities. These investigations could uncover unconventional electronic orders, such as chiral topological superconductivity and fractional topological states. Additionally, extending our analysis of HOVHS from the surface of 3D TIs to 2D materials with multiple Dirac fermion flavors—such as twisted bilayer graphene [7, 115, 116] and transition metal dichalcogenides [117, 118]—would be particularly promising.

Additionally, we identify a characteristic signature in the intrinsic anomalous Hall response as the Fermi level traverses a Lifshitz transition. Specifically, the rate of change of the intrinsic anomalous Hall conductivity, $d\sigma_{xy}^{\text{int}}/d\mu$, exhibits a pronounced low-temperature peak due to the high density of states near the VHS, reflecting the logarithmic or power-law divergences of conventional and higher-order Lifshitz transitions. This relationship offers a pathway to experimentally probe VHS and Chern bands through transport measurements, with potential applications extending beyond HOVHS on topological insulator surfaces to a broader range of Hofstadter-Chern bands [87, 119–132] and zero-field Chern bands in moiré heterostructures [133–137].

We have also investigated the interplay of HOVHS and broken TRS on the kagome system, a geometrically frustrated lattice known for its potential to host exotic quantum phases. By introducing time-reversal-breaking next-nearest-neighbor(NNN) hopping, we obtained non-trivial topological band structures characterized by

higher Chern numbers. This intricate interplay between geometry and topology uncovered a rich landscape of HOVHS in the electronic band structure. These HOVHS, characterized by strong power-law divergences in the density of states, could potentially lead to the emergence of unconventional quantum phases such as unconventional superconductivity and fractional quantum Hall states. Furthermore, the NNN hopping induced topological bands with higher Chern numbers obeying a sublattice interference, where electronic states in specific bands became maximally localized on particular sublattices at high-symmetry points in the Brillouin zone.

Building on our investigation of HOVHS and broken TRS in kagome systems, future research could take several exciting directions. The classification of HOVHS in kagome systems paves the way for further exploration of the interplay between band topology and high density of states. This interplay provides a guiding principle to examine correlation effects in kagome lattices. Additionally, the recent discovery of new kagome metals, such as AV_3Sb_5 (A = K, Rb, Cs), which display a variety of exotic correlated electronic phenomena, [69–75] further motivates the study of HOVHS in these systems. Moreover, exploring spinful versions of this model, particularly in kagome metals like FeGe[210–212], could lead to a richer classification and a deeper understanding of the topological phases in kagome systems.

The next part of the thesis introduced fractal geometries as a departure from translational symmetry, focusing on the unique electronic properties they can induce. We investigated the coupling of Dirac fermions on the surface of 3D topological insulators with fractal potentials, leading to the emergence of Dirac fractals, a novel class of topological states characterized by fractal dimensions. These results were obtained for symmetry-preserving one-body fractal potentials having the geometry of Sierpiński carpet and Sierpiński gasket fractals. We have employed two methods based on inverse participation ratio as well as box counting, which

show within numerical accuracy that Dirac fermions on the TI surface acquire the fractal dimension of the corresponding fractal geometry of choice. Moreover, our analysis finds no evidence for multifractality, making this, to our knowledge, the first numerical demonstration of time-reversal invariant Dirac surface states with fractal characteristics.

This research opens a new avenue to explore exotic quantum orders on the surface of topological insulators. A particularly interesting direction is the characterization of charge and energy transport within fractal networks, which may be governed by their intrinsic fractality,[164, 176, 213] particularly for geometries extending beyond the Sierpínski carpet. Leveraging the fractal nature of these networks, our model offers a platform to study quantum transport in non-integer dimensions within the framework of Dirac surface states.

The level statistics of fractal systems, strongly influenced by fractal dimensions and geometric properties,[214] offer a unique opportunity to identify distinctive fingerprints of Dirac fractal states through their distribution. Additionally, our model provides an opportunity to investigate transport phenomena using renormalization group methods, [215–217] leveraging the unique topological properties of Dirac surface states—an area yet to be fully explored. Furthermore, examining the response of these states to perturbations that break time-reversal symmetry and/or charge conservation could yield new insights into fractionalization phenomena in fractal systems.

Appendix A

Analytical Expressions of the HOVHS lines

On the line $\phi = \pi$ in the t_2-ϕ parameter space, bands 2 and 3 are touching at $\mathbf{\Gamma}$ point, and thus need the degenerate perturbation theory (PT) treatment. We can set up the matrix

$$V = \begin{pmatrix} V_{22} & V_{23} \\ V_{23}^* & V_{33} \end{pmatrix}, \tag{A.1}$$

where $V_{ij} = \Psi_{i,\mathbf{\Gamma}}^{(0)*} \hat{\mathcal{H}}(\boldsymbol{p}) \Psi_{j,\mathbf{\Gamma}}^{(0)}$. After diagonalization, we use the two eigenvalues, $3t_2/4$ and $-1/4$, in replacement of $\Psi_{n,\mathbf{\Gamma}}^{(0)*} \hat{\mathcal{H}}(\boldsymbol{p}) \Psi_{n,\mathbf{\Gamma}}^{(0)}$ for the energy shift in Eq. (3.9).

Given that the perturbation matrices for $\boldsymbol{M}$ and $\boldsymbol{K}$ have both linear and quadratic dependence on $\boldsymbol{p}$, we use second-order perturbation theory, with the energy shift defined as the following:

$$\epsilon_{n,\boldsymbol{k}+\boldsymbol{p}} - \epsilon_{n,\boldsymbol{k}}^{(0)} = \hat{\mathcal{H}}_{nn}(\boldsymbol{p}) + \sum_{m \neq n} \frac{|\hat{\mathcal{H}}_{nm}(\boldsymbol{p})|^2}{\epsilon_{n,\boldsymbol{k}}^{(0)} - \epsilon_{m,\boldsymbol{k}}^{(0)}}, \tag{A.2}$$

where $\boldsymbol{k}$ can be $\boldsymbol{K}$ or $\boldsymbol{M}$, and $\hat{\mathcal{H}}_{nm} \equiv \Psi_{n,\boldsymbol{k}}^{(0)*} \hat{\mathcal{H}}(\boldsymbol{p}) \Psi_{m,\boldsymbol{k}}^{(0)}$. With Eq. A.2, we derived the expressions for Hessian at $\boldsymbol{M}$ and $\pm\boldsymbol{K}$ points:

$$\begin{aligned}\mathbb{H}_{1,\boldsymbol{M}}(t_2,\phi) = \frac{1}{64\gamma^6}[3(\gamma - 9t_2^4 - 9\gamma t_2^3\cos(3\phi) + (15\gamma - 4)t_2^2\cos(2\phi) \\ + t_2(-7\gamma + 22t_2^2 + 2)\cos(\phi) - 12t_2^2 + 1)] \\ [-\gamma + t_2^4 + t_2(-\gamma - 6t_2^2 - 2 + \gamma t_2(t_2\cos(3\phi) + \cos(2\phi)) + 8t_2\cos^2(\phi)) - 1]\end{aligned} \tag{A.3}$$

$$\begin{aligned}\mathbb{H}_{2,\boldsymbol{M}}(t_2,\phi) = \frac{1}{16\gamma^4}\left[9t_2^3\cos(3\phi) - 15t_2^2\cos(2\phi) + 7t_2\cos(\phi) - 1\right] \\ \left[-3t_2^2(t_2\cos(3\phi) + \cos(2\phi)) + 3t_2\cos(\phi) + 3\right]\end{aligned} \tag{A.4}$$

$$\begin{aligned}\mathbb{H}_{3,\boldsymbol{M}}(t_2,\phi) = \frac{1}{64\gamma^6}[9t_2^4 + \gamma(1 - 9t_2^3\cos(3\phi)) + (15\gamma + 4)t_2^2\cos(2\phi) \\ - t_2(7\gamma + 22t_2^2 + 2)\cos(\phi) + 12t_2^2 - 1][3t_2(-\gamma + 6t_2^2 + 2)\cos(\phi) + \gamma t_2(t_2\cos(3\phi) \\ + \cos(2\phi)) - 8t_2\cos^2(\phi) - 3(\gamma + t_2^4 - 1)]\end{aligned} \tag{A.5}$$

$$\begin{aligned}\mathbb{H}_{1,\pm\boldsymbol{K}}(t_2,\phi) = \frac{\csc(\phi)}{16t_2\left(-6t_2\cot(\phi) + 2\sqrt{3}t_2 + 3\csc(\phi)\right)}[36t_2^3 - 24t_2^2\cos(\phi) \\ + \sqrt{3}\left(4t_2^2\sin(\phi)(5 - 12t_2\cos(\phi)) + 6t_2\cot(\phi) - 3\csc(\phi)\right) - 6t_2]\end{aligned} \tag{A.6}$$

$$\begin{aligned}\mathbb{H}_{2,\pm\boldsymbol{K}}(t_2,\phi) = \frac{\csc(\phi)}{16t_2\left(6t_2\cot(\phi) + 2\sqrt{3}t_2 - 3\csc(\phi)\right)}[-36t_2^3 + 24t_2^2\cos(\phi) \\ + \sqrt{3}\left(4t_2^2\sin(\phi)(5 - 12t_2\cos(\phi)) + 6t_2\cot(\phi) - 3\csc(\phi)\right) + 6t_2]\end{aligned} \tag{A.7}$$

$$\mathbb{H}_{3,\pm\boldsymbol{K}}(t_2,\phi)=\frac{1}{8}\left(\frac{3-6t_2\cos(\phi)}{8t_2^2\cos(2\phi)+4t_2^2-12t_2\cos(\phi)+3}+6t_2\cos(\phi)-1\right), \quad \text{(A.8)}$$

where $\gamma = \sqrt{t_2^2-2t_2\cos(\phi)+1}$. At specific (t_2,ϕ) values in the parameter space, the $\pm\boldsymbol{K}$ points on either pair of neighboring bands will touch. Due to the no-level crossing theorem under the PT framework, we want to emphasize the $\mathbb{H}_{n,\boldsymbol{K}}$ expressions are only valid in some regions of the parameter space. The band-crossing happens at a set of (t_2,ϕ) values, related by the function $t_2 = \frac{3}{2\left(\sqrt{3}\sin(\phi)+3\cos(\phi)\right)}$. Starting from the NN kagome model, i.e. $(t_2,\phi)=(0,0)$, once the critical (t_2,ϕ) line is crossed, the Hessian expressions for $\pm\boldsymbol{K}$, as given in Eqs.(A.6)-(A.8), become mixed and do not correspond to the correct band index n. However, we wish to point out that upon plotting the roots of all three $\mathbb{H}_{n,\pm\boldsymbol{K}}$ expressions, we do obtain the complete set of HOVHS lines for the $\pm\boldsymbol{K}$ points in the parameter space.

Appendix B

Exact Diagonalization of a Large Matrix using the Sakurai-Sugiura Method

In this appendix, we provide a detailed account of the exact diagonalization process for a large matrix of dimensions (124002×124002). Given the requirement to obtain all eigenvalues and eigenvectors of the matrix, conventional sparse matrix techniques like single value decomposition, Lanczos algorithm, and Arnoldi iteration proved inadequate. Consequently, we employed the Sakurai-Sugiura method, [218] which is particularly well-suited for large-scale eigenproblems.

The Sakurai-Sugiura method utilizes contour integration to isolate and compute the desired eigenvalues within a specified region of the complex plane. This method involves integrating the resolvent of the matrix along a contour in the complex plane. Specifically, for a given matrix A, the resolvent $R(z) = (zI - A)^{-1}$ is integrated along a contour Γ enclosing the eigenvalues of interest. The eigenvalues are then extracted from the poles of the resolvent. This method is highly efficient for large matrices because it allows for the parallel computation of the integrals, leveraging

numerical techniques such as Gauss-Legendre quadrature for accurate and efficient integration.

In this work, we implemented the Sakurai-Sugiura method in Julia to diagonalize a large Hamiltonian matrix. The libraries utilized include `LinearAlgebra`, `SparseArrays`, `Distributed`, and `FastGaussQuadrature`. We developed a function that takes as input the matrix A to be diagonalized, the range of eigenvalues specified by a and b, and the number of eigenvalues and eigenvectors to be output, N. The function operates as follows:

1. The contour in the complex plane is defined and discretized using Gauss-Legendre quadrature [219].

2. A function is defined to compute the resolvent of the matrix A at a given point z.

3. The resolvent is integrated along the contour using the quadrature points t and weights w, resulting in a projection matrix P. This step is parallelized to enhance computational efficiency.

4. The eigenvalues and eigenvectors of the projection matrix P are extracted using standard eigenvalue decomposition techniques.

Appendix C

Confirming the Absence of Multifractality in Dirac Fractals

As shown in Fig. 4.5, the $q = 2$ scaling dimension D_q of the manifold of Dirac surface states above the shifted Dirac point E_D is very close to the fractal dimension of the Sierpiński carpet. While it strongly suggests that the surface states exhibit fractal scaling behavior for $q = 2$, it does not rule out the possibility of multifractality where the scaling exponent D_q varies with q. Hence, we calculate the scaling exponents for $q = 1.5$ and $q = 3$, and we obtain $D_3 = 1.86 \pm 0.04$ and $D_{1.5} = 1.895 \pm 0.008$, as shown in Fig. C.1. We can notice that $D_2 \approx D_{1.5} \approx D_3$, which strongly indicates the absence of multifractal behavior.

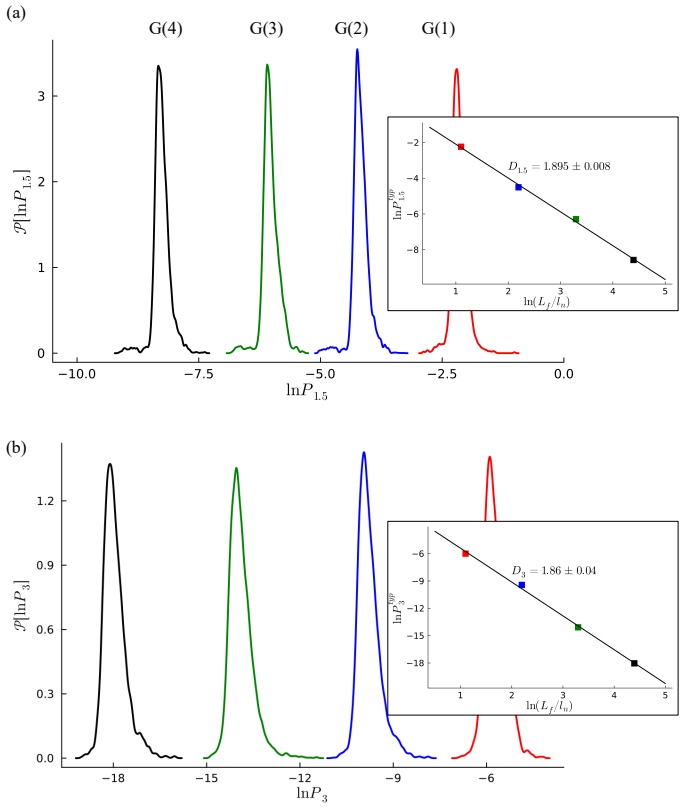

Figure C.1: Distribution of the IPR logarithm, $\mathcal{P}[\ln P_q]$ of the class of states above E_D, for each of the first four generations of the Sierpiński carpet fractal potential of strength $V = -0.25\,t$, for (a) $q = 1.5$, (b) $q = 3$. The log-log scaling of the corresponding typical values $\ln P_q^{typ}$ with the linear dimension $L_f/l_n = 3^n$ are shown in the inset, where the scaling dimensions $D_{1.5}$ and D_3 are given by the corresponding regression slopes.

Appendix D

Sierpiński Gasket Geometry on 3D TI Surface

Note: The results given in this appendix have not been published.

In this section, we study a model of the 3D TI surface featuring a Sierpiński gasket geometry, as shown in Figure D.1(b). The model consists of the surface Dirac cone of 3D TI, described by a continuum Dirac Hamiltonian, coupled with a time-reversal symmetric scalar potential $V(\boldsymbol{r})$. The model is described by the Hamiltonian

$$H = v_F\big(\boldsymbol{\sigma} \times \mathbf{p}\big) + V(\mathbf{r})\sigma_0 \tag{D.1}$$

where v_F is the Fermi velocity, $\mathbf{p}$ is the momentum, $\boldsymbol{\sigma} = \big(\sigma_x, \sigma_y, \sigma_z\big)$ are the Pauli matrices, σ_0 is the identity matrix and $V(\mathbf{r})$ is the time-reversal symmetric fractal potential that models the electron scattering centers deposited on the TI surface in a Sierpiński gasket geometry, using muffin-tin approximation.

The Sierpiński gasket is a fractal set with a triangular shape, created by recursively subdividing an equilateral triangle into smaller equilateral triangles and removing the central triangle at each iteration. For a generation n Sierpiński gasket $G(n)$, the fractal is constructed by recursively removing the central triangle from

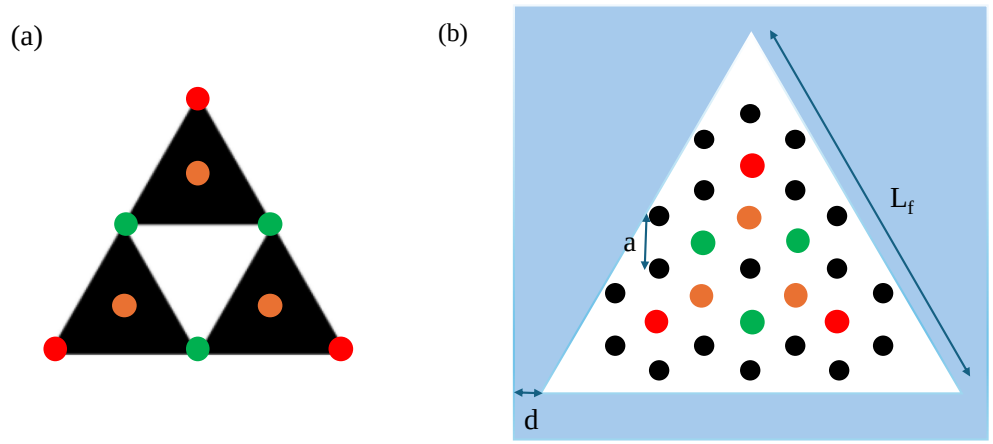

Figure D.1: (a) Schematic of the G(1) Sierpiński gasket with its lattice sites marked in red and green. The lattice sites of the dual of the G(1) Sierpiński gasket are marked in orange. (b)Schematic of the surface of a 3D TI deposited with electron scattering centers represented as muffin-tins(black circles) of radius $r_0 = \frac{a}{4}$, around the lattice sites of the first generation G(1) Sierpinski gasket (red and green circles) and its dual (orange circles). The nearest distance between two scattering centers is a. A constant Zeeman field is turned on in the area shaded in light blue. The white region along with the sites of the Sierpinski gasket and its dual, that is enclosed by the scattering centers is referred to as the fractal region. Additionally, the triangular region (shown in white) that encloses the fractal region is placed at least $d = 3a$ distance away from the boundary of the TI surface in order to avoid the influence of the boundary on the surface states coupled to the fractal geometry.

each larger triangle. For instance, a $G(1)$ unit which is shown in Fig. D.1(a), is created by removing the central equilateral triangle of the $G(0)$ unit which is a two-dimensional equilateral triangle.

At each generation n, $G(n)$ consists of $N_n = 3^n$ smaller triangles, each with a side length $l_n = \frac{L_f}{2^n}$. Using the relationship $N_n = \left(\frac{L_f}{l_n}\right)^D$, we find the Hausdorff dimension D of the Sierpiński gasket as $D = \frac{\ln 3}{\ln 2} \approx 1.585$. This dimension indicates the scaling behavior of the fractal, which is observed for boxes of size $l_n < l < l_1$, with no scaling behavior below the length scale l_n.

The fractal potential $V(\mathbf{r})$ introduces the fractal geometry of the Sierpiński gasket to the 3D TI surface by modeling electron scattering centers, [80] as depicted in

Fig. D.1(b), using muffin-tin approximation. $V(\mathbf{r})$ consists of a network of potential barriers of height V arranged such that

$$V(\mathbf{r}) = \begin{cases} V > 0 & \mathbf{r} \in \mathcal{R}_{scattering} \\ 0 & \text{otherwise} \end{cases} \tag{D.2}$$

where $\mathcal{R}_{scattering}$ represents all the electron scattering centers of radius r_0, shown in Fig. D.1(b).

Furthermore, as shown in Fig. D.1(b), there is a significant amount of space on the TI surface outside the fractal region, which is shaded in blue. This is due to the fundamental difference in the shapes of the 3D TI surface considered and the G(0) Sierpiński gasket, which is triangular. Since we aim to study the surface states coupled with fractal geometry, a magnetic field is introduced around the region containing the fractal potential on the TI surface, as depicted in Fig. D.1(b). The Hamiltonian of the model can now be expressed as

$$H = v_F\big(\boldsymbol{\sigma} \times \mathbf{p}\big) + V(\mathbf{r})\sigma_0 + h(\mathbf{r})\sigma_z \tag{D.3}$$

where $h(\mathbf{r})$ is the magnetic field around the fractal region. This Zeeman field breaks the global time-reversal symmetry. Since the objective is to study surface states with time-reversal symmetry in the presence of a fractal potential, the focus is narrowed to the states that lie within the Zeeman gap.

D.1 Numerical analysis of the model

The eigenvalues and eigenvectors of the Hamiltonian described in Eq. D.3 are numerically determined through exact diagonalization for various strengths and generations of the fractal potential $V(\mathbf{r})$. In all scenarios, the Hamiltonian is an-

alyzed with a Zeeman field strength $h \approx t$ where $t = (\hbar v_F/a)$, which induces a Zeeman gap with a bandwidth of $2t$ within which the surface states are expected to be time-reversal symmetric.

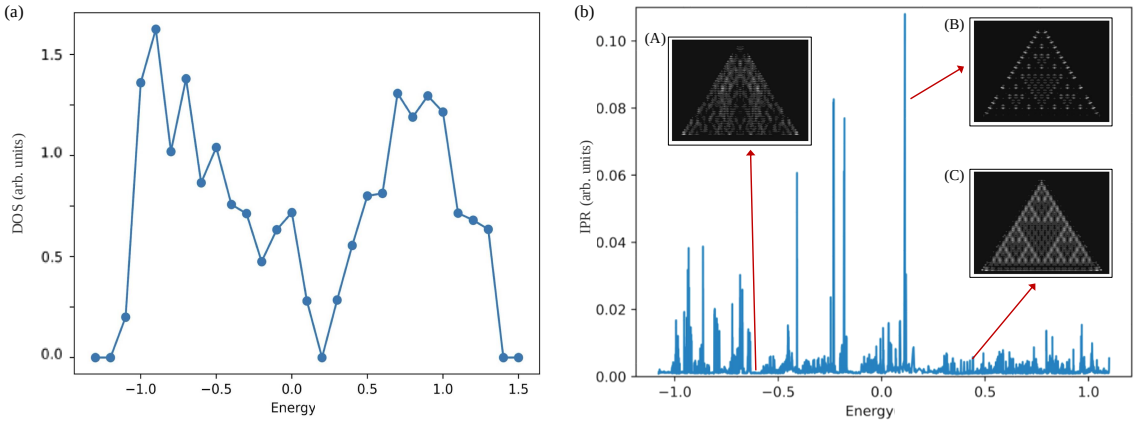

Figure D.2: (a) Density of states plotted against energy in units of t for G(4) fractal potential with strength $V = 0.2t$. Notice that the DOS vanishes at $E_D = 0.21t$, indicating that the Zeeman field around the fractal region does not gap the spectrum. (b) The $q = 2$ moment of IPR of each individual state plotted against energy in units of t for the same fractal potential as in (a). The LDOS maps of the states that lie within an energy window of width $\Delta E = 0.05t$ around (A) $E = -0.72t$,(B) $E = 0.18t$ and (C) $E = 0.37t$, as indicated by the arrows, are shown on the inset. Notice that the region outside the triangle, where the Zeeman field is applied, exhibits no LDOS contribution, as the considered bandwidth W is within the Zeeman gap

The DOS for the states within the Zeeman gap is depicted in Figure D.2(a) for a $G(4)$ fractal potential with a strength of $V = 0.2t$. In the presence of the fractal potential, the DOS vanishes at $E = E_D$, as shown in Figure D.2(a), indicating that the Zeeman field around the fractal region does not gap the spectrum. This suggests that the eigenstates within the Zeeman gap retain time-reversal symmetry. Furthermore, we find that as the strength of the fractal potential increases, the Dirac point shifts along the energy axis. Our numerical analysis confirms that the energy shift E_D is directly proportional to the fractal potential strength V, with the Dirac point moving down (up) in energy as V becomes more negative (positive).

Additionally, our analysis focuses on surface states within a bandwidth $W = 2t$, centered around the shifted Dirac point E_D.

To probe the localization properties of eigenstates $\psi(\mathbf{r})$, we employ the inverse participation ratio, [196]

$$IPR_q = \sum_i |\psi(\mathbf{r}_i)|^{2q} \tag{D.4}$$

where i is summed over all the lattice points of the system and $q \in \mathbb{R}$. When $q = 1$, $IPR_{q=1} = 1$ due to the normalization of the wave function. Hence, we focus on $q > 1$ modes of the IPR.

In Fig. D.2(b), we present the second moment of the IPR ($IPR_{q=2}$), calculated numerically for each eigenstate associated with the $G(4)$ fractal potential. The states within the considered energy window exhibit IPR peaks of varying heights, indicating that the individual eigenstates possess different IPR values and, consequently, different spatial distributions of the LDOS. But interestingly, when we consider the LDOS map averaged over in energy that corresponds to the states in an energy window of width $\Delta E \sim 10^{-2}\, t$, we find the emergence of three characteristic LDOS profiles shown in the inset of Fig. D.2 (b). Based on these profiles, we can categorize all eigenstates within the considered energy bandwidth W into three distinct classes. Notice that unlike in the case of the Sierpiński carpet where we find two classes of states that are separated by the energy scale E_D, in this case, the different classes of states are observed throughout the considered energy window of bandwidth W without a set energy scale to separate them.

The first class, denoted as class A, is characterized by the LDOS distribution demonstrated in LDOS profile (A) shown in the inset of Figure D.2(b). This LDOS distribution appears to have similar contributions from both the fractal region and the scattering centers, indicating that the probability of finding electrons is similar across the two-dimensional triangular region on the TI surface with no Zeeman field, shown in Fig. D.1(b). Consequently, these states exhibit no fractal scaling

behavior and have shorter IPR peaks. Furthermore, we confirm that these results have been observed for the first four generations of the Sierpiński gasket fractal potential.

The eigenstates falling under class B, as demonstrated in LDOS profile (B) shown in the inset of Fig. D.2(b), have an LDOS distribution where the probability of finding electrons is higher on the scattering centers than the fractal region. As a result, they exhibit a geometry that lacks self-similarity, indicating the absence of fractal scaling behavior. Additionally, LDOS profile (B) reveals that the region with a higher LDOS contribution, i.e., the region occupied by the scattering centers, occupies less area compared to the LDOS contribution shown in profile (A) for the $G(4)$ fractal potential. Since the IPR is inversely proportional to the area, the eigenstates in class B exhibit more prominent IPR peaks than those in class A. Furthermore, as the fractal generation n increases, the ratio of the area occupied by the scattering centers to the area of the entire triangular region also increases. As $n \to \infty$, the fractal dimension of the region occupied by the scattering centers approaches that of the triangular region, which is two. Consequently, the IPR peaks corresponding to class B states become less prominent with increasing fractal generation.

Unlike the eigenstates in class B, the ones in class C, as demonstrated in LDOS profile (C) shown in the inset of Fig. D.2(b), have an LDOS distribution where the probability of finding electrons is higher in the fractal region than in the region occupied by the scattering centers. Consequently, we find the emergence of eigenstates that could exhibit the scaling behavior of the Sierpiński gasket geometry. Additionally, we observe that these eigenstates exhibit IPR peaks that are more prominent than those shown by class A states while less shorter than those shown by class B states, for the $G(4)$ fractal potential. This observation aligns with the fact that the area of the fractal region is larger than that of the region outside the fractal

region for smaller fractal generations such as $n = 4$. Furthermore, as the fractal generation n increases, the ratio of the areas of the fractal region to the triangular region remains constant, unlike the region occupied by the scattering centers. As a result, the IPR peaks of class C eigenstates become more prominent, while those of class B states grow short as $n \to \infty$. [196–198]

While the LDOS maps provide important visual guidance of the onset of Dirac states with fractal dimension, we confirm that the surface states in class C indeed inherit the scaling properties of the Sierpiński gasket fractal by calculating their fractal dimensions through IPR scaling and box-counting methods.

D.1.1 Scaling of the IPR logarithm

In this section, we present numerical evidence demonstrating that the eigenstates in class C exhibit the scaling behavior characteristic of the Sierpiński gasket geometry, as indicated by the scaling of the corresponding IPR distribution. If the wave functions within a specific energy window, which display similar LDOS profiles, are scale-invariant over a range of length scales l with $a \ll l \ll L_f$, the distribution of the IPR logarithms $\mathcal{P}[\ln IPR_q]$, scaled by a typical IPR IPR_q^{typ}, where IPR_q^{typ} can be the mean of the IPR distribution, assumes a scale-invariant form. The scaling properties of the IPR are encapsulated in IPR_q^{typ}, which in this context satisfies $IPR_q^{typ} \propto (L_f/l_n)^{-D_q(q-1)}$, where D_q is the fractal dimension of the states.

In order to evaluate the fractal dimension of the eigenstates in class C, we begin by examining the distributions of the IPR logarithm. Unlike the Sierpiński carpet, where fractal scaling behavior is observed within a single energy window of width approximately half the corresponding bandwidth, the eigenstates exhibiting fractal scaling behavior in class C are dispersed across the considered energy window of bandwidth W. Consequently, we obtain $\mathcal{P}[\ln IPR_q]$ for each set of eigenstates in class C. Due to the lack of a distinct energy scale separating the eigenstates of

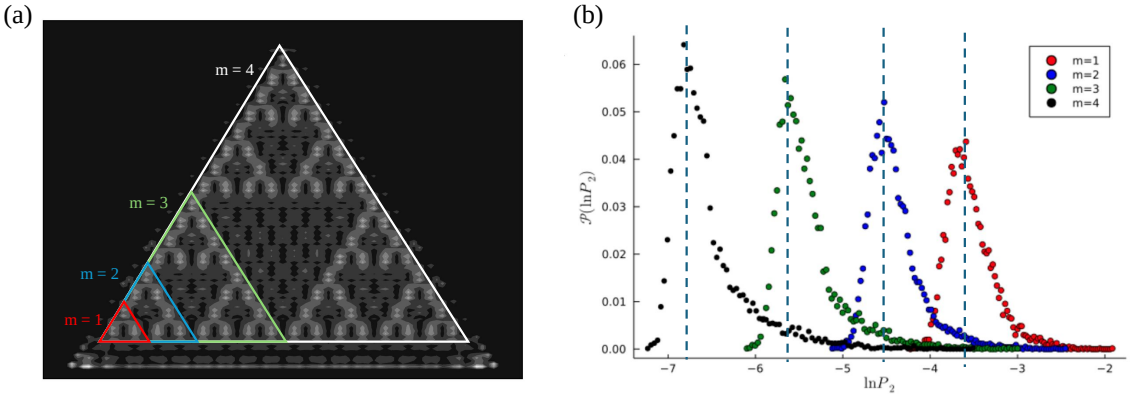

Figure D.3: (a) LDOS profile of a set of eigenstates that lie within an energy window of width $\Delta E = 0.05t$ around $E = 0.37t$ for the $G(4)$ fractal potential. The white, green, blue, and red triangles mark the $G(4)$, $G(3)$, $G(2)$, and $G(1)$ units of the $G(4)$ Sierpiński carpet fractal respectively. The corresponding fractal generation m of the units have also been denoted to their left. (b) Distribution of the IPR logarithm, $\mathcal{P}[\ln P_2]$ of the set of states considered in (a), for each of the first four generations of the Sierpiński gasket fractal potential of strength $V = 0.2\,t$. The dashed line indicates the mean $\ln P_2^{typ}(m)$ of the corresponding $\mathcal{P}[\ln P_2](m)$.

different classes, the IPR distributions for various fractal generations n cannot be used to calculate the fractal dimension of the states. Therefore, we derive the IPR distribution for fractal generation $m \leq 4$ from the eigen data obtained for the $G(4)$ fractal potential. Specifically, consider the LDOS profile of a set of eigenstates in class C corresponding to the $G(4)$ fractal potential, as shown in Fig. D.3(a). Within the white triangle denoting a $G(4)$ unit, we can identify copies of $G(3)$, $G(2)$, and $G(1)$ units, marked by green, blue, and red triangles, respectively. By restricting the IPR calculation of each state within the red triangle with $L_f/l_1 = 2$, we obtain a distribution of effective IPR values $P_q(m = 1)$ for generation $m = 1$. Similarly, distributions of such effective IPR values, $\mathcal{P}[P_q](m)$, can be obtained for $m \leq 4$. Subsequently, the fractal dimension D_q of the eigenstates can be obtained from the scaling relation given by

$$P_q^{typ} \propto \left(\frac{L_f}{l_n}\right)^{-D_q(q-1)}, \tag{D.5}$$

where P_q^{typ} is defined as the mean of the $\mathcal{P}[P_q]$.

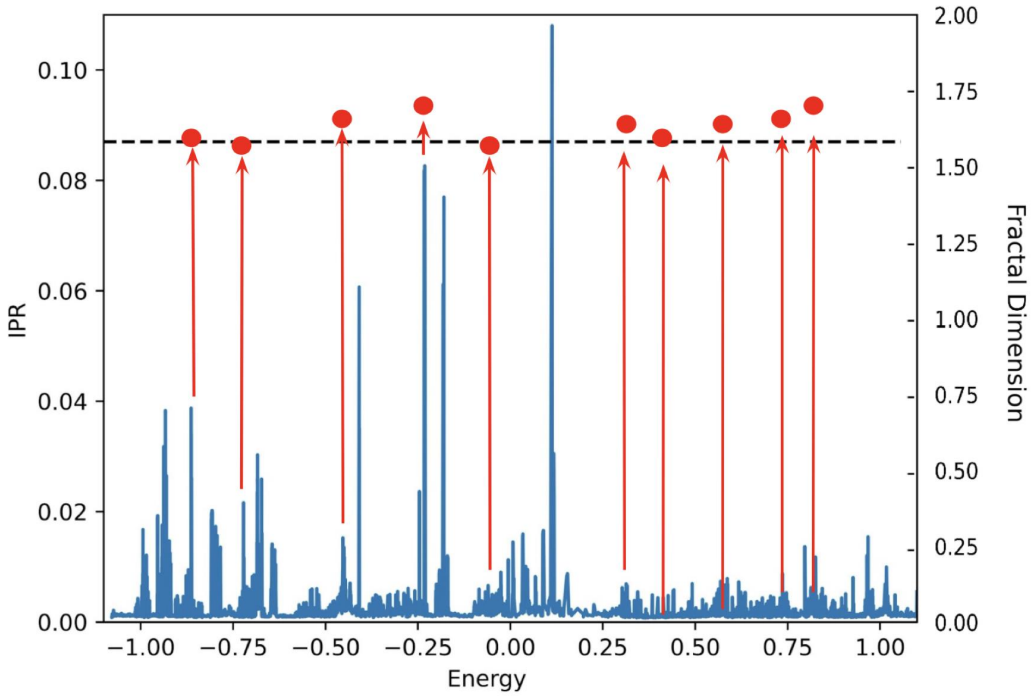

Figure D.4: Fractal dimension D_2 calculated using Eq. (D.5), for the different sets of eigenstates that fall under class C (shown on the right axis) and the corresponding IPR of the individual eigenstates (shown on the left axis) plotted as a function of the energy for the $G(4)$ fractal potential with $V = 0.2\,t$. Notice that all these sets of states have fractal dimensions close to that of the Sierpiński gasket fractal, which is denoted by the dashed line drawn at $D = 1.585$.

In Fig. D.3(b), we present the distributions of the IPR logarithm, $\mathcal{P} \ln P_2$, for the set of states depicted in Fig. D.3(a), for $m \leq 4$. We observe that as m increases, the distribution exhibits a sharper peak and narrower width. This phenomenon can be attributed to the increasing noise prominence when considering $G(m)$ units with smaller m values, which involve fewer lattice sites in the calculation of the corresponding effective IPR $P_2(m)$. Additionally, the distributions appear similar across all fractal generations, and we confirm that they largely overlap when shifted

along the horizontal axis. Furthermore, we compute the fractal dimension of this set of states using Eq. (D.5) and obtain $D_2 = 1.598 \pm 0.009$ which is very close to the fractal dimension of the Sierpiński gasket geometry, 1.585.

Similarly, we compute the $q = 2$ fractal dimension for the other sets of eigenstates that mirror the geometry of the Sierpiński gasket fractal, as shown in Fig. D.4. We find that these states also exhibit fractal dimension $D_2 \approx 1.585$, thereby providing strong evidence that the eigenstates falling under class C exhibit fractal scaling behavior with scaling exponent same as that of the Sierpiński gasket geometry. Additionally, due to the localization profile of the states changing over energy windows as narrow as $10^{-1}\,t$, we are unable to obtain the IPR logarithm distributions for $q > 1$. Consequently, we are unable to confirm the absence of multifractality in this case.

D.1.2 Box counting method

In this section, we confirm the fractal dimension of the class C states, obtained in Sec. D.1.1 using the Box-counting method applied to the LDOS. The box-counting dimension D of a LDOS map can be obtained from the scaling of the number $N(r)$ of boxes of size r that cover the LDOS map as a function of the system size $1/r$, as given by Eq. (4.7).

As discussed in Sec. 4.2.2, the box-counting dimension is influenced by the threshold α, which is defined such that LDOS values below α are set to zero and those above α are set to one in the binarized map. For each set of eigenstates shown in Fig. D.4, we apply the box-counting method across a range of α values. An example is provided in Fig. D.5(a), where we display the Minkowski-Bouligand dimension for an energy window of width $\Delta E = 0.01\,t$ around $E = 0.31\,t$ for a $G(4)$ fractal potential $V = 0.2\,t$, and for various binarization thresholds ranging from 0 to 1. The LDOS values are rescaled so that their minimum and maximum values are 0

and 1, respectively. When the threshold α is set close to zero, capturing contributions from even the smaller LDOS peaks, the LDOS landscape appears homogeneous, resulting in a box-counting dimension of two. As α increases, we observe a range of thresholds $\alpha \in [0.4, 0.65]$ that reveals the emergence of dominant LDOS peaks distributed across the fractal region, indicated by a plateau at $D = 1.589 \pm 0.004$. This value closely approximates the fractal dimension of the Sierpiński gasket.

Similarly, by employing the box-counting method on the other sets of eigenstates falling under class C, we numerically confirm that these sets of eigenstates exhibit fractal scaling behavior. Therefore, combined with the analysis of the IPR discussed in Sec. D.1.1, we confirm the emergence of Dirac surface states that inherit the geometry of the Sierpiński gasket fractal.

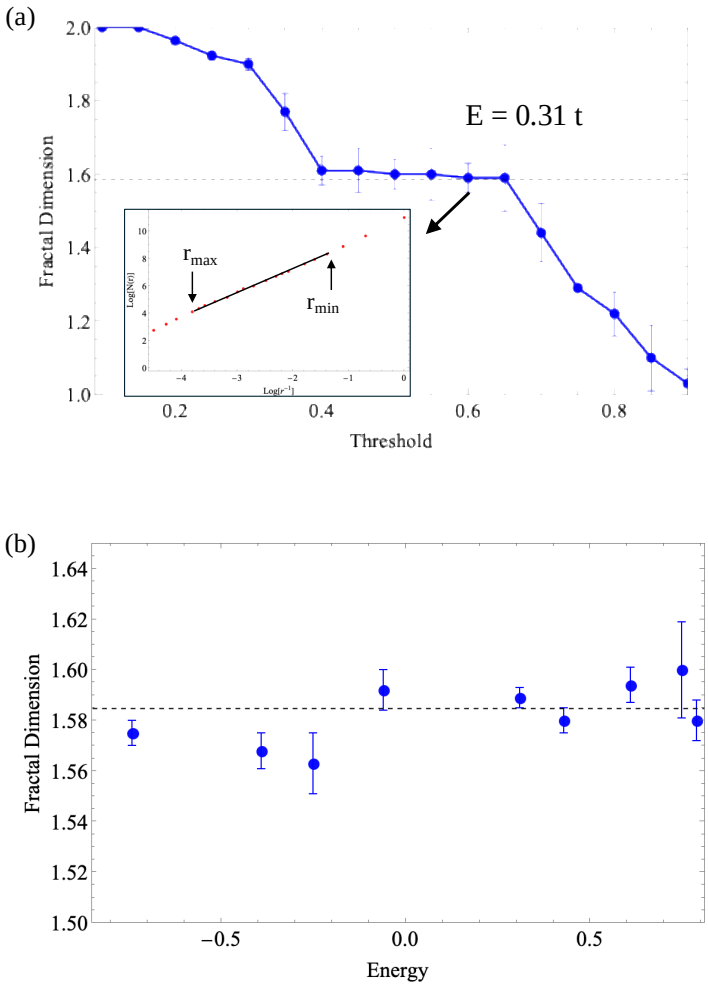

Figure D.5: (a) Fractal dimension D of the states within an energy window of width $\Delta E = 0.01t$ around $E = 0.31\,t$, for a $G(4)$ fractal potential of strength $V = 0.2\,t$, calculated using the box-counting method, plotted against the binarization threshold, α. The plateau at $D = 1.589 \pm 0.004$ indicates the fractal dimension for threshold values ranging from 0.4 to 0.65. Inset shows the log-log plot of $N(r)$ vs $1/r$ corresponding to the threshold $\alpha = 0.6$. Here, r_{min} and r_{max}, respectively, denote the minimum and maximum box sizes chosen to estimate the box-counting dimension of the states. (b) Fractal dimensions of class C states as a function of the corresponding energy values for a $G(4)$ Sierpiński gasket fractal potential of strength $V = 0.2\,t$, calculated using the box-counting method, as shown in (a). The black dashed line in (a) and (b) marks the fractal dimension of the Sierpiński gasket at $D = 1.585$.

Bibliography

[1] Koen Schouteden, Zhe Li, Taishi Chen, Fengqi Song, Bart Partoens, Chris Van Haesendonck, and Kyungwha Park. Moiré superlattices at the topological insulator bi2te3. *Scientific Reports*, 6(1):20278, 2016.

[2] YL Chen, James G Analytis, J-H Chu, ZK Liu, S-K Mo, Xiao-Liang Qi, HJ Zhang, DH Lu, Xi Dai, Zhong Fang, et al. Experimental realization of a three-dimensional topological insulator, bi2te3. *Science*, 325(5937):178–181, 2009.

[3] N. W. Ashcroft and N. D. Mermin. *Solid State Physics*. Holt, Rinehart and Winston, 1976.

[4] Charles Kittel and Paul McEuen. *Introduction to solid state physics*. John Wiley & Sons, 2018.

[5] Heinz Hopf. Vektorfelder in n-dimensionalen mannigfaltigkeiten. In *Collected Papers-Gesammelte Abhandlungen*, pages 87–112. Springer, 2001.

[6] Léon Van Hove. The occurrence of singularities in the elastic frequency distribution of a crystal. *Phys. Rev.*, 89:1189–1193, Mar 1953.

[7] Yuan Cao, Valla Fatemi, Shiang Fang, Kenji Watanabe, Takashi Taniguchi, Efthimios Kaxiras, and Pablo Jarillo-Herrero. Unconventional superconduc-

tivity in magic-angle graphene superlattices. *Nature*, 556(7699):43–50, April 2018. Number: 7699 Publisher: Nature Publishing Group.

[8] X. Lu, Y. Zhao, T. Zhang, Z. Sun, Y. Jia, C. Liu, C. Xu, C.-C. Lee, C. Gu, X. C. Xie, et al. Superconductivity protected by time-reversal symmetry in $1t$-tas_2. *Nature*, 527(7577):68–72, 2015.

[9] S. Sasaki, M. Kriener, K. Segawa, K. Yonezawa, S. Maekawa, and Y. Ando. Evidence for two-dimensional ising superconductivity in bi2se3. *Physical Review Letters*, 107(21):217001, 2015.

[10] Hiroki Isobe, Noah F.âQ. Yuan, and Liang Fu. Unconventional Superconductivity and Density Waves in Twisted Bilayer Graphene. *Physical Review X*, 8(4):041041, December 2018. Publisher: American Physical Society.

[11] Yury Sherkunov and Joseph J. Betouras. Electronic phases in twisted bilayer graphene at magic angles as a result of Van Hove singularities and interactions. *Phys. Rev. B*, 98:205151, Nov 2018.

[12] Cheng-Cheng Liu, Li-Da Zhang, Wei-Qiang Chen, and Fan Yang. Chiral spin density wave and $d + id$ superconductivity in the magic-angle-twisted bilayer graphene. *Phys. Rev. Lett.*, 121:217001, Nov 2018.

[13] Dante M. Kennes, Johannes Lischner, and Christoph Karrasch. Strong correlations and $d + id$ superconductivity in twisted bilayer graphene. *Phys. Rev. B*, 98:241407, Dec 2018.

[14] Yi-Zhuang You and Ashvin Vishwanath. Superconductivity from valley fluctuations and approximate SO(4) symmetry in a weak coupling theory of twisted bilayer graphene. *npj Quantum Materials*, 4(1):16, Apr 2019.

[15] Yu-Ping Lin and Rahul M. Nandkishore. Parquet renormalization group analysis of weak-coupling instabilities with multiple high-order Van Hove points inside the Brillouin zone. *Phys. Rev. B*, 102:245122, Dec 2020.

[16] Yi-Ting Hsu, Fengcheng Wu, and S. Das Sarma. Topological superconductivity, ferromagnetism, and valley-polarized phases in moiré systems: Renormalization group analysis for twisted double bilayer graphene. *Phys. Rev. B*, 102:085103, Aug 2020.

[17] Laura Classen, Andrey V. Chubukov, Carsten Honerkamp, and Michael M. Scherer. Competing orders at higher-order Van Hove points. *Physical Review B*, 102(12):125141, September 2020. Publisher: American Physical Society.

[18] Dmitry V. Chichinadze, Laura Classen, and Andrey V. Chubukov. Nematic superconductivity in twisted bilayer graphene. *Phys. Rev. B*, 101:224513, Jun 2020.

[19] H. J. Schulz. Superconductivity and Antiferromagnetism in the Two-Dimensional Hubbard Model: Scaling Theory. *Europhysics Letters (EPL)*, 4(5):609–615, September 1987. Publisher: IOP Publishing.

[20] Rahul Nandkishore, L. S. Levitov, and A. V. Chubukov. Chiral superconductivity from repulsive interactions in doped graphene. *Nature Physics*, 8(2):158–163, Feb 2012.

[21] Daniel Shaffer, Jian Wang, and Luiz H. Santos. Unconventional self-similar hofstadter superconductivity from repulsive interactions. *Nature Communications*, 13(1):7785, Dec 2022.

[22] Daniel Shaffer and Luiz H Santos. Triplet pair density wave superconductivity on the π-flux square lattice. *Physical Review B*, 108(3):035135, 2023.

[23] F. Sohier, M. Calandra, and F. Mauri. Charge density wave instabilities driven by van hove singularities in twisted bilayer graphene. *Physical Review B*, 96(7):075449, 2017.

[24] Y. Jiang, X. Lai, K. Kong, S. Park, Y. Cao, K. Watanabe, T. Taniguchi, K. F. Mak, C. R. Dean, and P. A. Lee. Charge order and broken rotational symmetry in magic-angle graphene. *Nature*, 573(7773):91–95, 2019.

[25] B. Kannan, J. Park, L. Xian, K. Watanabe, T. Taniguchi, K. Watanabe, T. Taniguchi, D. Miller, and P. Jarillo-Herrero. Observation of topological valleytronics in twisted bilayer graphene. *Nature*, 567(7746):438–442, 2019.

[26] G. Chen, A. L. Sharpe, E. M. Yuan, E. Navarro-Moratalla, Y. Yang, Z. Kashti, L. Zhang, J. Lee, H. Wang, Y. Shi, et al. Correlated insulator and metal states in twisted double bilayer graphene. *Nature*, 572(7769):215–219, 2019.

[27] Y. Choi, J. Choi, Y. Kim, Y. Park, J. Kim, J. H. Lee, K. Watanabe, T. Taniguchi, and P. Kim. Correlated insulating behaviour at half-filling in magic-angle graphene superlattices. *Nature*, 556(7702):42–46, 2018.

[28] Alex Shtyk, Garry Goldstein, and Claudio Chamon. Electrons at the monkey saddle: A multicritical lifshitz point. *Physical Review B*, 95(3):035137, 2017.

[29] Noah FQ Yuan, Hiroki Isobe, and Liang Fu. Magic of high-order van hove singularity. *Nature communications*, 10(1):5769, 2019.

[30] Taige Wang, Noah FQ Yuan, and Liang Fu. Moiré surface states and enhanced superconductivity in topological insulators. *Physical Review X*, 11(2):021024, 2021.

[31] Yury Sherkunov and Joseph J Betouras. Electronic phases in twisted bilayer

graphene at magic angles as a result of Van Hove singularities and interactions. *Physical Review B*, 98(20):205151, 2018.

[32] Dmitry V Efremov, Alex Shtyk, Andreas W Rost, Claudio Chamon, Andrew P Mackenzie, and Joseph J Betouras. Multicritical Fermi surface topological transitions. *Physical Review Letters*, 123(20):207202, 2019.

[33] Alexander Kerelsky, Leo J McGilly, Dante M Kennes, Lede Xian, Matthew Yankowitz, Shaowen Chen, K Watanabe, T Taniguchi, James Hone, Cory Dean, et al. Maximized electron interactions at the magic angle in twisted bilayer graphene. *Nature*, 572(7767):95–100, 2019.

[34] Yu-Ping Lin and Rahul M Nandkishore. Parquet renormalization group analysis of weak-coupling instabilities with multiple high-order Van Hove points inside the Brillouin zone. *Physical Review B*, 102(24):245122, 2020.

[35] Laura Classen, Andrey V Chubukov, Carsten Honerkamp, and Michael M Scherer. Competing orders at higher-order Van Hove points. *Physical Review B*, 102(12):125141, 2020.

[36] Yi-Ting Hsu, Fengcheng Wu, and S Das Sarma. Spin-valley locked instabilities in moiré transition metal dichalcogenides with conventional and higher-order Van Hove singularities. *Physical Review B*, 104(19):195134, 2021.

[37] Zhen Bi and Liang Fu. Excitonic density wave and spin-valley superfluid in bilayer transition metal dichalcogenide. *Nature communications*, 12(1):642, 2021.

[38] Mingu Kang, Shiang Fang, Jeong-Kyu Kim, Brenden R Ortiz, Sae Hee Ryu, Jimin Kim, Jonggyu Yoo, Giorgio Sangiovanni, Domenico Di Sante, Byeong-Gyu Park, et al. Twofold Van Hove singularity and origin of charge order in

topological kagome superconductor CsV_3Sb_5. *Nature Physics*, 18(3):301–308, 2022.

[39] Yong Hu, Xianxin Wu, Brenden R Ortiz, Sailong Ju, Xinloong Han, Junzhang Ma, Nicholas C Plumb, Milan Radovic, Ronny Thomale, Stephen D Wilson, et al. Rich nature of Van Hove singularities in kagome superconductor CsV_3Sb_5. *Nature Communications*, 13(1):2220, 2022.

[40] Yi-Ming Wu, Zhengzhi Wu, and Hong Yao. Pair-density-wave and chiral superconductivity in twisted bilayer transition metal dichalcogenides. *Physical Review Letters*, 130(12):126001, 2023.

[41] Nicholas Read and Dmitry Green. Paired states of fermions in two dimensions with breaking of parity and time-reversal symmetries and the fractional quantum hall effect. *Physical Review B*, 61(15):10267, 2000.

[42] Jason Alicea. New directions in the pursuit of majorana fermions in solid state systems. *Reports on progress in physics*, 75(7):076501, 2012.

[43] Chetan Nayak, Steven H Simon, Ady Stern, Michael Freedman, and Sankar Das Sarma. Non-abelian anyons and topological quantum computation. *Reviews of Modern Physics*, 80(3):1083–1159, 2008.

[44] Roman M Lutchyn, Jay D Sau, and S Das Sarma. Majorana fermions and a topological phase transition in semiconductor-superconductor heterostructures. *Physical review letters*, 105(7):077001, 2010.

[45] Jay D Sau, Roman M Lutchyn, Sumanta Tewari, and Sankar Das Sarma. Generic new platform for topological quantum computation using semiconductor heterostructures. *Physical review letters*, 104(4):040502, 2010.

[46] JK Jain. Theory of the fractional quantum hall effect. *Physical Review B*, 41(11):7653, 1990.

[47] Bertrand I Halperin and Jainendra K Jain. *Fractional quantum hall effects: new developments*. World Scientific, 2020.

[48] Pedro Castro, Daniel Shaffer, Yi-Ming Wu, and Luiz H. Santos. Emergence of the chern supermetal and pair-density wave through higher-order van hove singularities in the haldane-hubbard model. *Phys. Rev. Lett.*, 131:026601, Jul 2023.

[49] Joel E Moore. The birth of topological insulators. *Nature*, 464(7286):194–198, 2010.

[50] M Zahid Hasan and Charles L Kane. Colloquium: topological insulators. *Reviews of modern physics*, 82(4):3045, 2010.

[51] Xiao-Liang Qi and Shou-Cheng Zhang. Topological insulators and superconductors. *Reviews of Modern Physics*, 83(4):1057, 2011.

[52] R. Yu, W. Zhang, H.-J. Zhang, S.-C. Zhang, X. Dai, Z. Fang, and X. Zhang. Quantized anomalous hall effect in magnetic topological insulators. *Science*, 329(5987):61–64, 2010.

[53] Cui-Zu Chang, Jinsong Zhang, Xiao Feng, Jie Shen, Zuocheng Zhang, Minghua Guo, Kang Li, Yunbo Ou, Pang Wei, Li-Li Wang, et al. Experimental observation of the quantum anomalous hall effect in a magnetic topological insulator. *Science*, 340(6129):167–170, 2013.

[54] Masatoshi Sato and Yoichi Ando. Topological superconductors: a review. *Reports on Progress in Physics*, 80(7):076501, 2017.

[55] B Andrei Bernevig. *Topological insulators and topological superconductors*. Princeton university press, 2013.

[56] A Yu Kitaev. Unpaired majorana fermions in quantum wires. *Physics-uspekhi*, 44(10S):131, 2001.

[57] CWJ Beenakker. Search for majorana fermions in superconductors. *Annu. Rev. Condens. Matter Phys.*, 4(1):113–136, 2013.

[58] Martin Leijnse and Karsten Flensberg. Introduction to topological superconductivity and majorana fermions. *Semiconductor Science and Technology*, 27(12):124003, 2012.

[59] Jia-Xin Yin, Biao Lian, and M Zahid Hasan. Topological kagome magnets and superconductors. *Nature*, 612(7941):647–657, 2022.

[60] Leon Balents. Spin liquids in frustrated magnets. *Nature*, 464(7286):199–208, 2010.

[61] Dmitry Green, Luiz Santos, and Claudio Chamon. Isolated flat bands and spin-1 conical bands in two-dimensional lattices. *Physical Review B—Condensed Matter and Materials Physics*, 82(7):075104, 2010.

[62] Kenya Ohgushi, Shuichi Murakami, and Naoto Nagaosa. Spin anisotropy and quantum Hall effect in the kagomé lattice: Chiral spin state based on a ferromagnet. *Physical Review B*, 62(10):R6065, 2000.

[63] Doron L Bergman, Congjun Wu, and Leon Balents. Band touching from real-space topology in frustrated hopping models. *Physical Review B—Condensed Matter and Materials Physics*, 78(12):125104, 2008.

[64] Yi Xiao, Vincent Pelletier, Paul M Chaikin, and David A Huse. Landau levels

in the case of two degenerate coupled bands: Kagomé lattice tight-binding spectrum. *Physical Review B*, 67(10):104505, 2003.

[65] Congjun Wu, Doron Bergman, Leon Balents, and S Das Sarma. Flat bands and Wigner crystallization in the honeycomb optical lattice. *Physical review letters*, 99(7):070401, 2007.

[66] Linda Ye, Mingu Kang, Junwei Liu, Felix Von Cube, Christina R Wicker, Takehito Suzuki, Chris Jozwiak, Aaron Bostwick, Eli Rotenberg, David C Bell, et al. Massive Dirac fermions in a ferromagnetic kagome metal. *Nature*, 555(7698):638–642, 2018.

[67] Mingu Kang, Linda Ye, Shiang Fang, Jhih-Shih You, Abe Levitan, Minyong Han, Jorge I Facio, Chris Jozwiak, Aaron Bostwick, Eli Rotenberg, et al. Dirac fermions and flat bands in the ideal kagome metal FeSn. *Nature materials*, 19(2):163–169, 2020.

[68] Kun Jiang, Tao Wu, Jia-Xin Yin, Zhenyu Wang, M Zahid Hasan, Stephen D Wilson, Xianhui Chen, and Jiangping Hu. Kagome superconductors AV_3Sb_5 (A= K, Rb, Cs). *National Science Review*, 10(2):nwac199, 2023.

[69] Maximilian L Kiesel and Ronny Thomale. Sublattice interference in the kagome hubbard model. *Physical Review B*, 86(12):121105, 2012.

[70] Xianxin Wu, Tilman Schwemmer, Tobias Müller, Armando Consiglio, Giorgio Sangiovanni, Domenico Di Sante, Yasir Iqbal, Werner Hanke, Andreas P Schnyder, M Michael Denner, et al. Nature of unconventional pairing in the kagome superconductors AV_3Sb_5 (A= K, Rb, Cs). *Physical review letters*, 127(17):177001, 2021.

[71] Yu-Xiao Jiang, Jia-Xin Yin, M Michael Denner, Nana Shumiya, Brenden R Ortiz, Gang Xu, Zurab Guguchia, Junyi He, Md Shafayat Hossain, Xiaoxiong

Liu, et al. Unconventional chiral charge order in kagome superconductor KV_3Sb_5. *Nature materials*, 20(10):1353–1357, 2021.

[72] Mingu Kang, Shiang Fang, Jonggyu Yoo, Brenden R Ortiz, Yuzki M Oey, Jonghyeok Choi, Sae Hee Ryu, Jimin Kim, Chris Jozwiak, Aaron Bostwick, et al. Charge order landscape and competition with superconductivity in kagome metals. *Nature Materials*, 22(2):186–193, 2023.

[73] Zuowei Liang, Xingyuan Hou, Fan Zhang, Wanru Ma, Ping Wu, Zongyuan Zhang, Fanghang Yu, J-J Ying, Kun Jiang, Lei Shan, et al. Three-dimensional charge density wave and surface-dependent vortex-core states in a kagome superconductor CsV_3Sb_5. *Physical Review X*, 11(3):031026, 2021.

[74] Yaojia Wang, Shuoying Yang, Pranava K Sivakumar, Brenden R Ortiz, Samuel ML Teicher, Heng Wu, Abhay K Srivastava, Chirag Garg, Defa Liu, Stuart SP Parkin, et al. Anisotropic proximity-induced superconductivity and edge supercurrent in kagome metal, $K_{1-x}V_3Sb_5$. *arXiv preprint arXiv:2012.05898*, 2020.

[75] Hong Li, He Zhao, Brenden R Ortiz, Takamori Park, Mengxing Ye, Leon Balents, Ziqiang Wang, Stephen D Wilson, and Ilija Zeljkovic. Rotation symmetry breaking in the normal state of a kagome superconductor KV_3Sb_5. *Nature Physics*, 18(3):265–270, 2022.

[76] Brenden R Ortiz, Lídia C Gomes, Jennifer R Morey, Michal Winiarski, Mitchell Bordelon, John S Mangum, Iain WH Oswald, Jose A Rodriguez-Rivera, James R Neilson, Stephen D Wilson, et al. New kagome prototype materials: discovery of KV_3Sb_5, RbV_3Sb_5, and CsV_3Sb_5. *Physical Review Materials*, 3(9):094407, 2019.

[77] Brenden R Ortiz, Samuel ML Teicher, Yong Hu, Julia L Zuo, Paul M Sarte,

Emily C Schueller, AM Milinda Abeykoon, Matthew J Krogstad, Stephan Rosenkranz, Raymond Osborn, et al. CsV_3Sb_5: A Z_2 topological kagome metal with a superconducting ground state. *Physical Review Letters*, 125(24):247002, 2020.

[78] Benoit B Mandelbrot. *The fractal geometry of nature*, volume 1. WH freeman New York, 1982.

[79] Benoit Mandelbrot. How long is the coast of britain? statistical self-similarity and fractional dimension. *science*, 156(3775):636–638, 1967.

[80] Sander N Kempkes, Marlou R Slot, Saoirsé E Freeney, Stephan JM Zevenhuizen, Daniel Vanmaekelbergh, Ingmar Swart, and C Morais Smith. Design and characterization of electrons in a fractal geometry. *Nature physics*, 15(2):127–131, 2019.

[81] IM Lifshitz et al. Anomalies of electron characteristics of a metal in the high pressure region. *Sov. Phys. JETP*, 11(5):1130–1135, 1960.

[82] I Dzyaloshinskii. Maximal increase of the superconducting transition temperature due to the presence of van't hoff singularities. *JETP Lett*, 46(3), 1987.

[83] R. S Markiewicz. A survey of the Van Hove scenario for high-tc superconductivity with special emphasis on pseudogaps and striped phases. *Journal of Physics and Chemistry of Solids*, 58(8):1179–1310, August 1997.

[84] Wan-Sheng Wang, Yuan-Yuan Xiang, Qiang-Hua Wang, Fa Wang, Fan Yang, and Dung-Hai Lee. Functional renormalization group and variational Monte Carlo studies of the electronic instabilities in graphene near $\frac{1}{4}$ doping. *Phys. Rev. B*, 85:035414, Jan 2012.

[85] Maximilian L. Kiesel, Christian Platt, Werner Hanke, Dmitry A. Abanin, and Ronny Thomale. Competing many-body instabilities and unconventional superconductivity in graphene. *Phys. Rev. B*, 86:020507, Jul 2012.

[86] J. González. Kohn-Luttinger superconductivity in graphene. *Phys. Rev. B*, 78:205431, Nov 2008.

[87] Shuang Wu, Zhenyuan Zhang, K. Watanabe, T. Taniguchi, and Eva Y. Andrei. Chern insulators, van Hove singularities and topological flat bands in magic-angle twisted bilayer graphene. *Nature Materials*, pages 1–7, February 2021. Publisher: Nature Publishing Group.

[88] Ömer M Aksoy, Anirudh Chandrasekaran, Apoorv Tiwari, Titus Neupert, Claudio Chamon, and Christopher Mudry. Single monkey-saddle singularity of a fermi surface and its instabilities. *Physical Review B*, 107(20):205129, 2023.

[89] F. D. M. Haldane. Model for a quantum hall effect without landau levels: Condensed-matter realization of the "parity anomaly". *Phys. Rev. Lett.*, 61:2015–2018, Oct 1988.

[90] Kenta Kuroda, Masashi Arita, Koji Miyamoto, Mao Ye, Jian Jiang, Akio Kimura, EE Krasovskii, EV Chulkov, Hideaki Iwasawa, Taichi Okuda, et al. Hexagonally deformed fermi surface of the 3d topological insulator bi 2 se 3. *Physical review letters*, 105(7):076802, 2010.

[91] Can-Li Song, Yi-Lin Wang, Ye-Ping Jiang, Yi Zhang, Cui-Zu Chang, Lili Wang, Ke He, Xi Chen, Jin-Feng Jia, Yayu Wang, et al. Topological insulator bi2se3 thin films grown on double-layer graphene by molecular beam epitaxy. *Applied Physics Letters*, 97(14), 2010.

[92] Yilin Wang, Yeping Jiang, Mu Chen, Zhi Li, Canli Song, Lili Wang, Ke He, Xi Chen, Xucun Ma, and Qi-Kun Xue. Scanning tunneling microscopy of

interface properties of bi2se3 on fese. *Journal of Physics: Condensed Matter*, 24(47):475604, 2012.

[93] Jeong Heum Jeon, Won Jun Jang, Jong Keon Yoon, and Se-Jong Kahng. Metal-supported high crystalline bi2se3 quintuple layers. *Nanotechnology*, 22(46):465602, 2011.

[94] Shuigang Xu, Yu Han, Xiaolong Chen, Zefei Wu, Lin Wang, Tianyi Han, Weiguang Ye, Huanhuan Lu, Gen Long, Yingying Wu, et al. van der waals epitaxial growth of atomically thin bi2se3 and thickness-dependent topological phase transition. *Nano letters*, 15(4):2645–2651, 2015.

[95] ZY Wang, X Guo, HD Li, TL Wong, N Wang, and MH Xie. Superlattices of bi2se3/in2se3: Growth characteristics and structural properties. *Applied physics letters*, 99(2), 2011.

[96] Jennifer Cano, Shiang Fang, JH Pixley, and Justin H Wilson. Moiré superlattice on the surface of a topological insulator. *Physical Review B*, 103(15):155157, 2021.

[97] Robert Karplus and JM Luttinger. Hall effect in ferromagnetics. *Physical Review*, 95(5):1154, 1954.

[98] T Jungwirth, Qian Niu, and AH MacDonald. Anomalous hall effect in ferromagnetic semiconductors. *Physical review letters*, 88(20):207208, 2002.

[99] Naoto Nagaosa, Jairo Sinova, Shigeki Onoda, Allan H MacDonald, and Nai Phuan Ong. Anomalous hall effect. *Reviews of modern physics*, 82(2):1539, 2010.

[100] Ming-Che Chang and Qian Niu. Berry phase, hyperorbits, and the hofstadter

spectrum: Semiclassical dynamics in magnetic bloch bands. *Physical Review B*, 53(11):7010, 1996.

[101] Ganesh Sundaram and Qian Niu. Wave-packet dynamics in slowly perturbed crystals: Gradient corrections and berry-phase effects. *Physical Review B*, 59(23):14915, 1999.

[102] Di Xiao, Ming-Che Chang, and Qian Niu. Berry phase effects on electronic properties. *Reviews of modern physics*, 82(3):1959, 2010.

[103] Peng Wei, Ferhat Katmis, Badih A Assaf, Hadar Steinberg, Pablo Jarillo-Herrero, Donald Heiman, and Jagadeesh S Moodera. Exchange-coupling-induced symmetry breaking in topological insulators. *Physical review letters*, 110(18):186807, 2013.

[104] Zilong Jiang, Cui-Zu Chang, Chi Tang, Jian-Guo Zheng, Jagadeesh S Moodera, and Jing Shi. Structural and proximity-induced ferromagnetic properties of topological insulator-magnetic insulator heterostructures. *AIP Advances*, 6(5), 2016.

[105] AV Matetskiy, IA Kibirev, T Hirahara, S Hasegawa, AV Zotov, and AA Saranin. Direct observation of a gap opening in topological interface states of mnse/bi2se3 heterostructure. *Applied Physics Letters*, 107(9), 2015.

[106] Toru Hirahara, Sergey V Eremeev, Tetsuroh Shirasawa, Yuma Okuyama, Takayuki Kubo, Ryosuke Nakanishi, Ryota Akiyama, Akari Takayama, Tetsuya Hajiri, Shin-ichiro Ideta, et al. Large-gap magnetic topological heterostructure formed by subsurface incorporation of a ferromagnetic layer. *Nano letters*, 17(6):3493–3500, 2017.

[107] Emile DL Rienks, Sebastian Wimmer, Jaime Sánchez-Barriga, Ondřej Caha, Partha Sarathi Mandal, Jiří Růžička, Andreas Ney, Hubert Steiner, Valen-

tine V Volobuev, Heiko Groiß, et al. Large magnetic gap at the dirac point in bi2te3/mnbi2te4 heterostructures. *Nature*, 576(7787):423–428, 2019.

[108] Murong Lang, Mohammad Montazeri, Mehmet C Onbasli, Xufeng Kou, Yabin Fan, Pramey Upadhyaya, Kaiyuan Yao, Frank Liu, Ying Jiang, Wanjun Jiang, et al. Proximity induced high-temperature magnetic order in topological insulator-ferrimagnetic insulator heterostructure. *Nano letters*, 14(6):3459–3465, 2014.

[109] Noah FQ Yuan and Liang Fu. Classification of critical points in energy bands based on topology, scaling, and symmetry. *Physical Review B*, 101(12):125120, 2020.

[110] Anirudh Chandrasekaran, Alex Shtyk, Joseph J Betouras, and Claudio Chamon. Catastrophe theory classification of fermi surface topological transitions in two dimensions. *Physical Review Research*, 2(1):013355, 2020.

[111] Zhaochen Liu, Huan Wang, and Jing Wang. Magnetic moiré surface states and flat chern bands in topological insulators. *Physical Review B*, 106(3):035114, 2022.

[112] Yi-Ming Wu, Ronny Thomale, and S Raghu. Sublattice interference promotes pair density wave order in kagome metals. *Physical Review B*, 108(8):L081117, 2023.

[113] Xiao-Liang Qi, Yong-Shi Wu, and Shou-Cheng Zhang. General theorem relating the bulk topological number to edge states in two-dimensional insulators. *Physical Review B*, 74(4):045125, 2006.

[114] Xiao-Liang Qi, Taylor L Hughes, and Shou-Cheng Zhang. Topological field theory of time-reversal invariant insulators. *Physical Review B*, 78(19):195424, 2008.

[115] Rafi Bistritzer and Allan H MacDonald. Moiré bands in twisted double-layer graphene. *Proceedings of the National Academy of Sciences*, 108(30):12233–12237, 2011.

[116] JMB Lopes dos Santos, NMR Peres, and AH Castro Neto. Graphene bilayer with a twist: electronic structure. *Physical review letters*, 99(25):256802, 2007.

[117] Eva Y Andrei, Dmitri K Efetov, Pablo Jarillo-Herrero, Allan H MacDonald, Kin Fai Mak, T Senthil, Emanuel Tutuc, Ali Yazdani, and Andrea F Young. The marvels of moiré materials. *Nature Reviews Materials*, 6(3):201–206, 2021.

[118] Kin Fai Mak and Jie Shan. Semiconductor moiré materials. *Nature Nanotechnology*, 17(7):686–695, 2022.

[119] Jian Wang and Luiz H. Santos. Classification of topological phase transitions and van Hove singularity steering mechanism in graphene superlattices. *Phys. Rev. Lett.*, 125:236805, Dec 2020.

[120] Jonah Herzog-Arbeitman, Zhi-Da Song, Nicolas Regnault, and B. Andrei Bernevig. Hofstadter topology: Noncrystalline topological materials at high flux. *Phys. Rev. Lett.*, 125:236804, Dec 2020.

[121] Eric M. Spanton, Alexander A. Zibrov, Haoxin Zhou, Takashi Taniguchi, Kenji Watanabe, Michael P. Zaletel, and Andrea F. Young. Observation of fractional Chern insulators in a van der Waals heterostructure. *Science*, 360(6384):62–66, 2018.

[122] Aaron L. Sharpe, Eli J. Fox, Arthur W. Barnard, Joe Finney, Kenji Watanabe, Takashi Taniguchi, M. A. Kastner, and David Goldhaber-Gordon. Emergent ferromagnetism near three-quarters filling in twisted bilayer graphene. *Science*, 365(6453):605–608, August 2019. Publisher: American Association for the Advancement of Science.

[123] M. Serlin, C. L. Tschirhart, H. Polshyn, Y. Zhang, J. Zhu, K. Watanabe, T. Taniguchi, L. Balents, and A. F. Young. Intrinsic quantized anomalous Hall effect in a moiré heterostructure. *Science*, 367(6480):900–903, February 2020. Publisher: American Association for the Advancement of Science.

[124] Yu Saito, Jingyuan Ge, Louk Rademaker, Kenji Watanabe, Takashi Taniguchi, Dmitry A. Abanin, and Andrea F. Young. Hofstadter subband ferromagnetism and symmetry-broken Chern insulators in twisted bilayer graphene. *Nature Physics*, 17(4):478–481, Apr 2021.

[125] Yonglong Xie, Andrew T. Pierce, Jeong Min Park, Daniel E. Parker, Eslam Khalaf, Patrick Ledwith, Yuan Cao, Seung Hwan Lee, Shaowen Chen, Patrick R. Forrester, Kenji Watanabe, Takashi Taniguchi, Ashvin Vishwanath, Pablo Jarillo-Herrero, and Amir Yacoby. Fractional Chern insulators in magic-angle twisted bilayer graphene. *Nature*, 600(7889):439–443, Dec 2021.

[126] Kevin P. Nuckolls, Myungchul Oh, Dillon Wong, Biao Lian, Kenji Watanabe, Takashi Taniguchi, B. Andrei Bernevig, and Ali Yazdani. Strongly correlated Chern insulators in magic-angle twisted bilayer graphene. *Nature*, 588(7839):610–615, December 2020. Number: 7839 Publisher: Nature Publishing Group.

[127] Ipsita Das, Xiaobo Lu, Jonah Herzog-Arbeitman, Zhi-Da Song, Kenji Watanabe, Takashi Taniguchi, B. Andrei Bernevig, and Dmitri K. Efetov. Symmetry-broken Chern insulators and Rashba-like Landau-level crossings in magic-angle bilayer graphene. *Nature Physics*, 17(6):710–714, June 2021. Number: 6 Publisher: Nature Publishing Group.

[128] Youngjoon Choi, Hyunjin Kim, Yang Peng, Alex Thomson, Cyprian Lewandowski, Robert Polski, Yiran Zhang, Harpreet Singh Arora, Kenji

Watanabe, Takashi Taniguchi, Jason Alicea, and Stevan Nadj-Perge. Correlation-driven topological phases in magic-angle twisted bilayer graphene. *Nature*, 589(7843):536–541, Jan 2021.

[129] Jeong Min Park, Yuan Cao, Kenji Watanabe, Takashi Taniguchi, and Pablo Jarillo-Herrero. Flavour Hund's coupling, Chern gaps and charge diffusivity in moiré graphene. *Nature*, 592(7852):43–48, April 2021. Number: 7852 Publisher: Nature Publishing Group.

[130] Petr Stepanov, Ming Xie, Takashi Taniguchi, Kenji Watanabe, Xiaobo Lu, Allan H. MacDonald, B. Andrei Bernevig, and Dmitri K. Efetov. Competing zero-field Chern insulators in superconducting twisted bilayer graphene. *Phys. Rev. Lett.*, 127:197701, Nov 2021.

[131] Andrew T. Pierce, Yonglong Xie, Jeong Min Park, Eslam Khalaf, Seung Hwan Lee, Yuan Cao, Daniel E. Parker, Patrick R. Forrester, Shaowen Chen, Kenji Watanabe, Takashi Taniguchi, Ashvin Vishwanath, Pablo Jarillo-Herrero, and Amir Yacoby. Unconventional sequence of correlated Chern insulators in magic-angle twisted bilayer graphene. *Nature Physics*, 17(11):1210–1215, November 2021. Number: 11 Publisher: Nature Publishing Group.

[132] Jiachen Yu, Benjamin A. Foutty, Zhaoyu Han, Mark E. Barber, Yoni Schattner, Kenji Watanabe, Takashi Taniguchi, Philip Phillips, Zhi-Xun Shen, Steven A. Kivelson, and Benjamin E. Feldman. Correlated Hofstadter spectrum and flavour phase diagram in magic-angle twisted bilayer graphene. *Nature Physics*, 18(7):825–831, 2022.

[133] Jiaqi Cai, Eric Anderson, Chong Wang, Xiaowei Zhang, Xiaoyu Liu, William Holtzmann, Yinong Zhang, Fengren Fan, Takashi Taniguchi, Kenji Watanabe,

et al. Signatures of fractional quantum anomalous hall states in twisted mote2. *Nature*, 622(7981):63–68, 2023.

[134] Heonjoon Park, Jiaqi Cai, Eric Anderson, Yinong Zhang, Jiayi Zhu, Xiaoyu Liu, Chong Wang, William Holtzmann, Chaowei Hu, Zhaoyu Liu, et al. Observation of fractionally quantized anomalous hall effect. *Nature*, 622(7981):74–79, 2023.

[135] Yihang Zeng, Zhengchao Xia, Kaifei Kang, Jiacheng Zhu, Patrick Knüppel, Chirag Vaswani, Kenji Watanabe, Takashi Taniguchi, Kin Fai Mak, and Jie Shan. Thermodynamic evidence of fractional chern insulator in moiré mote2. *Nature*, 622(7981):69–73, 2023.

[136] Fan Xu, Zheng Sun, Tongtong Jia, Chang Liu, Cheng Xu, Chushan Li, Yu Gu, Kenji Watanabe, Takashi Taniguchi, Bingbing Tong, et al. Observation of integer and fractional quantum anomalous hall effects in twisted bilayer mote 2. *Physical Review X*, 13(3):031037, 2023.

[137] Zhengguang Lu, Tonghang Han, Yuxuan Yao, Aidan P Reddy, Jixiang Yang, Junseok Seo, Kenji Watanabe, Takashi Taniguchi, Liang Fu, and Long Ju. Fractional quantum anomalous hall effect in multilayer graphene. *Nature*, 626(8000):759–764, 2024.

[138] AA Abrikosov, JC Campuzano, and K Gofron. Experimentally observed extended saddle point singularity in the energy spectrum of $YBa_2Cu_3O_{6.9}$ and $YBa_2Cu_4O_8$ and some of the consequences. *Physica C: Superconductivity*, 214(1-2):73–79, 1993.

[139] K Gofron, JC Campuzano, AA Abrikosov, M Lindroos, A Bansil, H Ding, D Koelling, and B Dabrowski. Observation of an "extended" Van Hove

singularity in $YBa_2Cu_4O_8$ by ultrahigh energy resolution angle-resolved photoemission. *Physical review letters*, 73(24):3302, 1994.

[140] Lakshmi Pullasseri and Luiz H Santos. Chern bands with higher-order Van Hove singularities on topological moiré surface states. *Physical Review B*, 110(11):115125, 2024.

[141] Jun Wen, Andreas Rüegg, C-C Joseph Wang, and Gregory A Fiete. Interaction-driven topological insulators on the kagome and the decorated honeycomb lattices. *Physical Review B—Condensed Matter and Materials Physics*, 82(7):075125, 2010.

[142] Wan-Sheng Wang, Zheng-Zhao Li, Yuan-Yuan Xiang, and Qiang-Hua Wang. Competing electronic orders on kagome lattices at Van Hove filling. *Physical Review B—Condensed Matter and Materials Physics*, 87(11):115135, 2013.

[143] Maximilian L Kiesel, Christian Platt, and Ronny Thomale. Unconventional Fermi surface instabilities in the kagome Hubbard model. *Physical review letters*, 110(12):126405, 2013.

[144] Yu-Ping Lin and Rahul M Nandkishore. Complex charge density waves at Van Hove singularity on hexagonal lattices: Haldane-model phase diagram and potential realization in the kagome metals AV_3Sb_5 (A= K, Rb, Cs). *Physical Review B*, 104(4):045122, 2021.

[145] Titus Neupert, Luiz Santos, Claudio Chamon, and Christopher Mudry. Fractional quantum Hall states at zero magnetic field. *Phys. Rev. Lett.*, 106:236804, Jun 2011.

[146] D. N. Sheng, Zheng-Cheng Gu, Kai Sun, and L. Sheng. Fractional quantum hall effect in the absence of landau levels. *Nature Communications*, 2:389 EP –, 07 2011.

[147] Evelyn Tang, Jia-Wei Mei, and Xiao-Gang Wen. High-temperature fractional quantum hall states. *Phys. Rev. Lett.*, 106:236802, Jun 2011.

[148] Kai Sun, Zhengcheng Gu, Hosho Katsura, and S. Das Sarma. Nearly flatbands with nontrivial topology. *Phys. Rev. Lett.*, 106:236803, Jun 2011.

[149] N. Regnault and B. Andrei Bernevig. Fractional chern insulator. *Phys. Rev. X*, 1:021014, Dec 2011.

[150] Tilman Schwemmer, Hendrik Hohmann, Matteo Dürrnagel, Janik Potten, Jacob Beyer, Stephan Rachel, Yi-Ming Wu, Srinivas Raghu, Tobias Müller, Werner Hanke, and Ronny Thomale. Pair density wave instability in the kagome Hubbard model, 2023.

[151] Gyu-Boong Jo, Jennie Guzman, Claire K. Thomas, Pavan Hosur, Ashvin Vishwanath, and Dan M. Stamper-Kurn. Ultracold atoms in a tunable optical kagome lattice. *Phys. Rev. Lett.*, 108:045305, Jan 2012.

[152] Gregor Jotzu, Michael Messer, Rémi Desbuquois, Martin Lebrat, Thomas Uehlinger, Daniel Greif, and Tilman Esslinger. Experimental realization of the topological haldane model with ultracold fermions. *Nature*, 515(7526):237–240, 2014.

[153] Taige Wang, Noah F. Q. Yuan, and Liang Fu. Moiré surface states and enhanced superconductivity in topological insulators. *Phys. Rev. X*, 11:021024, Apr 2021.

[154] Noah F. Q. Yuan and Liang Fu. Classification of critical points in energy bands based on topology, scaling, and symmetry. *Phys. Rev. B*, 101:125120, Mar 2020.

[155] Takahiro Fukui, Yasuhiro Hatsugai, and Hiroshi Suzuki. Chern numbers

in discretized Brillouin zone: efficient method of computing (spin) Hall conductances. *Journal of the Physical Society of Japan*, 74(6):1674–1677, 2005.

[156] Alexei Kitaev. Periodic table for topological insulators and superconductors. In *AIP conference proceedings*, volume 1134, pages 22–30. American Institute of Physics, 2009.

[157] Andreas P Schnyder, Shinsei Ryu, Akira Furusaki, and Andreas WW Ludwig. Classification of topological insulators and superconductors. In *AIP Conference Proceedings*, volume 1134, pages 10–21. American Institute of Physics, 2009.

[158] Shinsei Ryu, Andreas P Schnyder, Akira Furusaki, and Andreas WW Ludwig. Topological insulators and superconductors: tenfold way and dimensional hierarchy. *New Journal of Physics*, 12(6):065010, 2010.

[159] Steven M Girvin and Kun Yang. *Modern condensed matter physics*. Cambridge University Press, 2019.

[160] Shlomo Alexander and Raymond Orbach. Density of states on fractals:fractons. *Journal de Physique Lettres*, 43(17):625–631, 1982.

[161] A Blumen, Joseph Klafter, BS White, and G Zumofen. Continuous-time random walks on fractals. *Physical review letters*, 53(14):1301, 1984.

[162] R Orbach. Dynamics of fractal networks. *Science*, 231(4740):814–819, 1986.

[163] Shlomo Havlin and Daniel Ben-Avraham. Diffusion in disordered media. *Advances in physics*, 36(6):695–798, 1987.

[164] XY Xu, XW Wang, DY Chen, CM Smith, and XM Jin. Quantum transport in fractal networks. nature photonics 15, 703–710, 2021.

[165] Edo van Veen, Shengjun Yuan, Mikhail I Katsnelson, Marco Polini, and Andrea Tomadin. Quantum transport in sierpinski carpets. *Physical Review B*, 93(11):115428, 2016.

[166] Georges Bouzerar and Didier Mayou. Quantum transport in self-similar graphene carpets. *Physical Review Research*, 2(3):033063, 2020.

[167] Claudio Chamon. Quantum glassiness in strongly correlated clean systems: An example of topological overprotection. *Physical review letters*, 94(4):040402, 2005.

[168] Rahul M Nandkishore and Michael Hermele. Fractons. *Annual Review of Condensed Matter Physics*, 10:295–313, 2019.

[169] Zhi-Gang Song, Yan-Yang Zhang, and Shu-Shen Li. The topological insulator in a fractal space. *Applied Physics Letters*, 104(23):233106, 2014.

[170] Marta Brzezińska, Ashley M Cook, and Titus Neupert. Topology in the sierpiński-hofstadter problem. *Physical Review B*, 98(20):205116, 2018.

[171] Edo van Veen, Andrea Tomadin, Marco Polini, Mikhail I Katsnelson, and Shengjun Yuan. Optical conductivity of a quantum electron gas in a sierpinski carpet. *Physical Review B*, 96(23):235438, 2017.

[172] Askar A Iliasov, Mikhail I Katsnelson, and Shengjun Yuan. Hall conductivity of a sierpiński carpet. *Physical Review B*, 101(4):045413, 2020.

[173] Tom Westerhout, Edo van Veen, Mikhail I Katsnelson, and Shengjun Yuan. Plasmon confinement in fractal quantum systems. *Physical Review B*, 97(20):205434, 2018.

[174] Zhaoju Yang, Eran Lustig, Yaakov Lumer, and Mordechai Segev. Photonic

floquet topological insulators in a fractal lattice. *Light: Science & Applications*, 9(1):128, 2020.

[175] Shriya Pai and Abhinav Prem. Topological states on fractal lattices. *Physical Review B*, 100(15):155135, 2019.

[176] Tobias Biesenthal, Lukas J Maczewsky, Zhaoju Yang, Mark Kremer, Mordechai Segev, Alexander Szameit, and Matthias Heinrich. Fractal photonic topological insulators. *Science*, 376(6597):1114–1119, 2022.

[177] Kenjiro K Gomes, Warren Mar, Wonhee Ko, Francisco Guinea, and Hari C Manoharan. Designer dirac fermions and topological phases in molecular graphene. *Nature*, 483(7389):306–310, 2012.

[178] Carlos Forsythe, Xiaodong Zhou, Kenji Watanabe, Takashi Taniguchi, Abhay Pasupathy, Pilkyung Moon, Mikito Koshino, Philip Kim, and Cory R Dean. Band structure engineering of 2d materials using patterned dielectric superlattices. *Nature nanotechnology*, 13(7):566–571, 2018.

[179] Sudipta Dubey, Vibhor Singh, Ajay K Bhat, Pritesh Parikh, Sameer Grover, Rajdeep Sensarma, Vikram Tripathi, K Sengupta, and Mandar M Deshmukh. Tunable superlattice in graphene to control the number of dirac points. *Nano letters*, 13(9):3990–3995, 2013.

[180] Martin Drienovsky, Franz-Xaver Schrettenbrunner, Andreas Sandner, Dieter Weiss, Jonathan Eroms, Ming-Hao Liu, Fedor Tkatschenko, Klaus Richter, et al. Towards superlattices: Lateral bipolar multibarriers in graphene. *Physical Review B*, 89(11):115421, 2014.

[181] Ziqin Yue, Jianwei Huang, Ruohan Wang, Jia-Wan Li, Hongtao Rong, Yucheng Guo, Han Wu, Yichen Zhang, Junichiro Kono, Xingjiang Zhou, et al. Topo-

logical surface state evolution in bi2se3 via surface etching. *Nano Letters*, 2024.

[182] Holger Bech Nielsen and Masao Ninomiya. Absence of neutrinos on a lattice:(i). proof by homotopy theory. *Nuclear Physics B*, 185(1):20–40, 1981.

[183] Claudio de C Chamon, Christopher Mudry, and Xiao-Gang Wen. Localization in two dimensions, gaussian field theories, and multifractality. *Physical review letters*, 77(20):4194, 1996.

[184] Horacio E Castillo, Claudio de C Chamon, Eduardo Fradkin, Paul M Goldbart, and Christopher Mudry. Exact calculation of multifractal exponents of the critical wave function of dirac fermions in a random magnetic field. *Physical Review B*, 56(16):10668, 1997.

[185] Ferdinand Evers and Alexander D Mirlin. Anderson transitions. *Reviews of Modern Physics*, 80(4):1355, 2008.

[186] Matthew S Foster. Multifractal nature of the surface local density of states in three-dimensional topological insulators with magnetic and nonmagnetic disorder. *Physical Review B*, 85(8):085122, 2012.

[187] Matthew S Foster, Hong-Yi Xie, and Yang-Zhi Chou. Topological protection, disorder, and interactions: Survival at the surface of three-dimensional topological superconductors. *Physical Review B*, 89(15):155140, 2014.

[188] Paraj Titum, Netanel H Lindner, Mikael C Rechtsman, and Gil Refael. Disorder-induced floquet topological insulators. *Physical review letters*, 114(5):056801, 2015.

[189] Annica M Black-Schaffer and Alexander V Balatsky. Strong potential impuri-

ties on the surface of a topological insulator. *Physical Review B*, 85(12):121103, 2012.

[190] Jhih-Sheng Wu, Michael M Fogler, et al. Scattering of two-dimensional massless dirac electrons by a circular potential barrier. *Physical Review B*, 90(23):235402, 2014.

[191] K Ziegler. Dirac fermions with disorder in two dimensions: Exact results. *Physical Review B*, 53(15):9653, 1996.

[192] Andrei A Fedorenko, David Carpentier, and Edmond Orignac. Two-dimensional dirac fermions in the presence of long-range correlated disorder. *Physical Review B*, 85(12):125437, 2012.

[193] L Andrew Wray. Topological transistor. *Nature Physics*, 8(10):705–706, 2012.

[194] Andreas WW Ludwig, Matthew PA Fisher, R Shankar, and G Grinstein. Integer quantum hall transition: An alternative approach and exact results. *Physical Review B*, 50(11):7526, 1994.

[195] Tetsuya Sakurai and Hiroshi Sugiura. A projection method for generalized eigenvalue problems using numerical integration. *Journal of computational and applied mathematics*, 159(1):119–128, 2003.

[196] Franz Wegner. Inverse participation ratio in 2+ ε dimensions. *Zeitschrift für Physik B Condensed Matter*, 36(3):209–214, 1980.

[197] Bodo Huckestein. Scaling theory of the integer quantum hall effect. *Reviews of Modern Physics*, 67(2):357, 1995.

[198] Ferdinand Evers and AD Mirlin. Fluctuations of the inverse participation ratio at the anderson transition. *Physical review letters*, 84(16):3690, 2000.

[199] Benoit B Mandelbrot. Intermittent turbulence in self-similar cascades: divergence of high moments and dimension of the carrier. *Journal of fluid Mechanics*, 62(2):331–358, 1974.

[200] H George E Hentschel and Itamar Procaccia. The infinite number of generalized dimensions of fractals and strange attractors. *Physica D: Nonlinear Phenomena*, 8(3):435–444, 1983.

[201] Yan V Fyodorov and Alexander D Mirlin. Mesoscopic fluctuations of eigenfunctions and level-velocity distribution in disordered metals. *Physical Review B*, 51(19):13403, 1995.

[202] AD Mirlin and Ferdinand Evers. Multifractality and critical fluctuations at the anderson transition. *Physical Review B*, 62(12):7920, 2000.

[203] VN Prigodin and BL Altshuler. Long-range spatial correlations of eigenfunctions in quantum disordered systems. *Physical review letters*, 80(9):1944, 1998.

[204] Benoit B Mandelbrot. Self-affine fractals and fractal dimension. *Physica scripta*, 32(4):257, 1985.

[205] Martin Bouda, Joshua S Caplan, and James E Saiers. Box-counting dimension revisited: presenting an efficient method of minimizing quantization error and an assessment of the self-similarity of structural root systems. *Frontiers in plant science*, 7:149, 2016.

[206] Kayhan Foroutan-pour, Pierre Dutilleul, and Donald L Smith. Advances in the implementation of the box-counting method of fractal dimension estimation. *Applied mathematics and computation*, 105(2-3):195–210, 1999.

[207] Douglas R Hofstadter. Energy levels and wave functions of bloch electrons in rational and irrational magnetic fields. *Physical review B*, 14(6):2239, 1976.

[208] Robert-Jan Slager, Vladimir Juričić, and Bitan Roy. Dissolution of topological fermi arcs in a dirty weyl semimetal. *Physical Review B*, 96(20):201401, 2017.

[209] Justin H Wilson, JH Pixley, David A Huse, Gil Refael, and S Das Sarma. Do the surface fermi arcs in weyl semimetals survive disorder? *Physical Review B*, 97(23):235108, 2018.

[210] Xiaokun Teng, Ji Seop Oh, Hengxin Tan, Lebing Chen, Jianwei Huang, Bin Gao, Jia-Xin Yin, Jiun-Haw Chu, Makoto Hashimoto, Donghui Lu, et al. Magnetism and charge density wave order in kagome FeGe. *Nature physics*, 19(6):814–822, 2023.

[211] Xiaokun Teng, Lebing Chen, Feng Ye, Elliott Rosenberg, Zhaoyu Liu, Jia-Xin Yin, Yu-Xiao Jiang, Ji Seop Oh, M Zahid Hasan, Kelly J Neubauer, et al. Discovery of charge density wave in a kagome lattice antiferromagnet. *Nature*, 609(7927):490–495, 2022.

[212] Jia-Xin Yin, Yu-Xiao Jiang, Xiaokun Teng, Md Shafayat Hossain, Sougata Mardanya, Tay-Rong Chang, Zijin Ye, Gang Xu, M Michael Denner, Titus Neupert, et al. Discovery of charge order and corresponding edge state in kagome magnet fege. *Physical review letters*, 129(16):166401, 2022.

[213] Mikael Fremling, Michal van Hooft, Cristiane Morais Smith, and Lars Fritz. Existence of robust edge currents in sierpiński fractals. *Physical Review Research*, 2(1):013044, 2020.

[214] Eytan Domany, Shlomo Alexander, David Bensimon, and Leo P Kadanoff. Solutions to the schrödinger equation on some fractal lattices. *Physical Review B*, 28(6):3110, 1983.

[215] Stefan Boettcher, Stefan Falkner, and Renato Portugal. Renormalization and scaling in quantum walks. *Physical Review A*, 90(3):032324, 2014.

[216] Shanshan Li and Stefan Boettcher. Renormalization group for a continuous-time quantum search in finite dimensions. *Physical Review A*, 95(3):032301, 2017.

[217] Stefan Boettcher and Shanshan Li. Analysis of coined quantum walks with renormalization. *Physical Review A*, 97(1):012309, 2018.

[218] Tsutomu Ikegami, Tetsuya Sakurai, and Umpei Nagashima. A filter diagonalization for generalized eigenvalue problems based on the sakurai–sugiura projection method. *Journal of Computational and Applied Mathematics*, 233(8):1927–1936, 2010.

[219] Ignace Bogaert, Bart Michiels, and Jan Fostier. O(1) computation of legendre polynomials and gauss–legendre nodes and weights for parallel computing. *SIAM Journal on Scientific Computing*, 34(3):C83–C101, 2012.